Supplementary material

Synthesis, Characterisation and Biological Evaluation of Monometallic Re(I) and Heterobimetallic Re(I)/Fe(II) Complexes with a 1,2,3-Triazolyl Pyridine Chelating Moiety

Silvio Jakopec,[a,†] Lisa Gourdon,[b,†] Ivona Čipor,[c,†] Andrijana Meščić Macan,[a] Berislav Perić,[d] Ivo Piantanida,[c] Kevin Cariou,[b] Gilles Gasser,[b,*] Srećko I. Kirin[d,*] and Silvana Raić-Malić[a,*]

[a]University of Zagreb, Faculty of Chemical Engineering and Technology, Department of Organic Chemistry, Marulićev trg 20, HR-10000 Zagreb, Croatia.
[b]Chimie ParisTech, PSL University, Institute of Chemistry for Life and Health Sciences, Laboratory for Inorganic Chemical Biology, F-75005 Paris, France.
[c]Ruđer Bošković Institute, Division of Organic Chemistry and Biochemistry, Laboratory for Biomolecular Interactions and Spectroscopy, Bijenička cesta 54, 10 000 Zagreb, Croatia.
[d]Ruđer Bošković Institute, Division of Materials Chemistry, Laboratory for solid state and complex compounds chemistry, Bijenička cesta 54, 10 000 Zagreb, Croatia.

[†]These authors have contributed equally to the work.
Corresponding authors: sraic@fkit.hr, srecko.kirin@irb.hr, gilles.gasser@chimieparistech.psl.eu

Contents

1. Structures of the prepared ligands and complexes

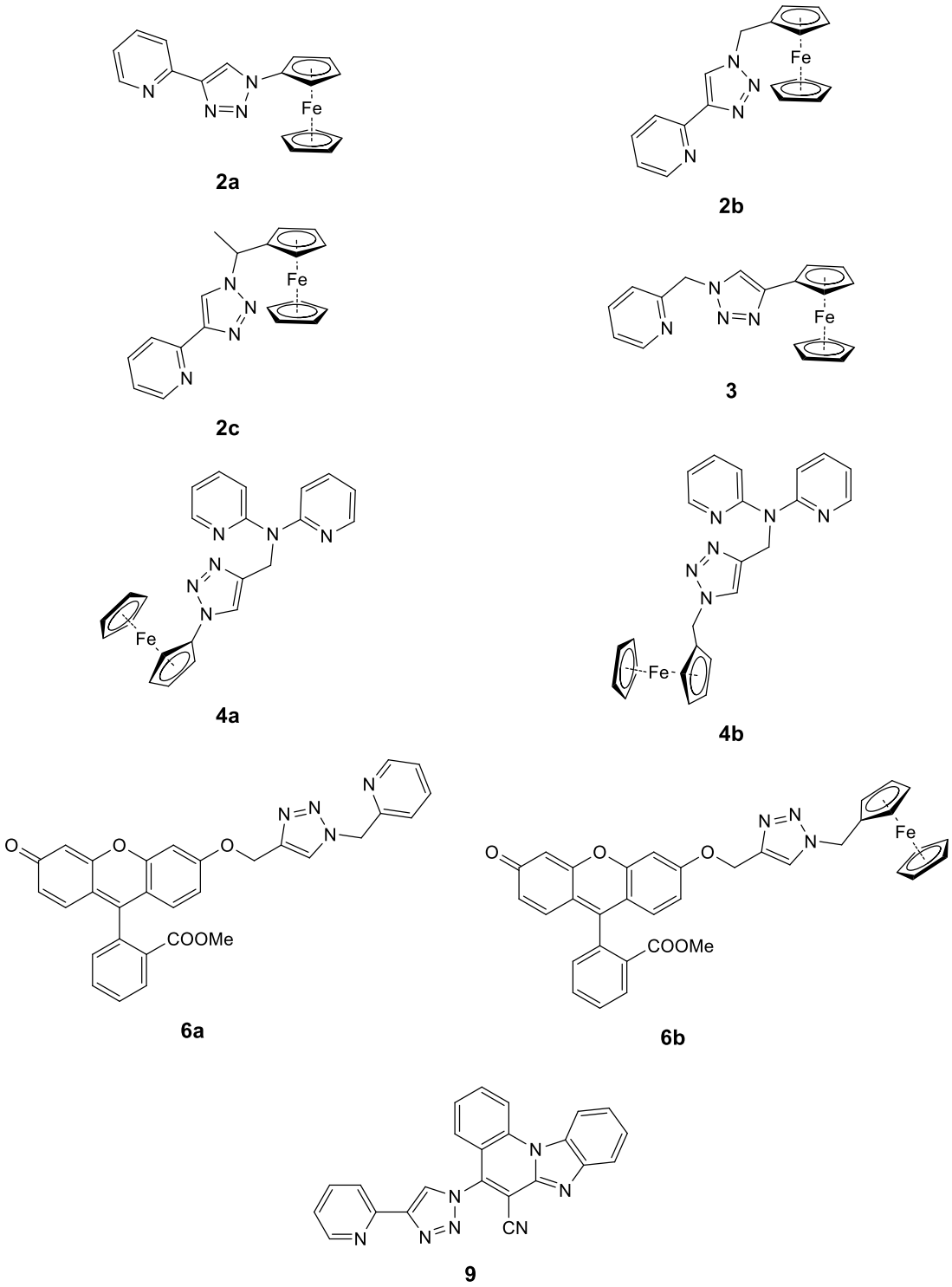

Figure S1. Structures of the prepared ligands

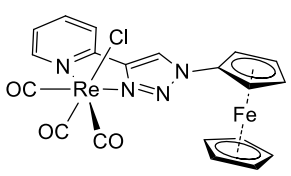

2a$_{Re}$

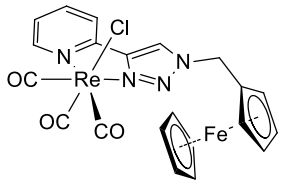

2b$_{Re}$

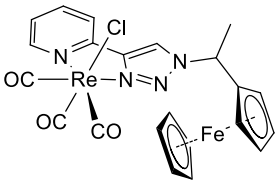

2c$_{Re}$

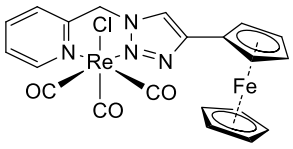

3$_{Re}$

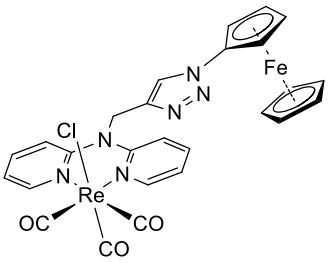

4a$_{Re}$

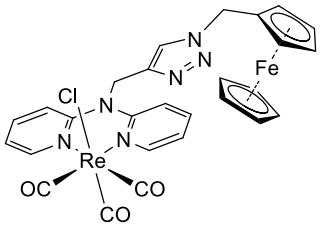

4b$_{Re}$

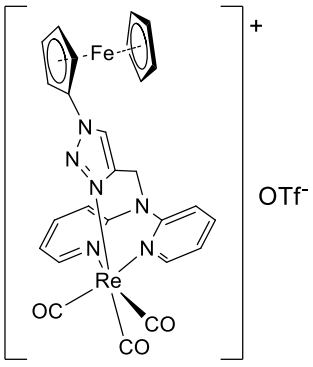

4a$_{Re}$•OTf

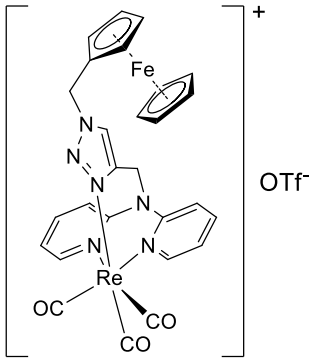

4b$_{Re}$•OTf

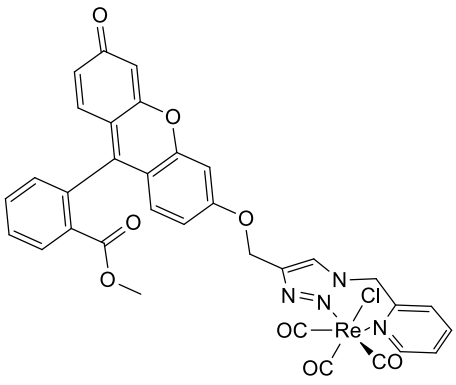

6a$_{Re}$

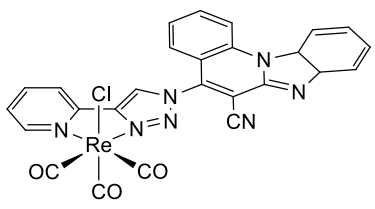

9$_{Re}$

Figure S2. Structures of the prepared metal complexes

2. X-ray crystallography

Table S1. Experimental data for the X-ray diffraction studies

Compound	**2b**	**3**	**$2a_{Re}$**
Formula	$C_{18}H_{16}FeN_4$	$C_{18}H_{16}FeN_4$	$C_{20}H_{14}ClFeN_4O_3Re$
F_w (g mol^{-1})	344.20	344.20	635.85
Crystal system	Monoclinic	Monoclinic	Orthorhombic
Space group	$P2_1/n$	$P2_1/n$	$Pbca$
a (Å)	5.8434(1)	5.8002(1)	10.6081(2)
b (Å)	28.9507(4)	29.8989(3)	9.5189(2)
c (Å)	9.3534(1)	9.0804(1)	41.2655(7)
α (°)	90	90	90
β (°)	99.118(1)	102.836 (1)	90
γ (°)	90	90	90
V (Å^3)	1562.33(4)	1535.37(4)	4166.9(1)
Z	4	4	8
Z'	1	1	1
D_{calc} (g cm^{-3})	1.463	1.489	2.027
F(000)	712	712	2432
Radiation (Å), instrumnet	1.54184, Xcalibur	1.54184, Xcalibur	1.54184, Dualflex
Temperature (K)	293(2)	293(2)	295.6 (2)
Reflections collected	7572	7469	19564
Independent reflections	3231	3179	4435
R_{init}	0.0309	0.0283	0.0718
Reflections observed	2904	2901	3808
Parameters	208	210	271
R_1 [$I > 2\sigma(I)$][a]	0.0421	0.0362	0.0522
wR_2 (all data)[b]	0.1122	0.1075	0.1473
Goof, S[c]	1.038	1.054	1.062
Maximum/minimum electron density (e Å^3)	0.297/-0.541	0.344/-0.405	2.590/-0.901

[a] $R_1 = \Sigma||F_o| - |F_c||/\Sigma|F_o|$. [b] $wR_2 = \{\Sigma[w(F_o^2 - F_c^2)^2]/\Sigma[w(F_o^2)^2]\}^{1/2}$. [c] $S = \{\Sigma[w(F_o^2 - F_c^2)^2]/(n - p)\}^{1/2}$ where n is number of reflections and p is the total number of parameters refined

Table S1. Experimental data for the X-ray diffraction studies (continuation)

Compound	**3_{Re}**	**$4a_{Re}$**	**$4b_{Re}$·OTf**
Formula	$C_{21}H_{16}ClFeN_4O_3Re$	$C_{26}H_{20}ClFeN_6O_3Re$	$[C_{27}H_{22}FeN_6O_3Re][CF_3SO_3]\cdot CHCl_3$
F_w (g mol^{-1})	649.88	741.98	988.99
Crystal system	Triclinic	Triclinic	Monoclinic
Space group	$P\bar{1}$	$P\bar{1}$	$P2_1/c$
a (Å)	12.8718(7)	8.8950(6)	9.3014 (1)
b (Å)	13.0241(4)	11.5329(8)	31.0939(4)
c (Å)	13.7907(4)	14.289(1)	12.5522(2)
α (°)	80.131(3)	72.524(7)	90
β (°)	75.297(4)	81.313(6)	102.377(1)
γ (°)	84.827(4)	71.001(6)	90
V (Å^3)	2200.48(16)	1319.7(2)	3545.93(8)
Z	4	2	4
Z'	2	1	1
D_{calc} (g cm^{-3})	1.962	1.867	1.853
F(000)	1248	720	1928
Radiation (Å), instrumnet	1.54184, Xcalibur	1.54184, Dualflex	1.54184, Dualflex
Temperature (*K*)	293(2)	296(1)	294.9(1)
Reflections collected	22603	12620	29446
Independent reflections	9056	5006	7289
R_{init}	0.0755	0.1160	0.0691
Reflections observed	7258	3966	6192
Parameters	577	343	470
R_1 [$I > 2\sigma(I)$][a]	0.0684	0.1169	0.0670
wR_2 (all data)[b]	0.2111	0.3418	0.1851
Goof, S[c]	1.037	1.043	1.069
Maximum/minimum electron density (e Å^3)	2.492/-2.475	3.152/-3.842	2.356/-1.587

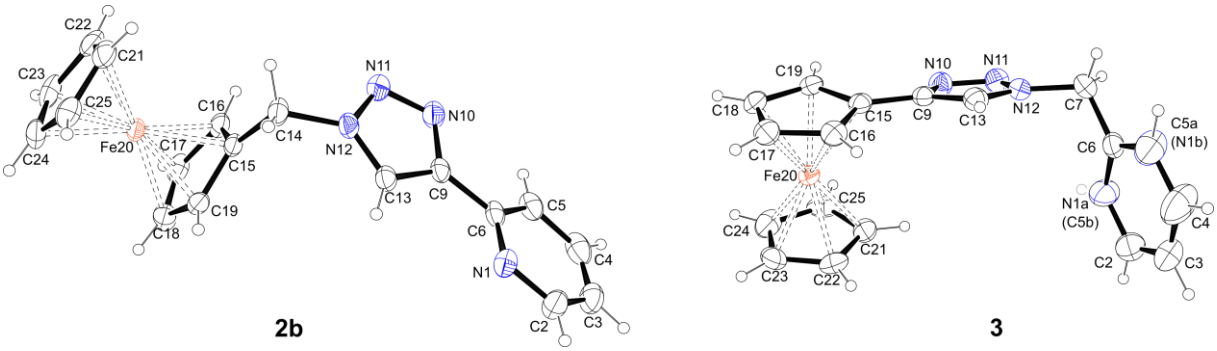

Figure S3. Molecular structure and atomic numbering scheme for ligands 2b and 3.

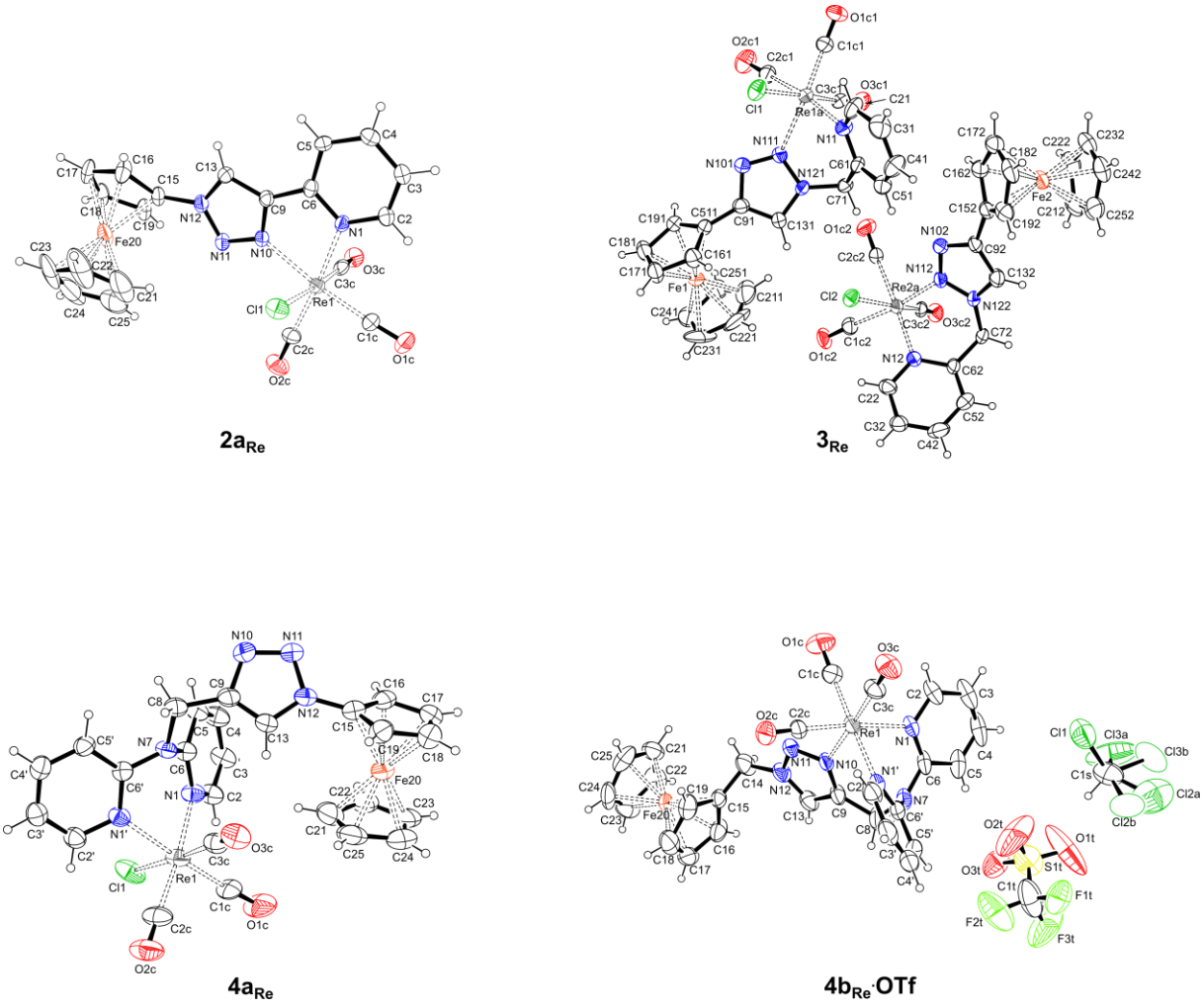

Figure S4. Molecular structure and atomic numbering scheme for complexes 2a$_{Re}$, 3$_{Re}$, 4a$_{Re}$, 4b$_{Re}$·OTf. For 3$_{Re}$ only positions of Re atoms with occupancy > 90% are shown. For 4b$_{Re}$·OTf positions of disordered Cl atoms with lower occupancy (from chloroform solvent molecule) are shown as open ellipsoids.

3. NMR spectra of Re(I) complexes

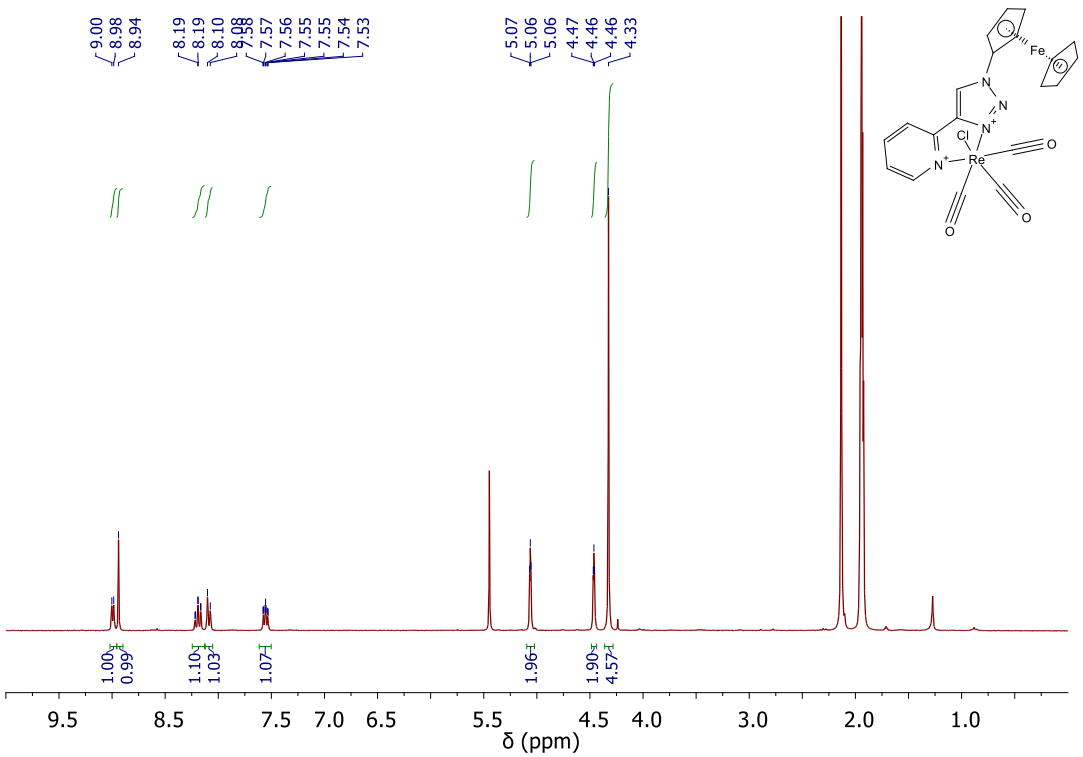

Figure S5. ^{1}H NMR spectrum of 2a$_{Re}$ (ACN-d_3)

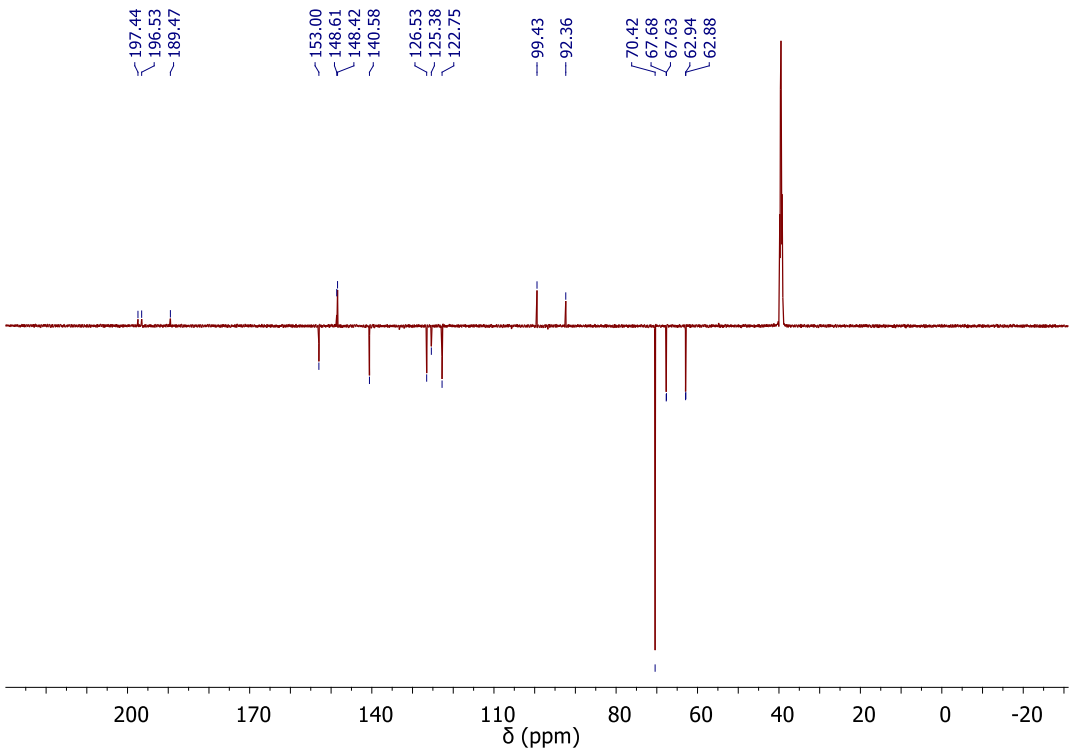

Figure S6. ^{13}C NMR spectrum of 2a$_{Re}$ (DMSO-d_6)

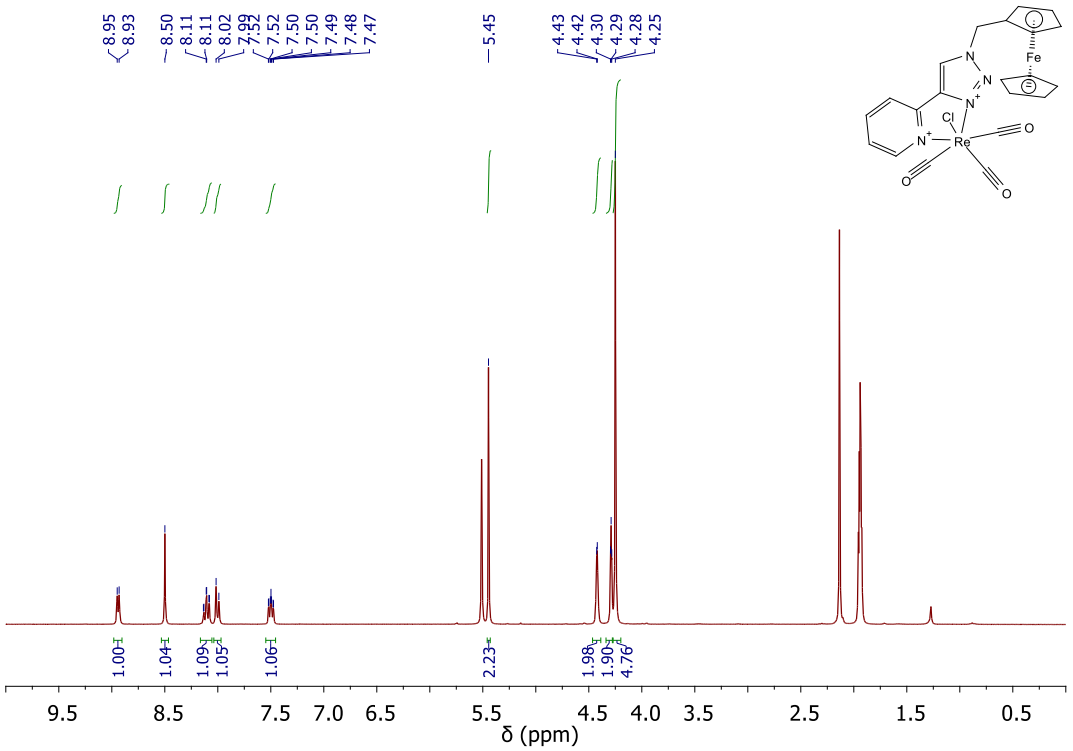

Figure S7. ^{1}H NMR spectrum of $2b_{Re}$ (ACN-d_3)

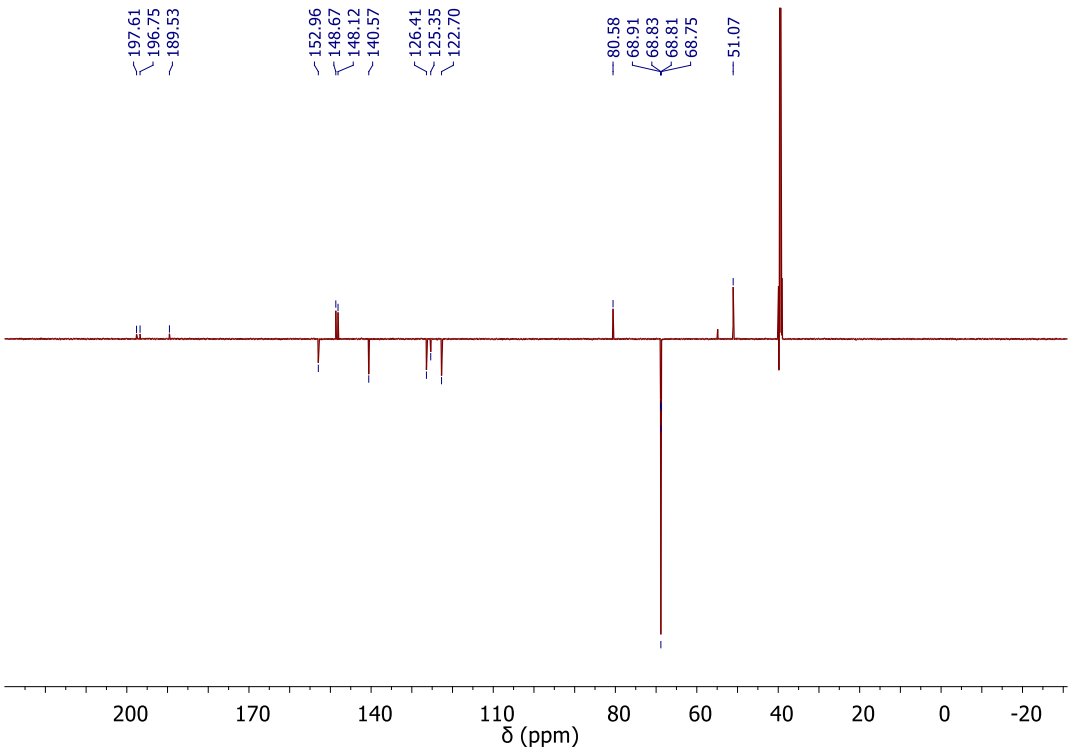

Figure S8. ^{13}C NMR spectrum of $2b_{Re}$ (DMSO-d_6)

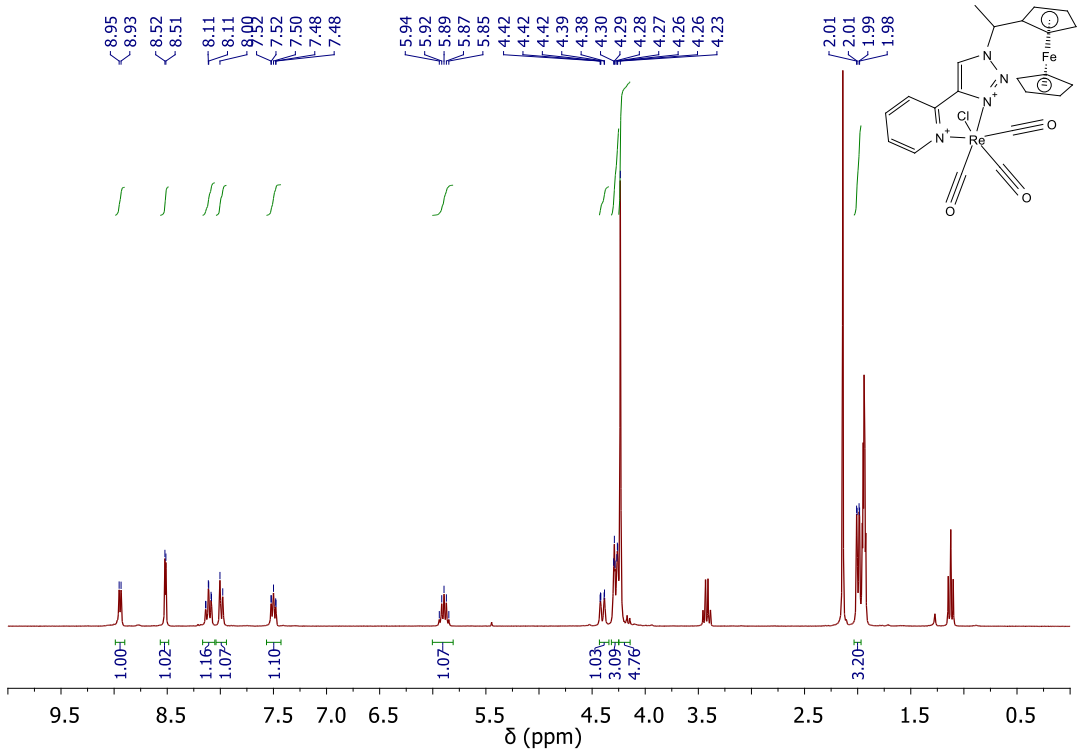

Figure S9. ^{1}H NMR spectrum of $2c_{Re}$ (ACN-d_3)

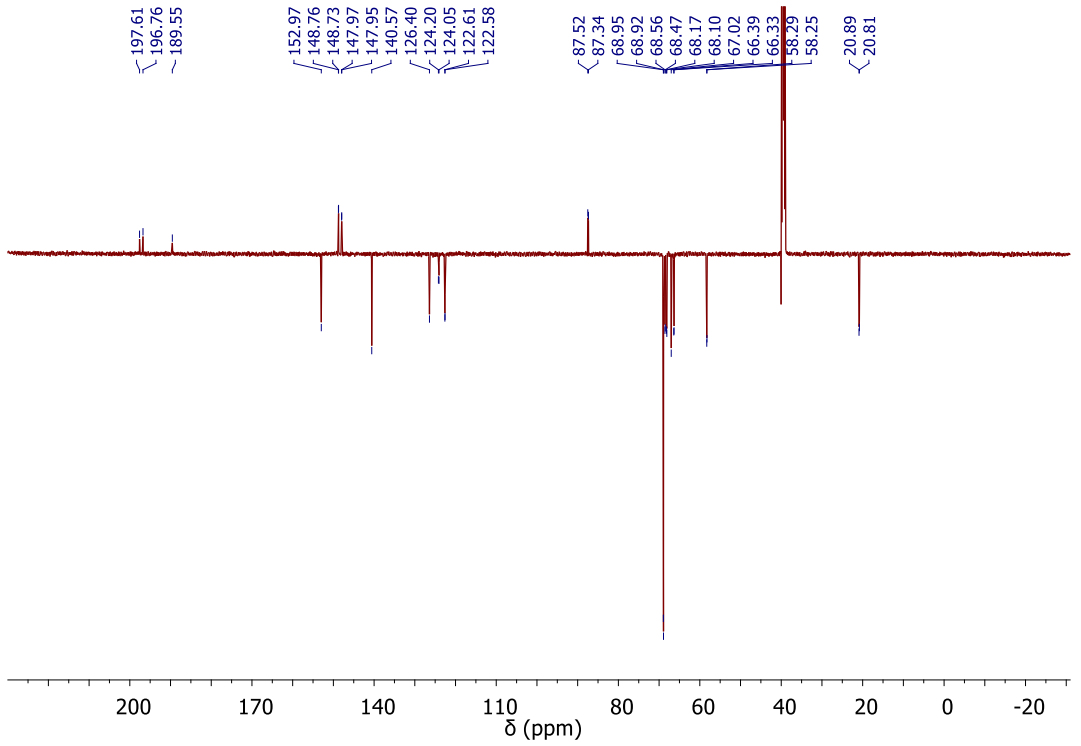

Figure S10. ^{13}C NMR spectrum of $2c_{Re}$ (DMSO-d_6)

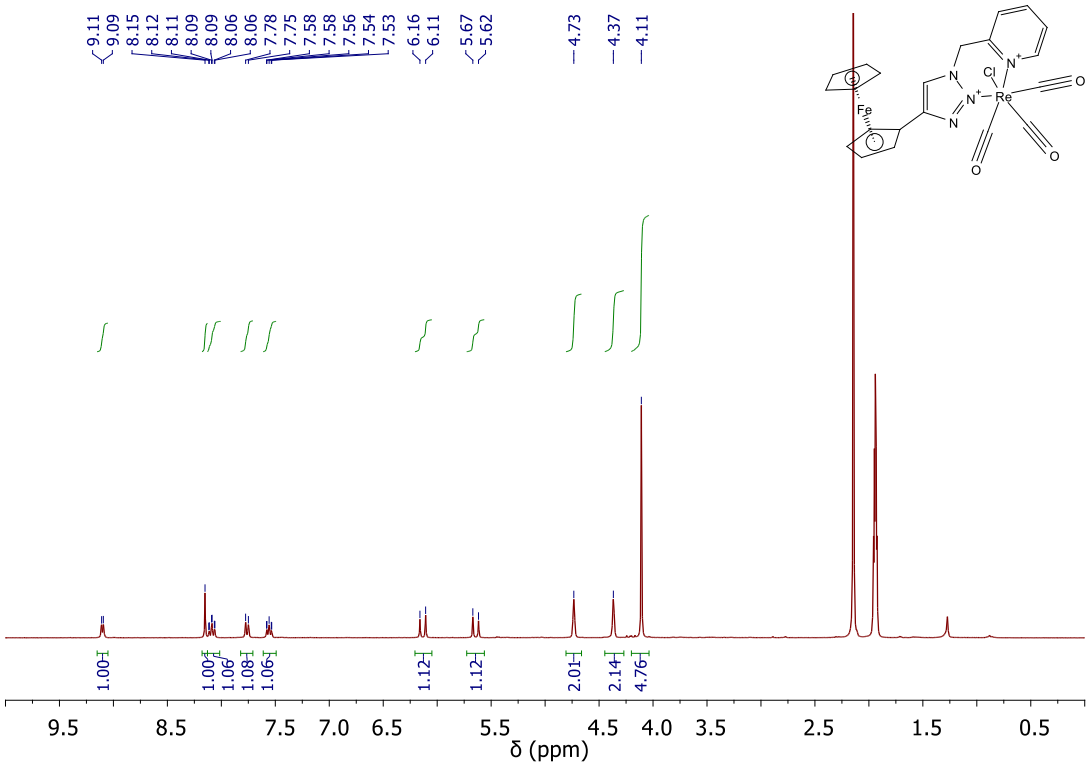

Figure S11. ^{1}H NMR spectrum of 3_{Re} (ACN-d_3)

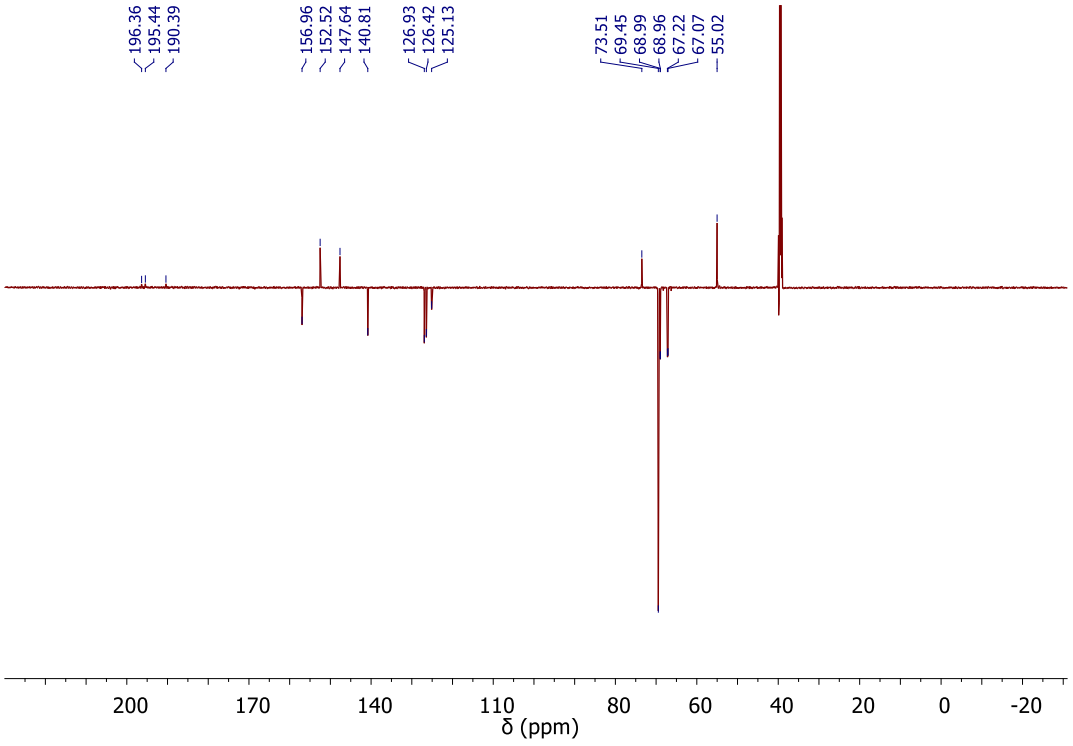

Figure S12. ^{13}C NMR spectrum of 3_{Re} (DMSO-d_6)

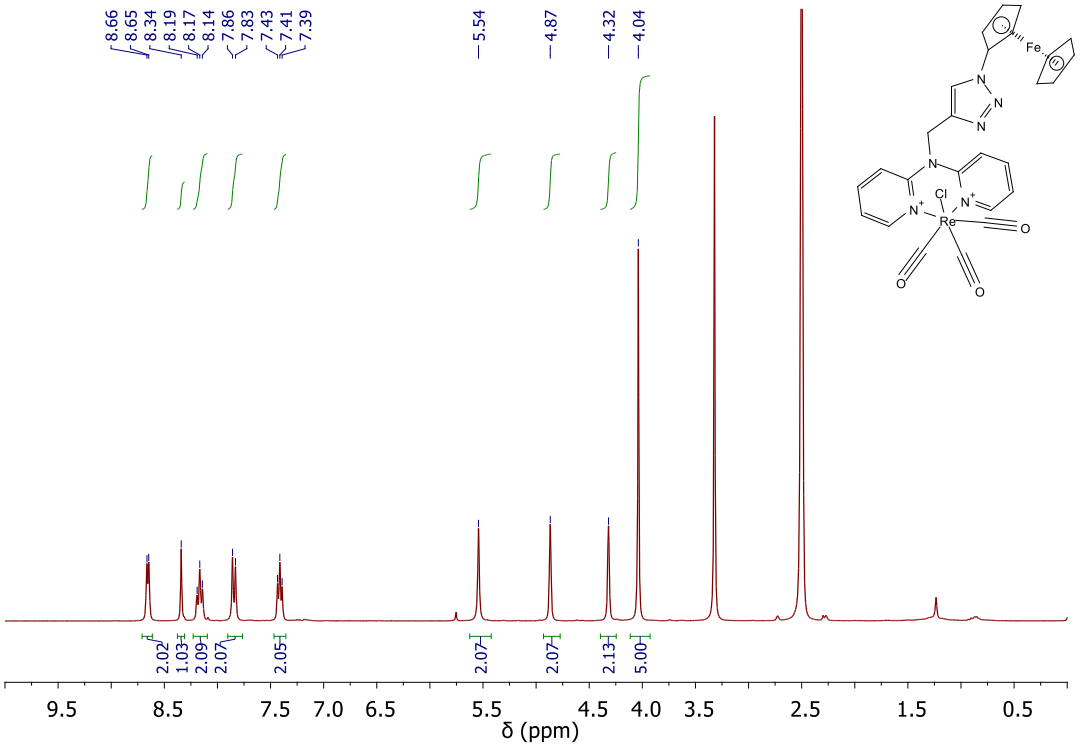

Figure S13. ^{1}H NMR spectrum of 4a$_{Re}$(DMSO-*d*$_6$)

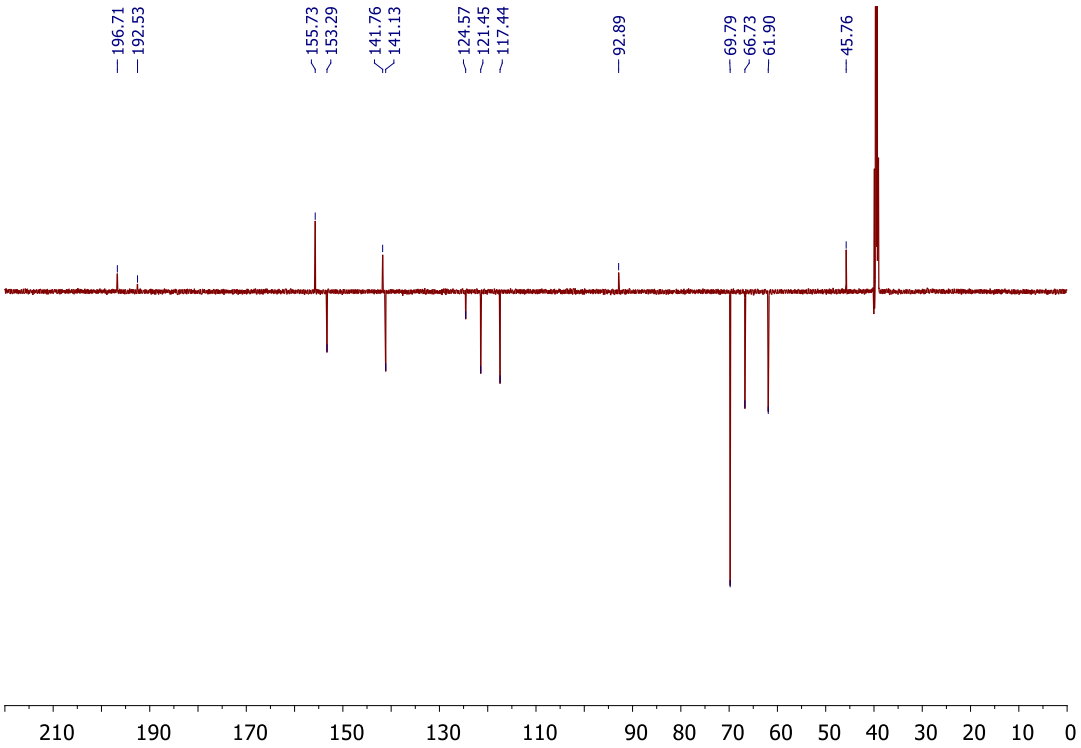

Figure S14. ^{13}C NMR spectrum of 4a$_{Re}$ (DMSO-*d*$_6$)

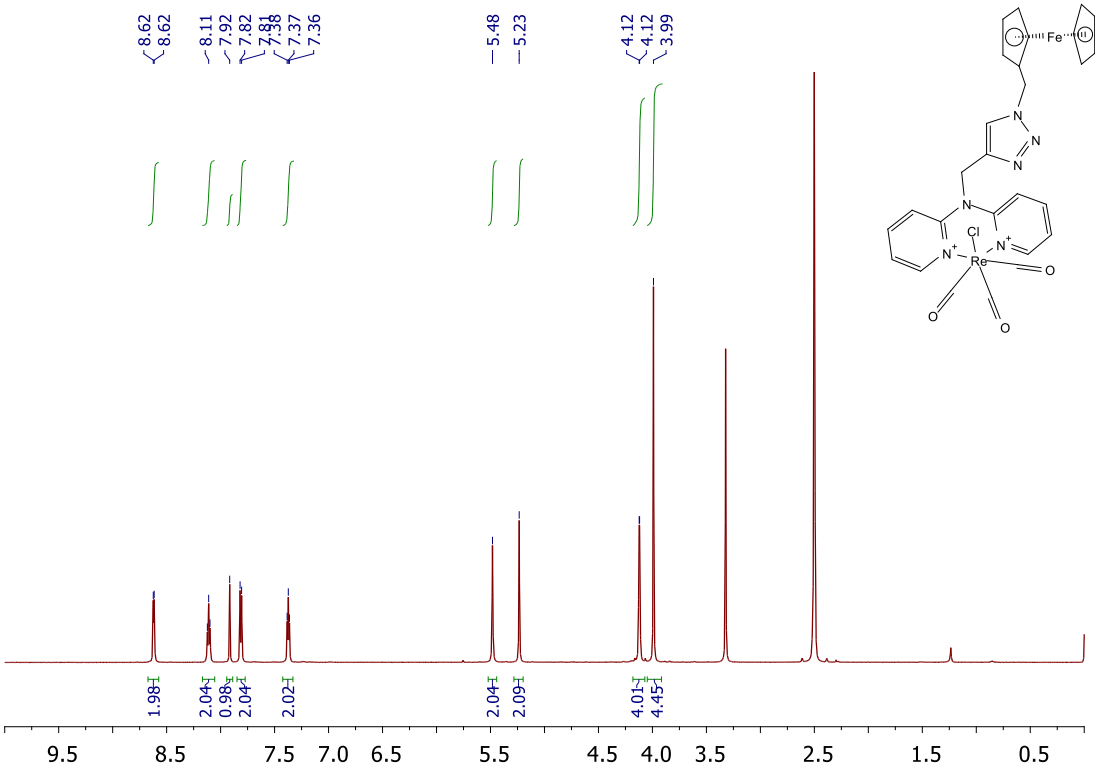

Figure S15. ^{1}H NMR spectrum of 4b$_{Re}$ (DMSO-*d*$_6$)

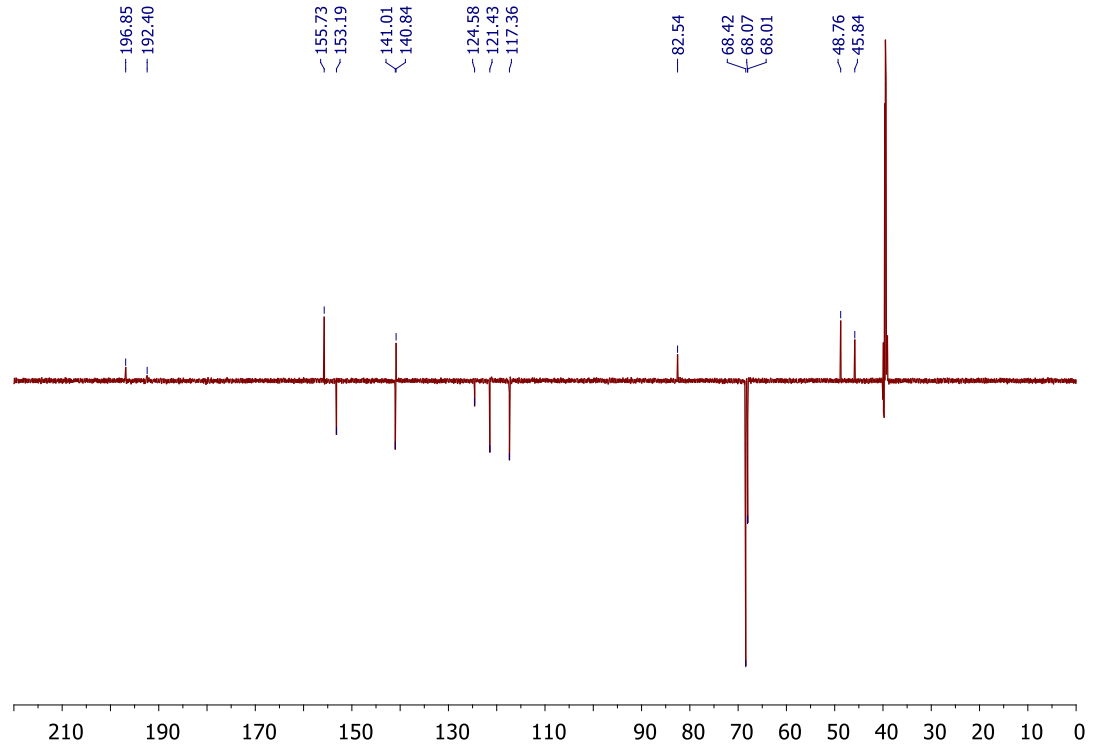

Figure S16. ^{13}C NMR spectrum of 4b$_{Re}$ (DMSO-*d*$_6$)

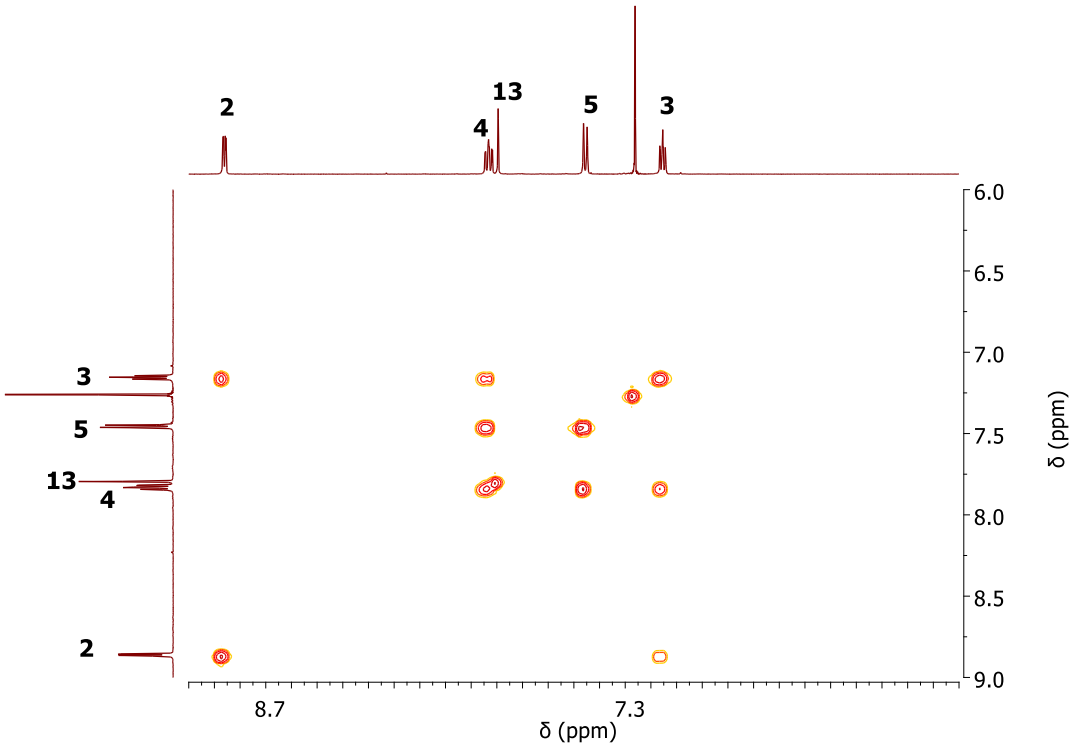

Figure S17. ^{1}H-^{1}H COSY NMR spectrum of $4b_{Re}$ ($CDCl_3$)

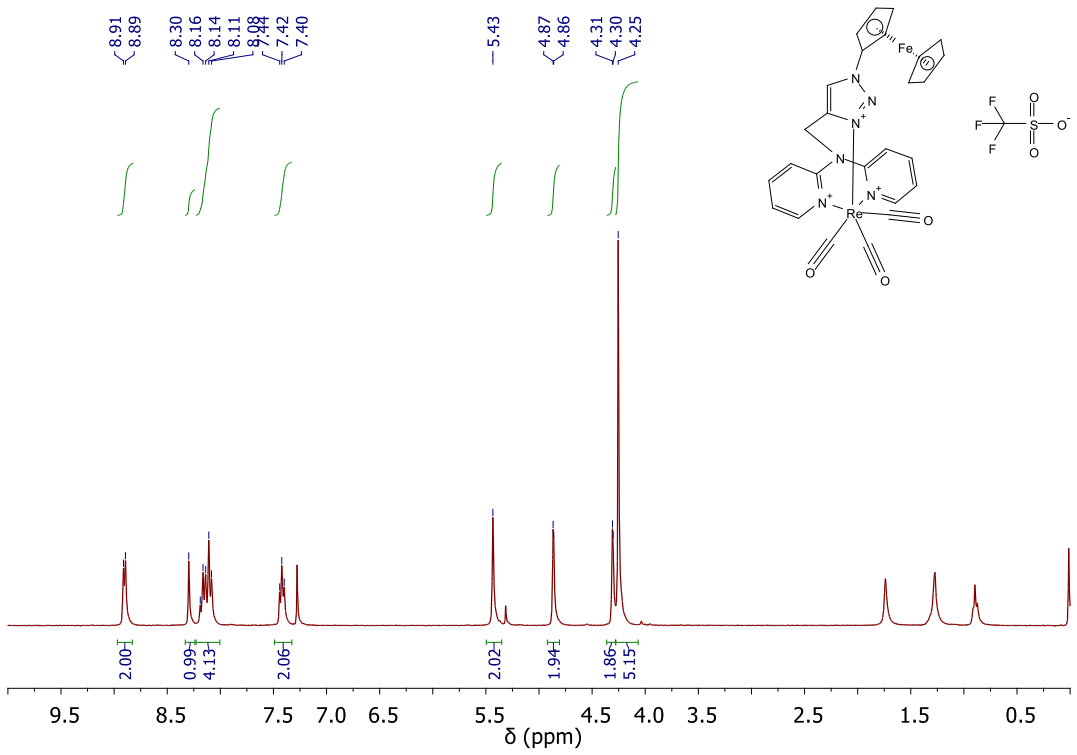

Figure S18. ^{1}H NMR spectrum of 4a$_{Re}$·OTf (CDCl$_3$)

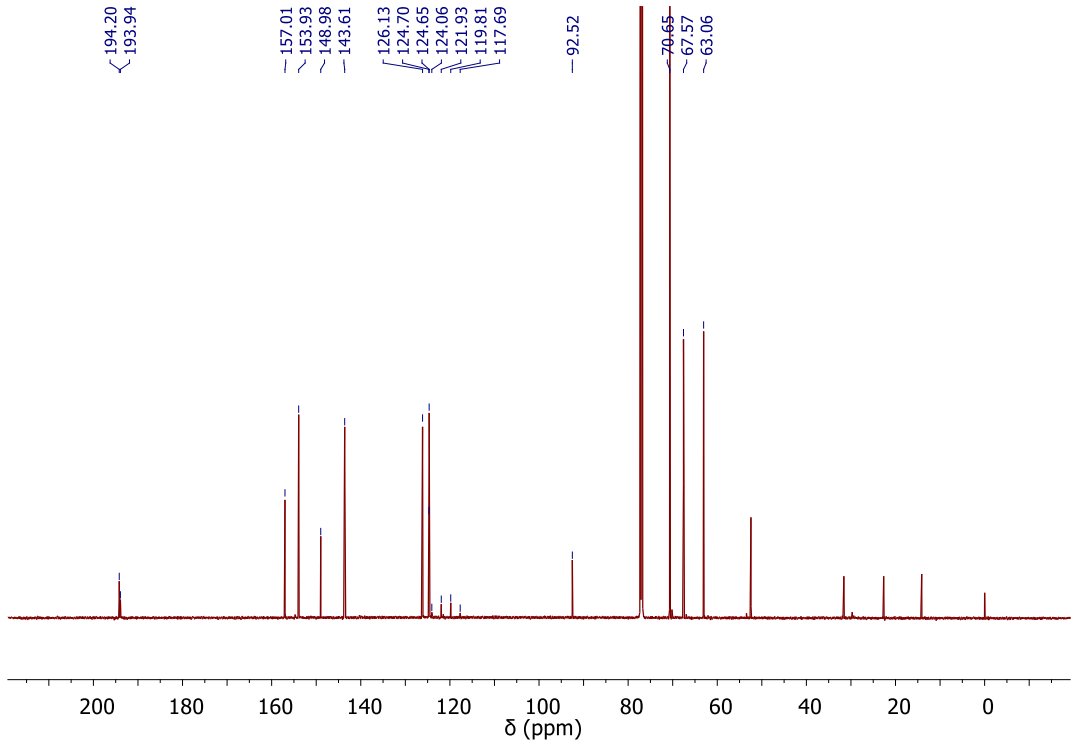

Figure S19. ^{13}C NMR spectrum of 4a$_{Re}$·OTf (CDCl$_3$)

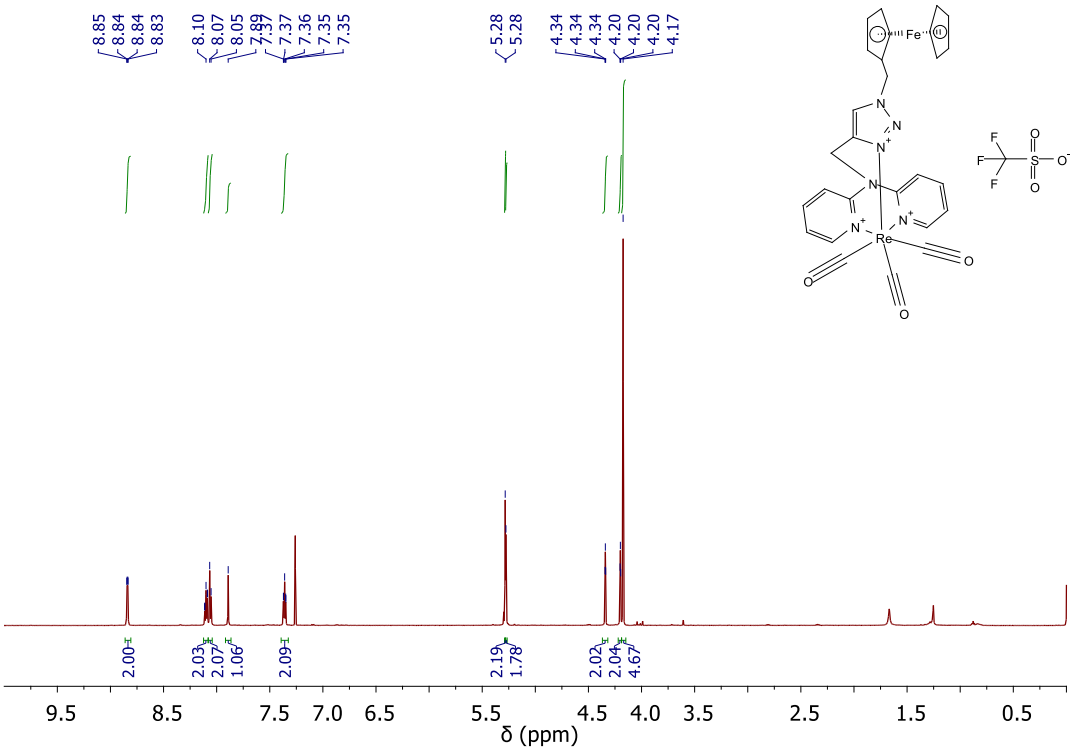

Figure S20. ^{1}H NMR spectrum of 4b$_{Re}$·OTf (CDCl$_3$)

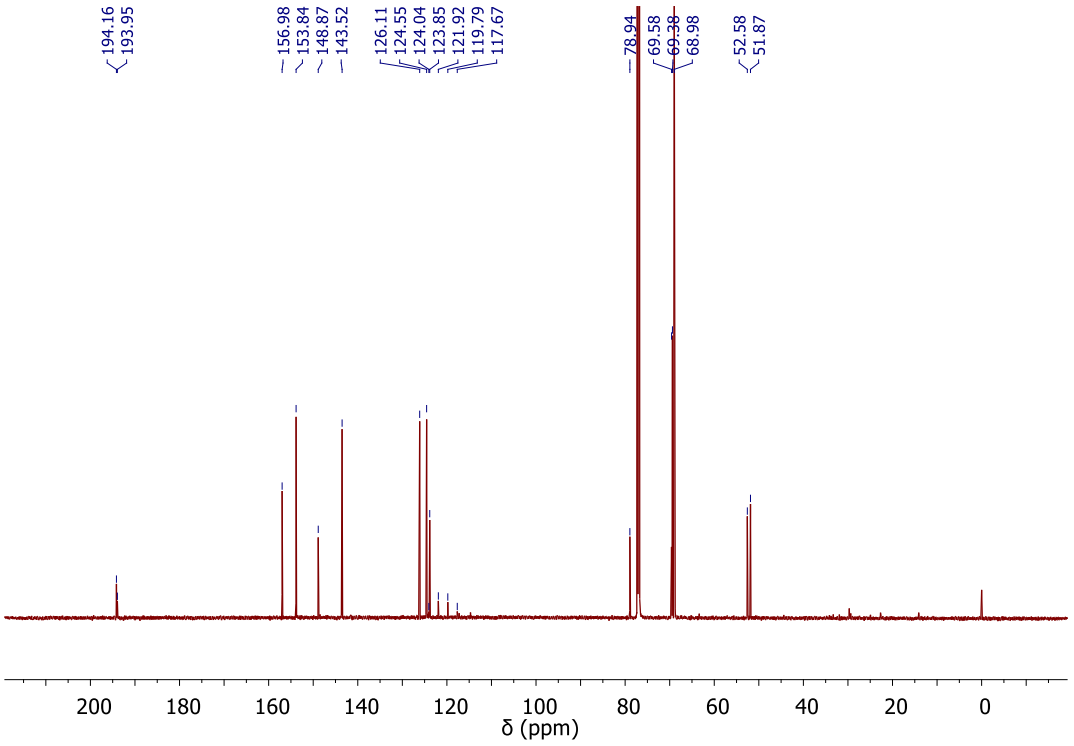

Figure S21. ^{13}C NMR spectrum of 4b$_{Re}$·OTf (CDCl$_3$)

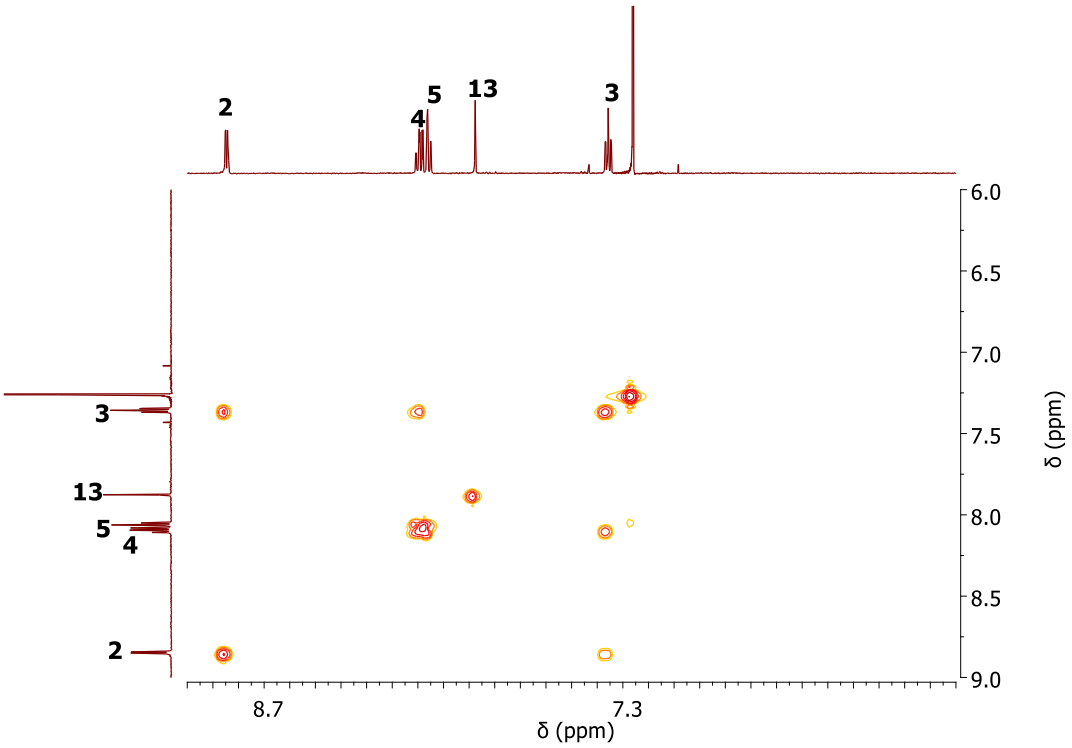

Figure S22. COSY NMR spectrum of $4b_{Re}$·OTf ($CDCl_3$)

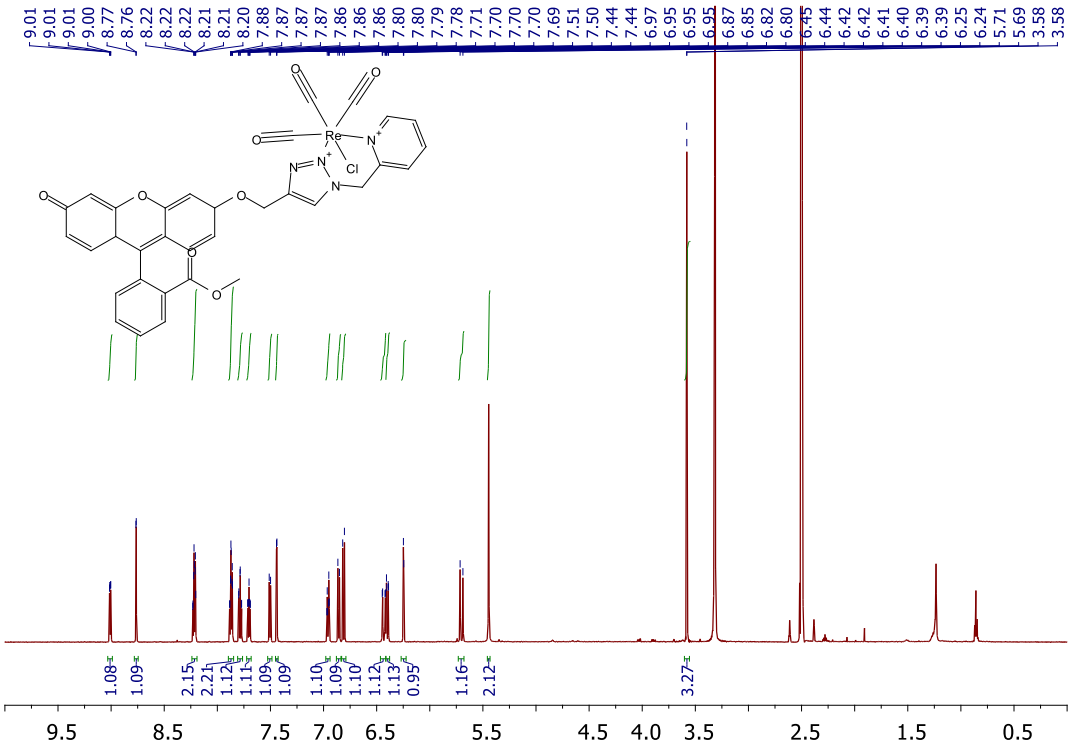

Figure S23. ^{1}H NMR spectrum of 6a$_{Re}$ (DMSO-*d*$_6$)

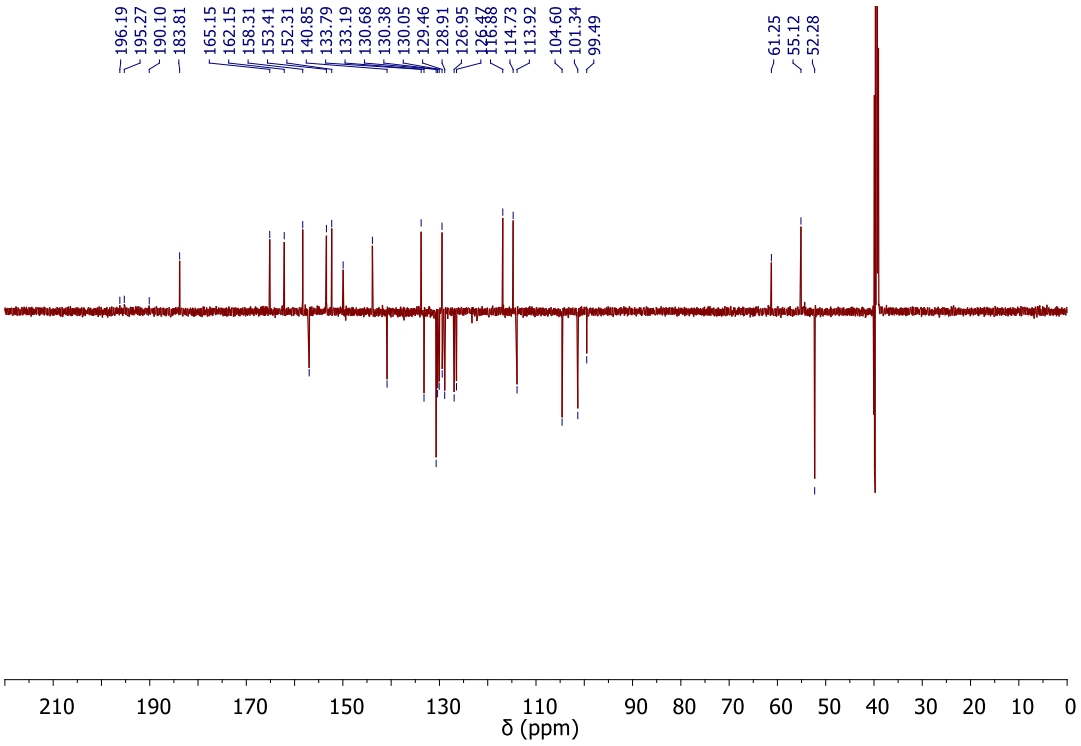

Figure S24. ^{13}C NMR spectrum of 6a$_{Re}$ (DMSO-*d*$_6$)

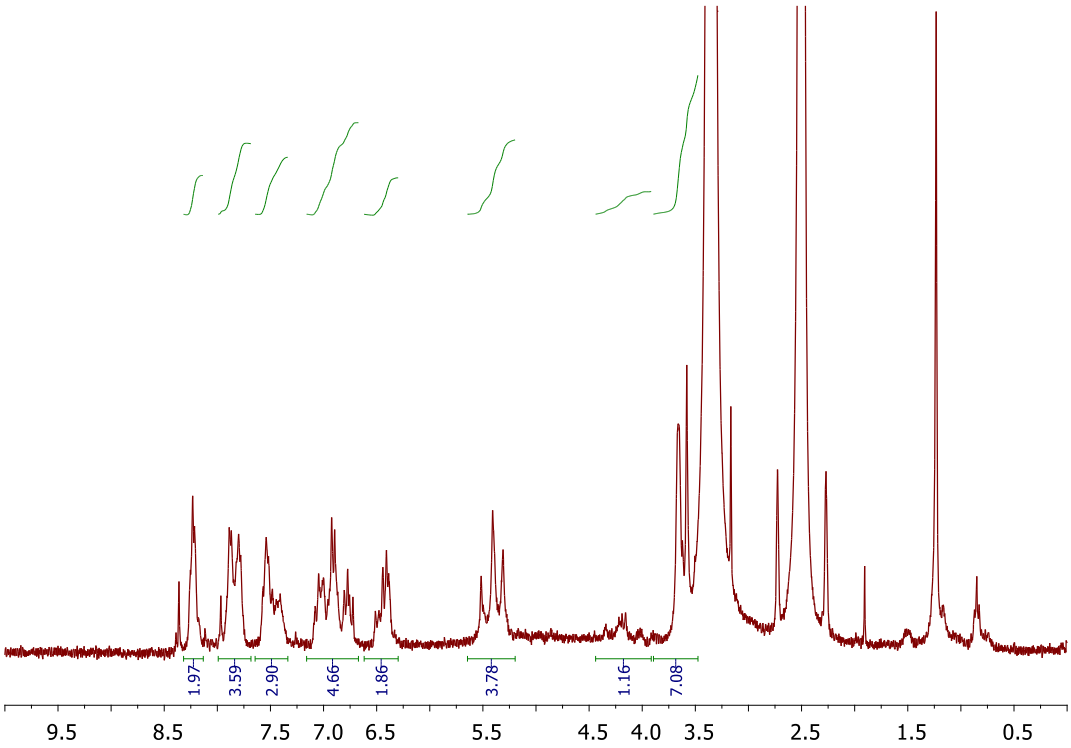

Figure S25. ^{1}H NMR spectrum of 6b$_{Re}$ (DMSO-*d*$_6$)

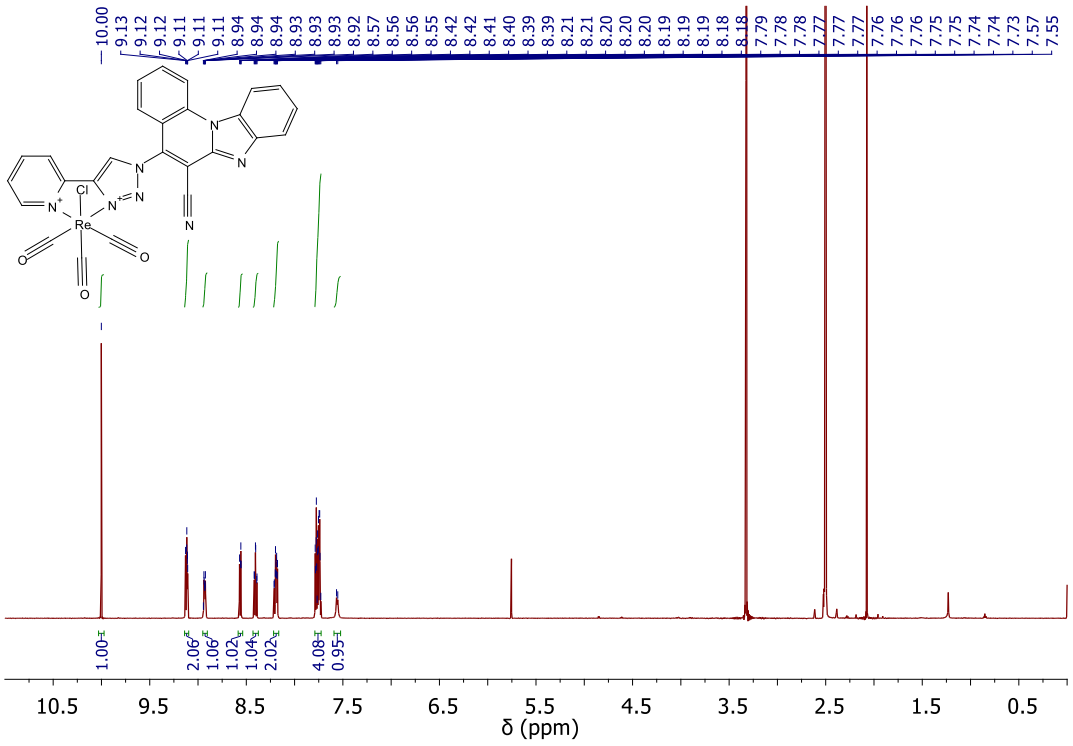

Figure S26. ^{1}H NMR spectrum of 9_{Re} (DMSO-d_6)

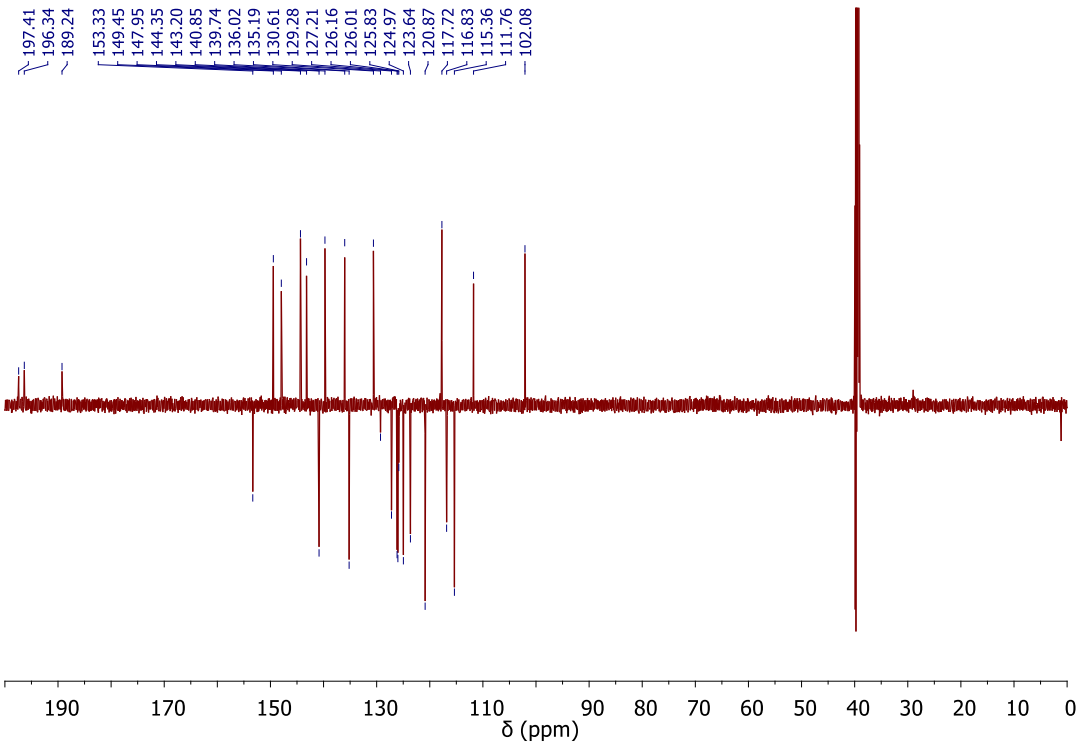

Figure S27. ^{13}C NMR spectrum of 9_{Re} (DMSO-d_6)

4. NMR spectra of ligands

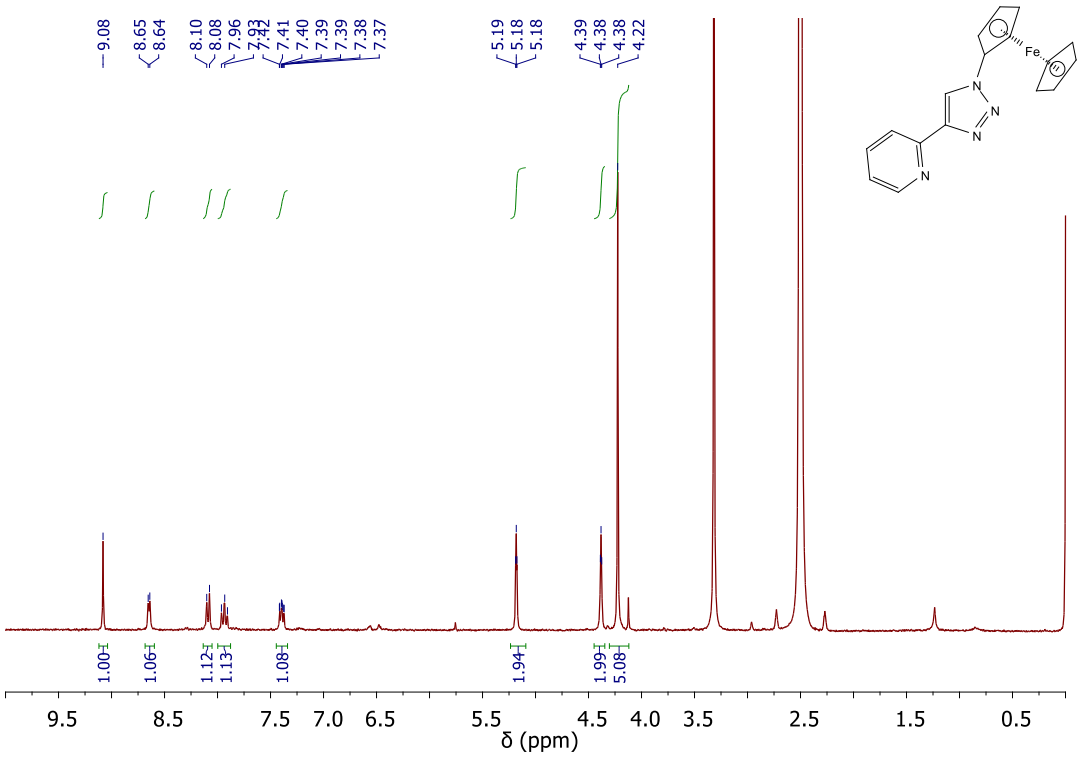

Figure S28. ^{1}H NMR spectrum of 2a (DMSO-d_6)

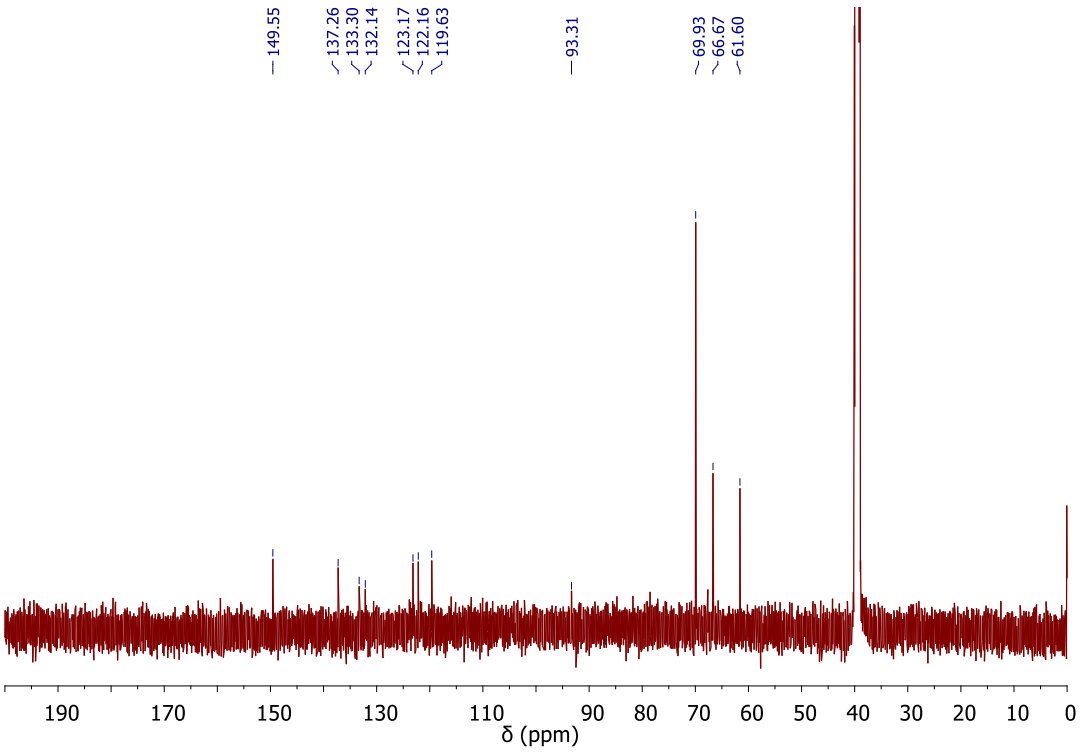

Figure S29. ^{13}C NMR spectrum of 2a (DMSO-d_6)

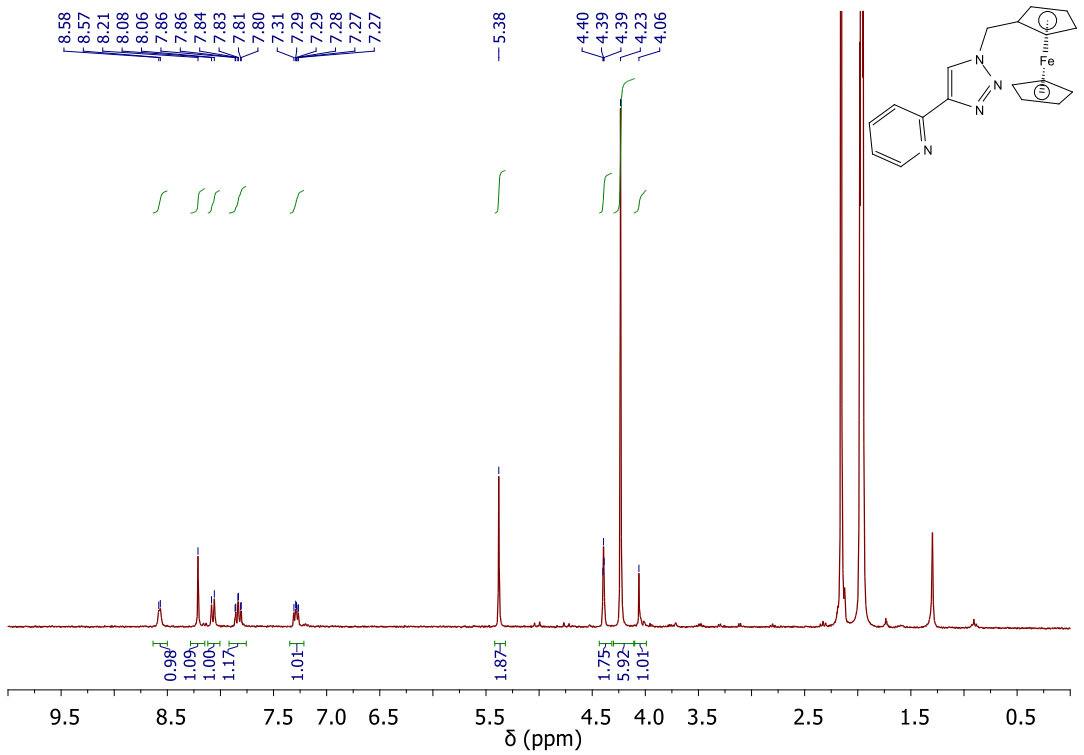

Figure S30. ^{1}H NMR spectrum of 2b (ACN-d_3)

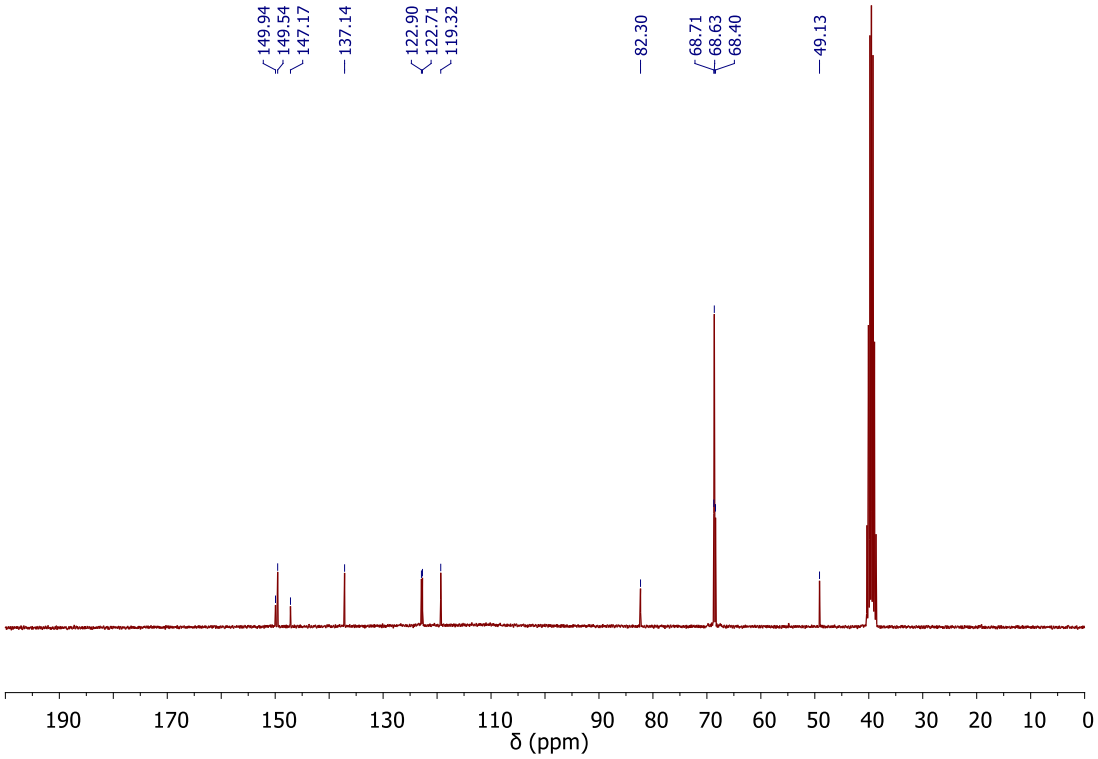

Figure S31. ^{13}C NMR spectrum of 2b (DMSO)

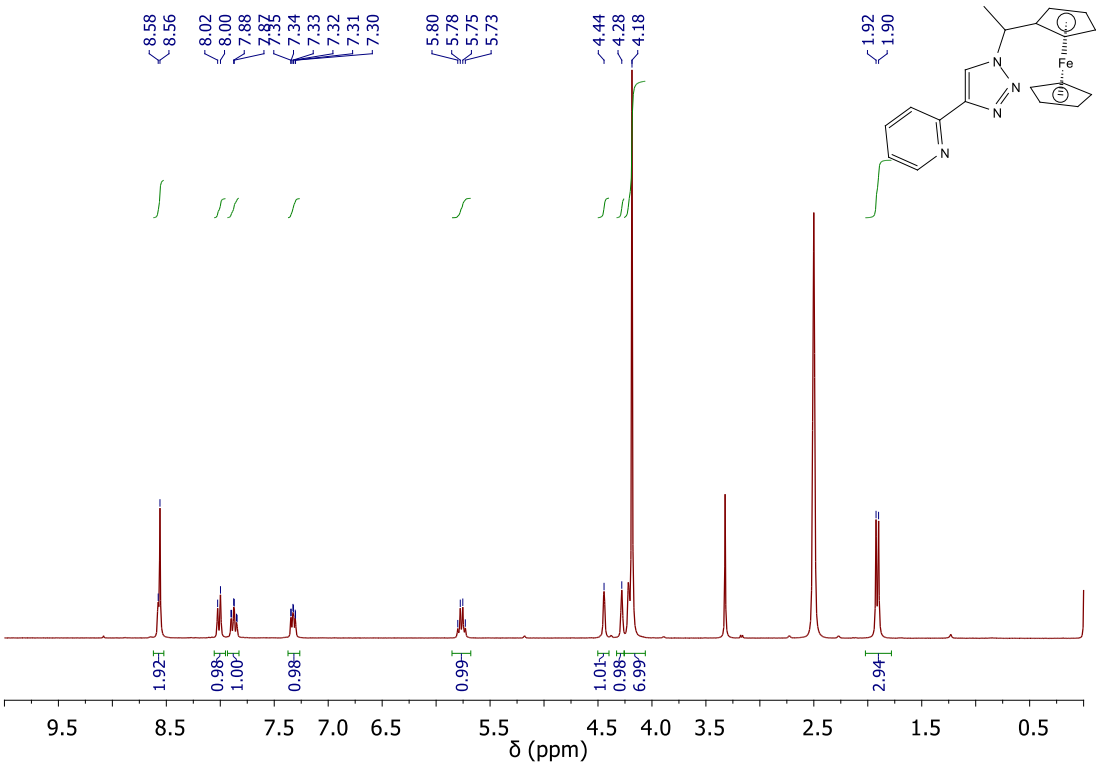

Figure S32. ^{1}H NMR spectrum of 2c (DMSO-d_6)

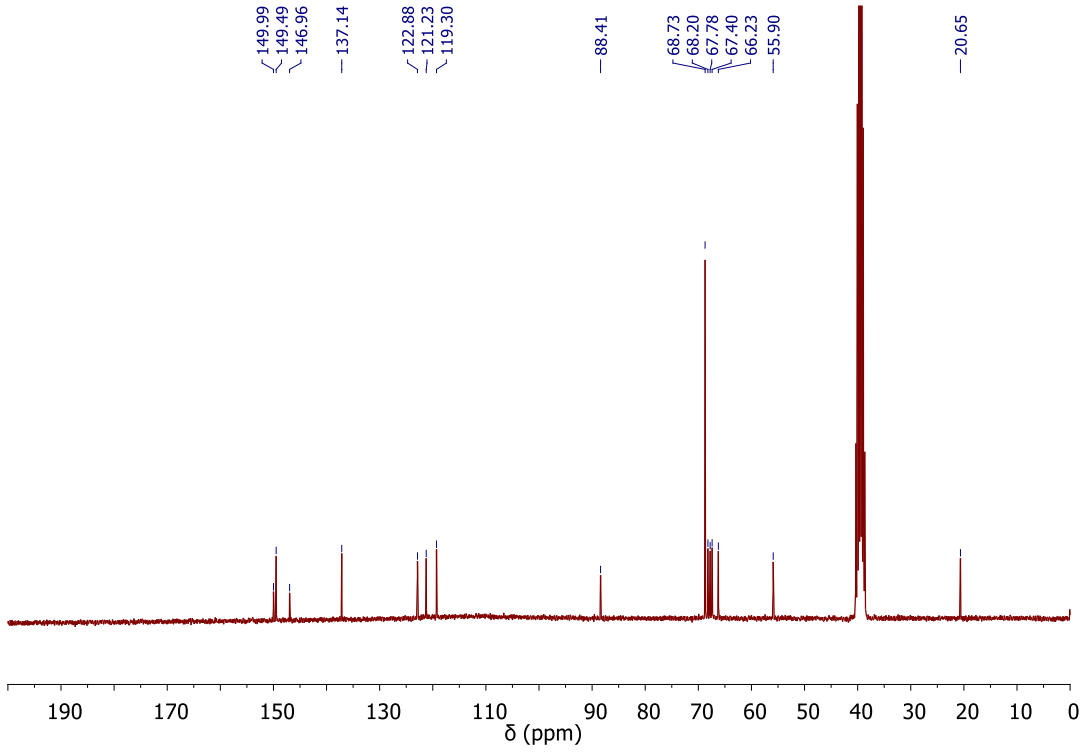

Figure S33. ^{13}C NMR spectrum of 2c (DMSO-d_6)

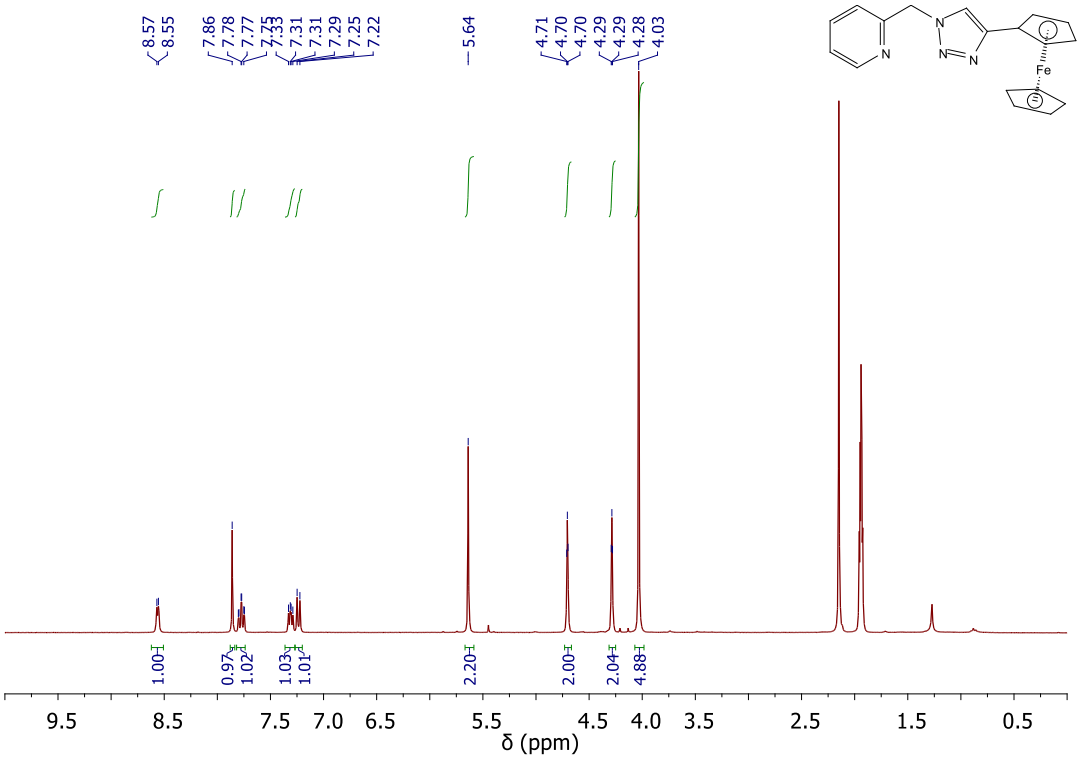

Figure S34. ^{1}H NMR spectrum of 3 (ACN-d_3)

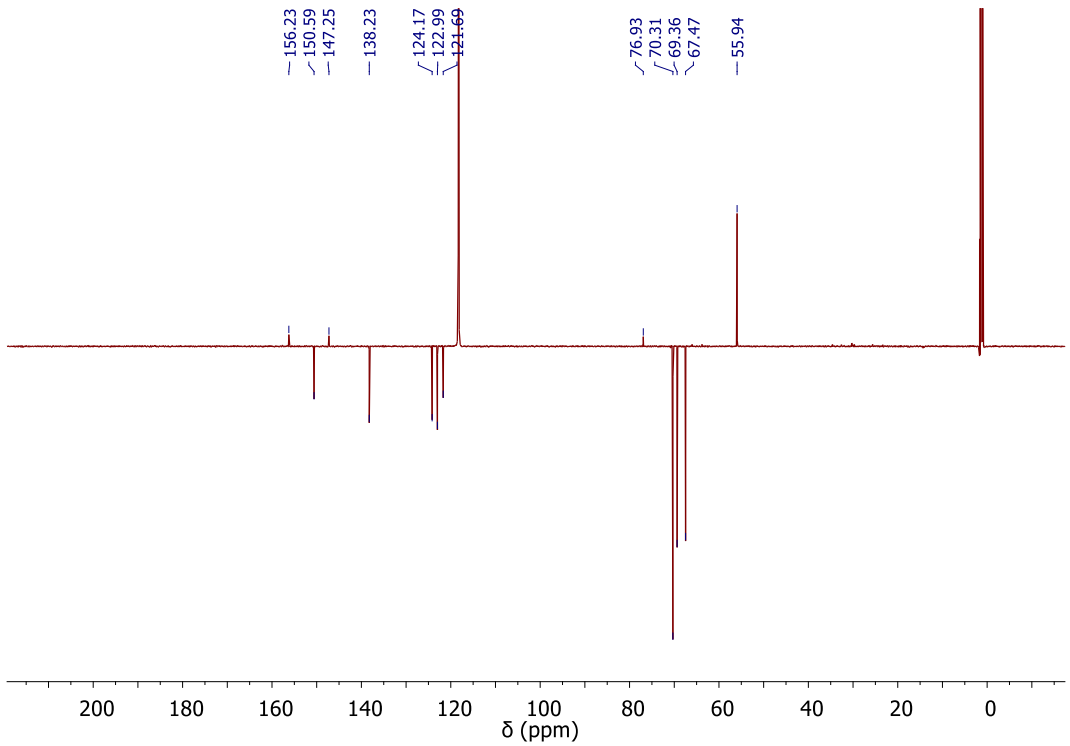

Figure S35. ^{13}C NMR spectrum of 3 (ACN-d_3)

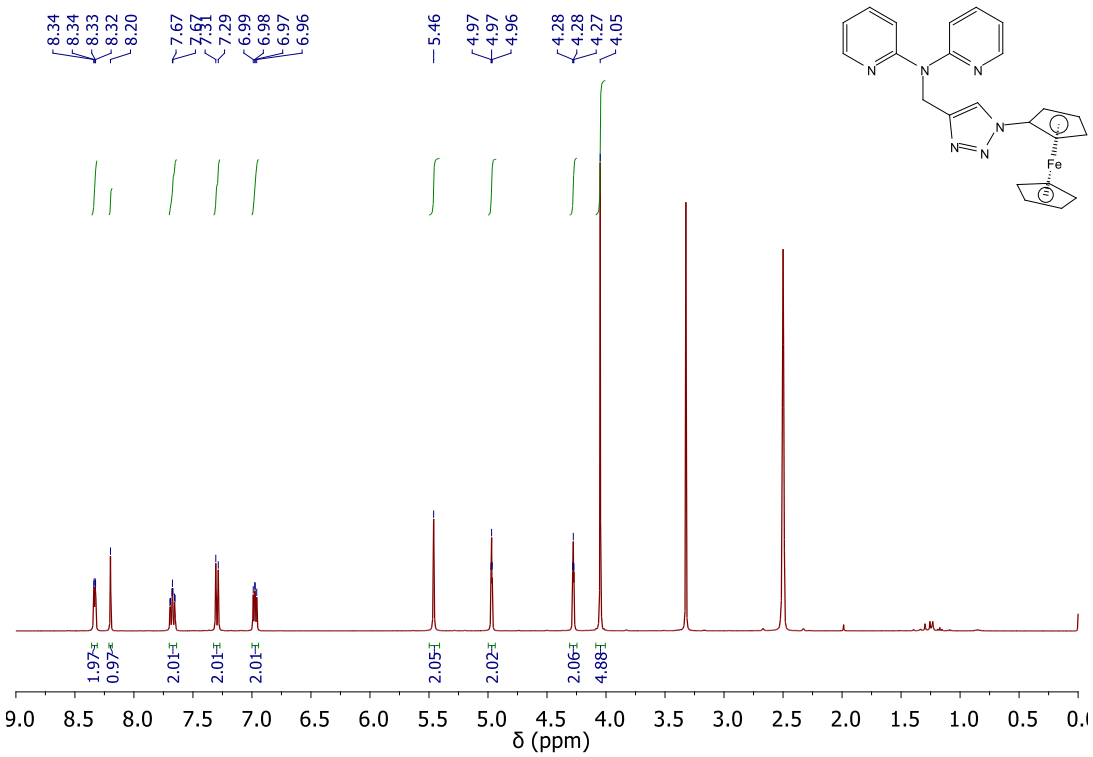

Figure S36. ^{1}H NMR spectrum of 4a (DMSO-d_6)

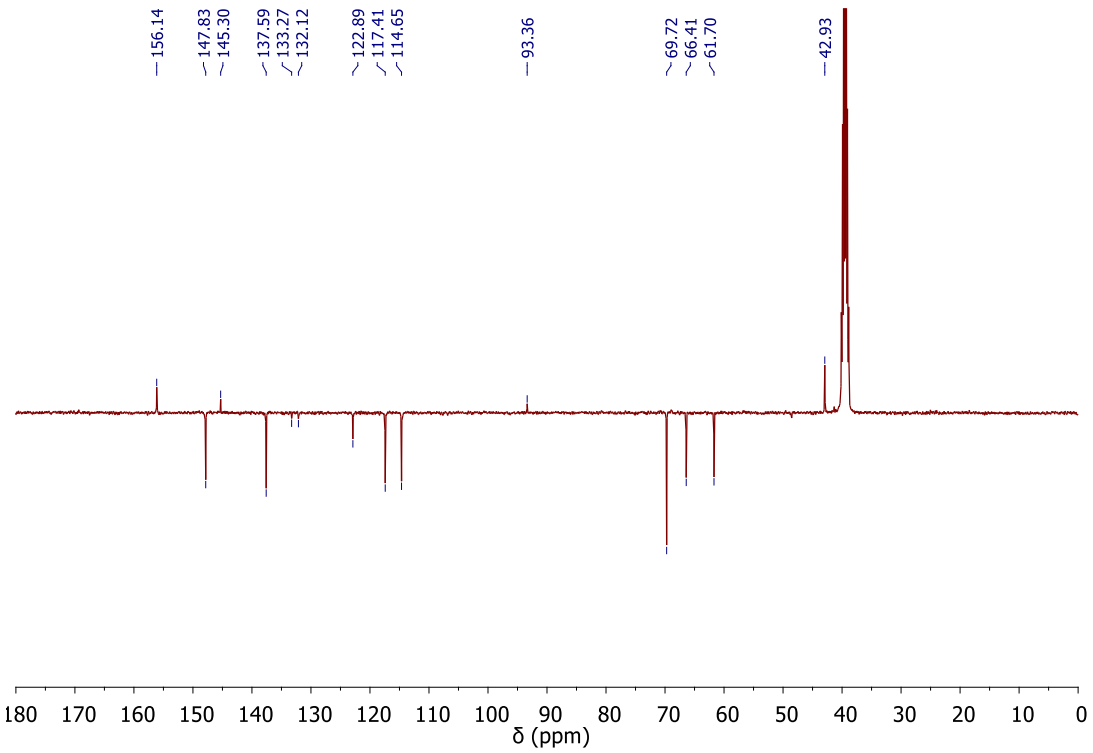

Figure S37. ^{13}C NMR spectrum of 4a (DMSO-d_6)

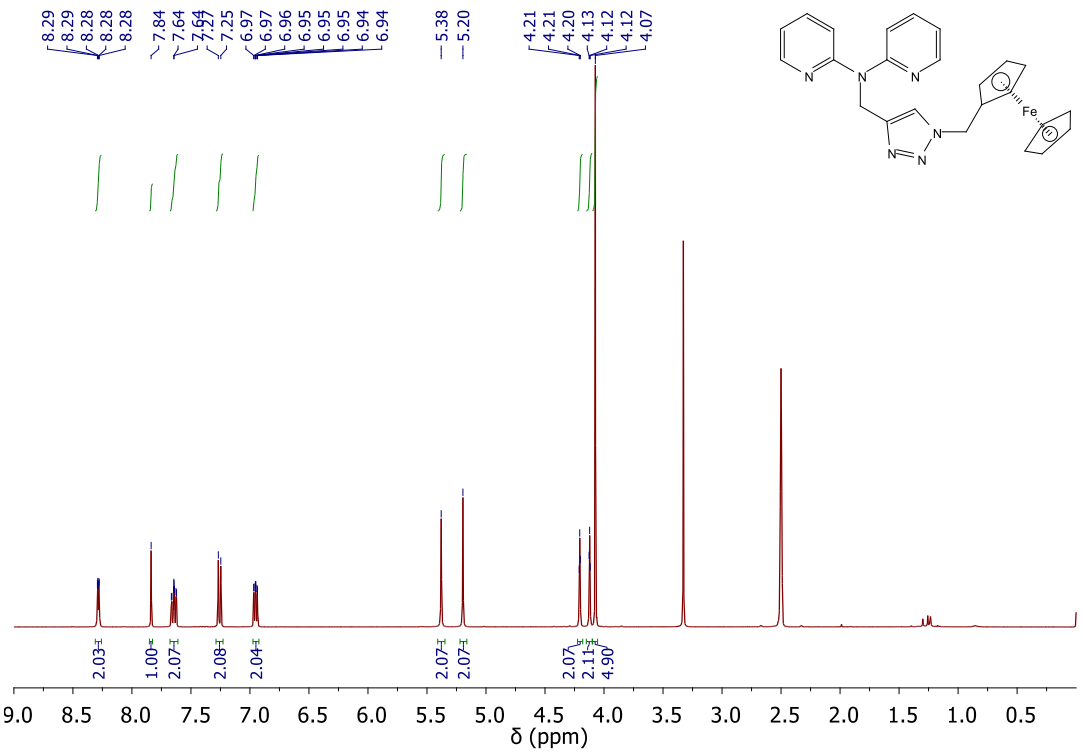

Figure S38. ^{1}H NMR spectrum of 4b (DMSO-d_6)

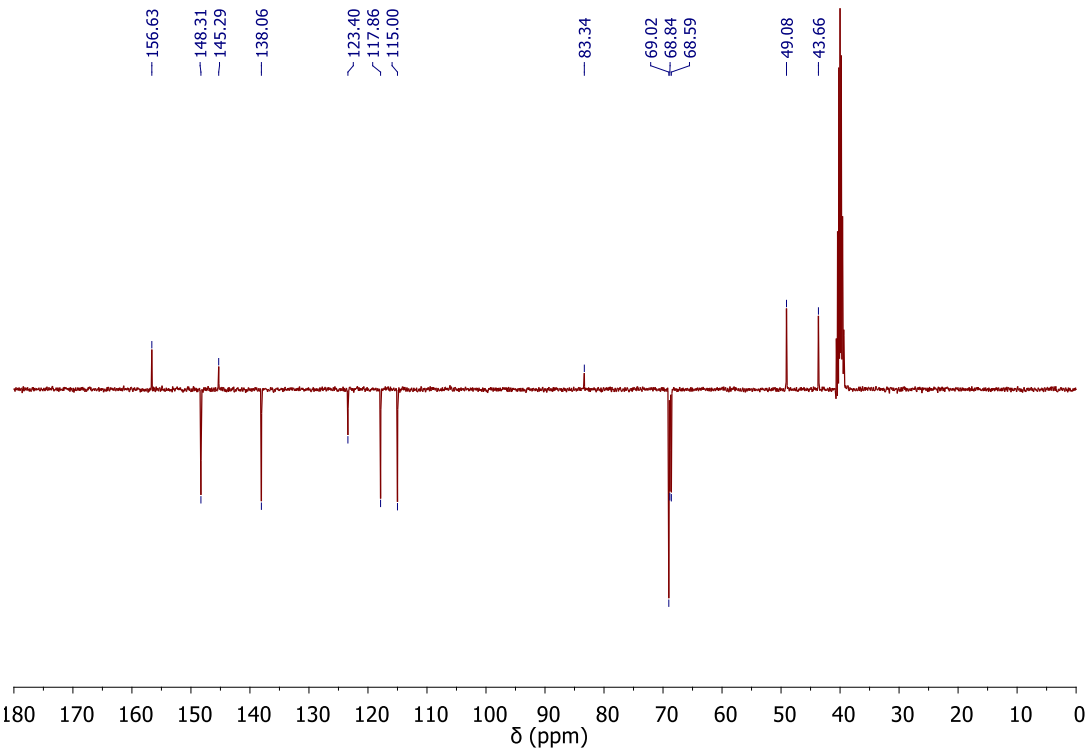

Figure S39. ^{13}C NMR spectrum of 4b (DMSO-d_6)

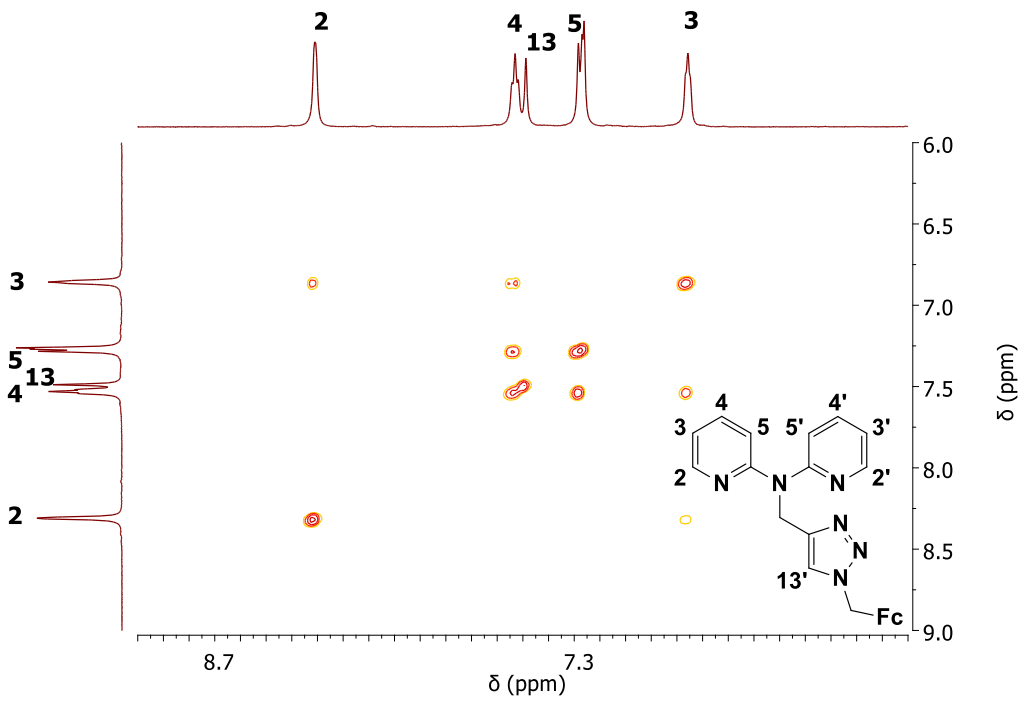

Figure S40. COSY NMR spectrum of 4b ($CDCl_3$)

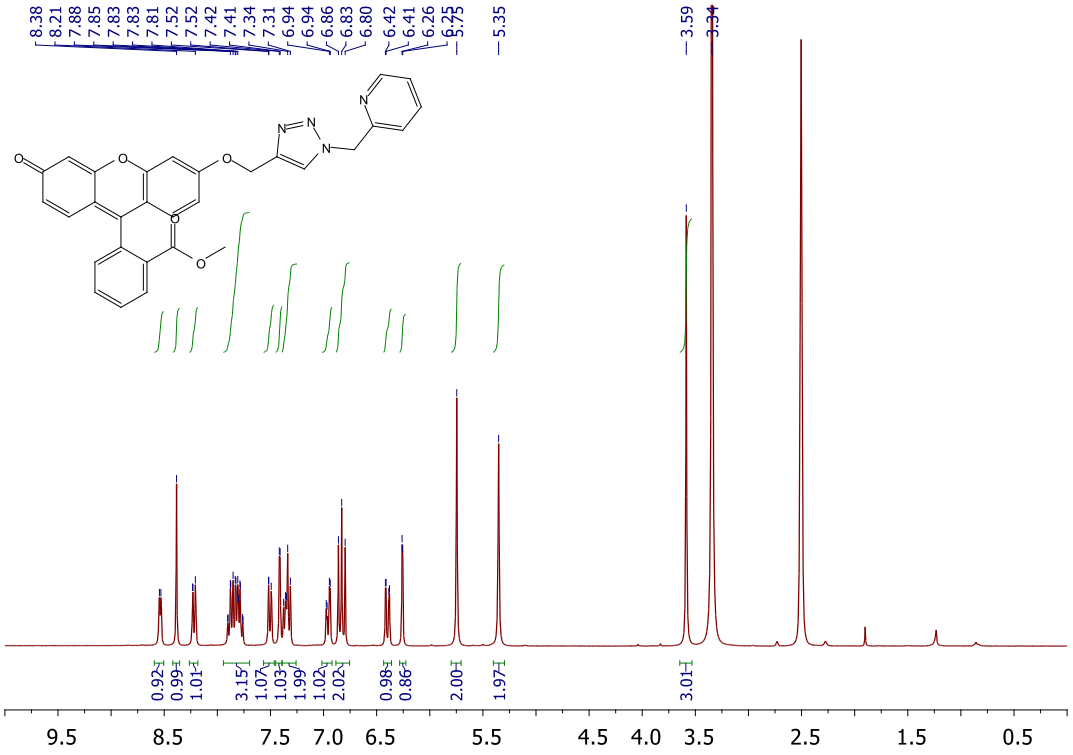

Figure S41. ^{1}H NMR spectrum of 6a (DMSO-d_6)

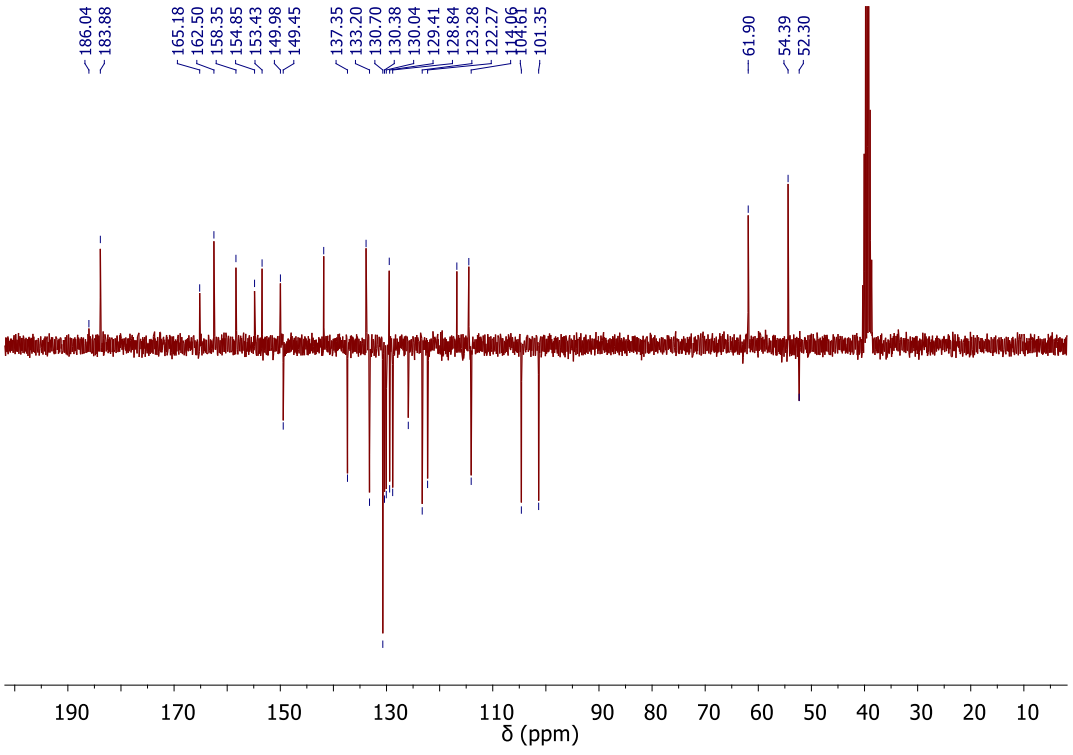

Figure S42. ^{13}C NMR spectrum of 6a (DMSO-d_6)

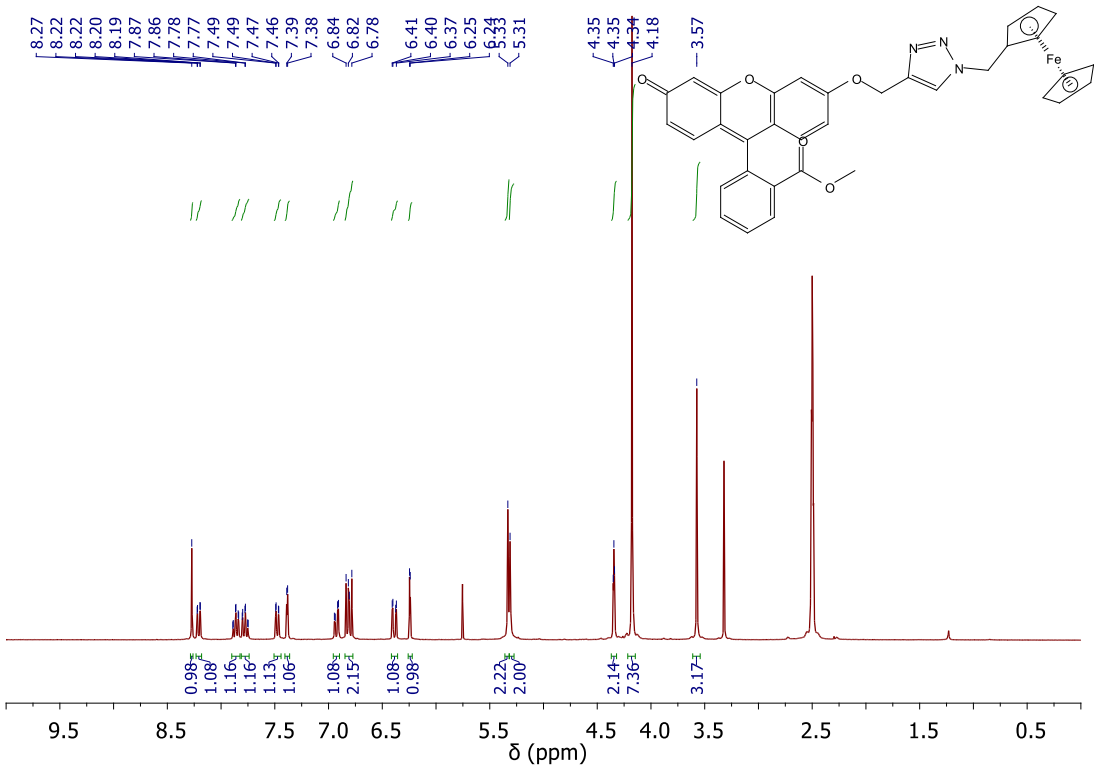

Figure S43. ^{1}H NMR spectrum of 6b (DMSO-d_6)

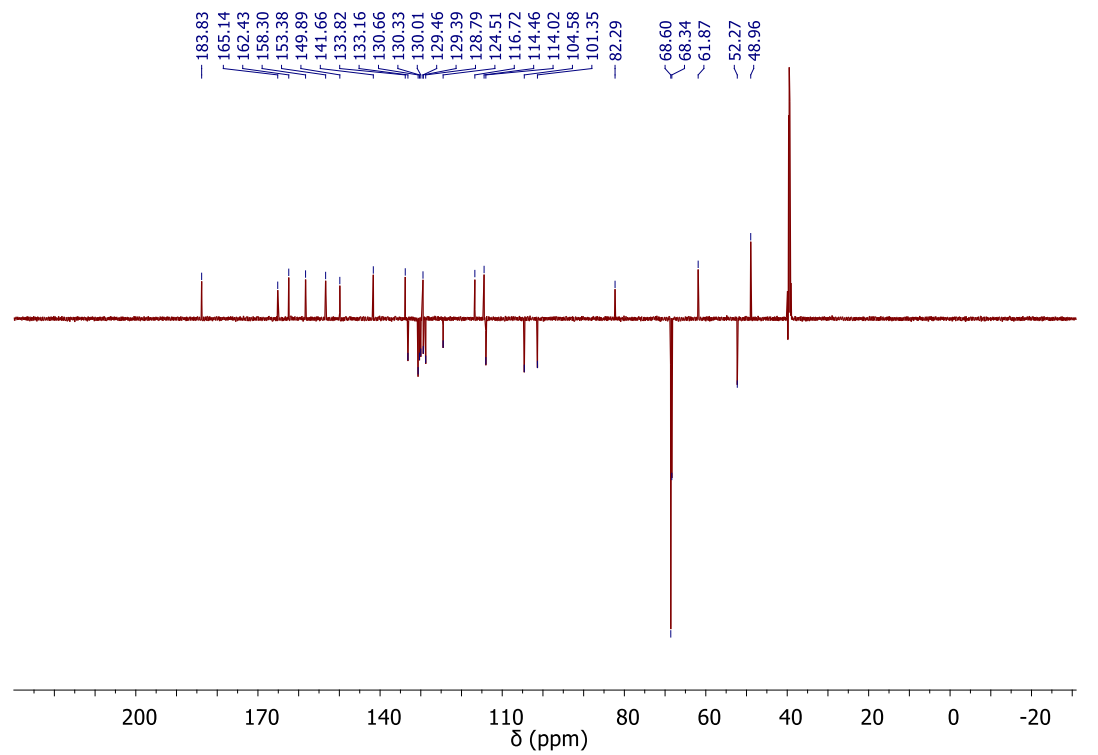

Figure S44. ^{13}C NMR spectrum of 6b (DMSO-d_6)

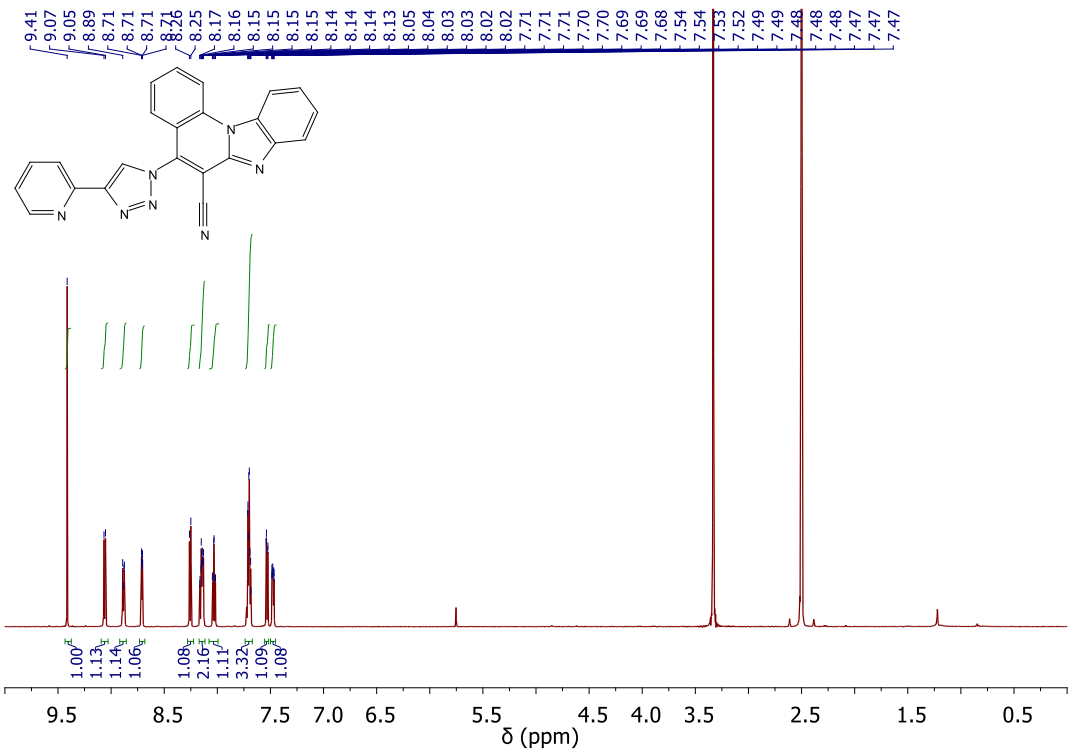

Figure S45. ^{1}H NMR spectrum of 9 (DMSO-d_6)

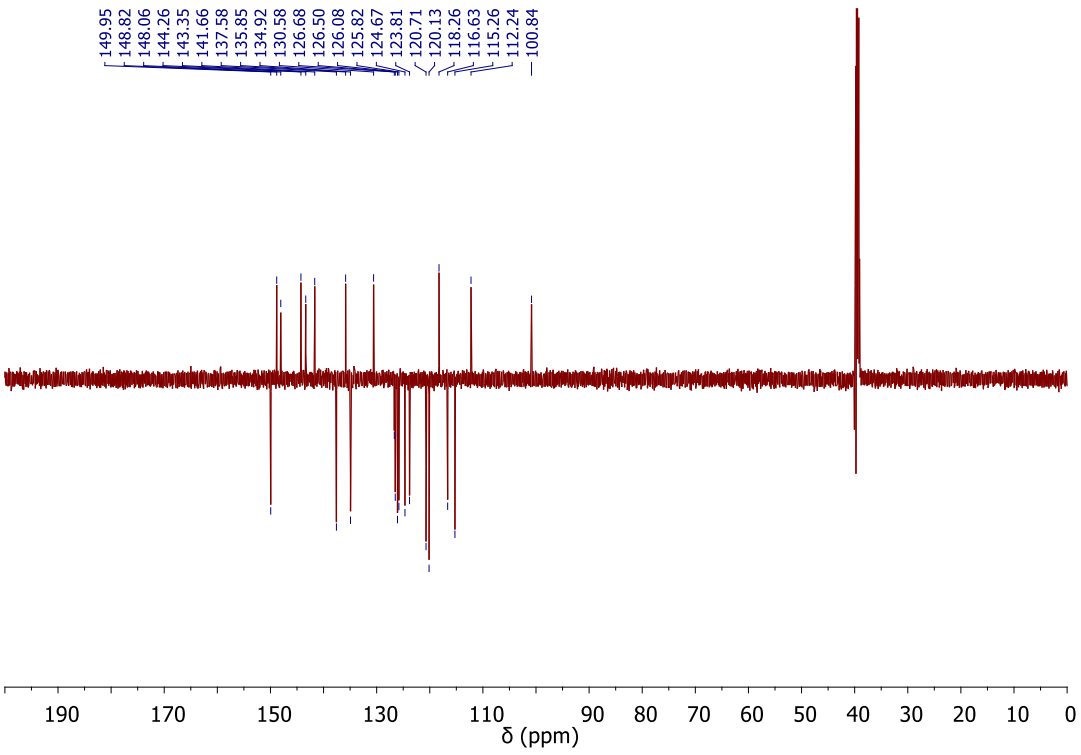

Figure S46. ^{13}C NMR spectrum of 9 (DMSO-d_6)

5. IR spectra

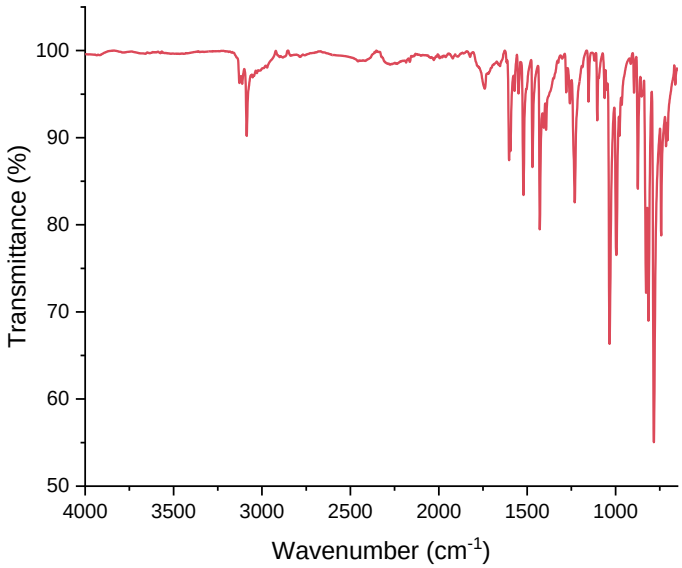

Figure S47. IR (ATR) spectrum of 2a

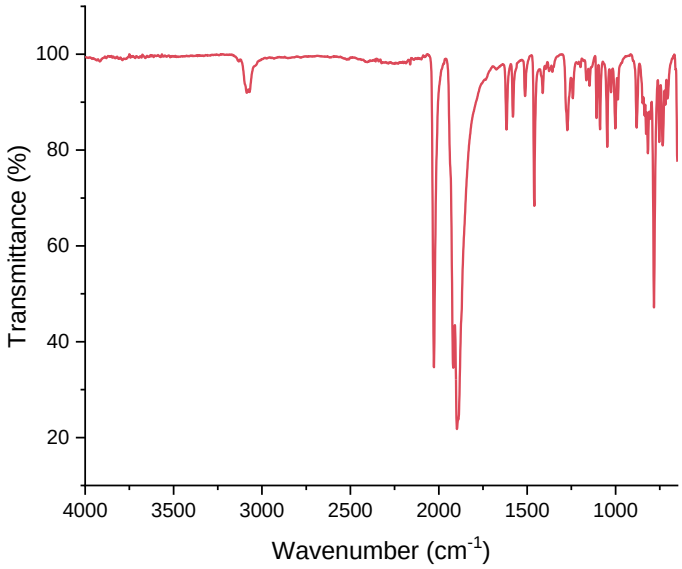

Figure S48. IR (ATR) spectrum of $2a_{Re}$

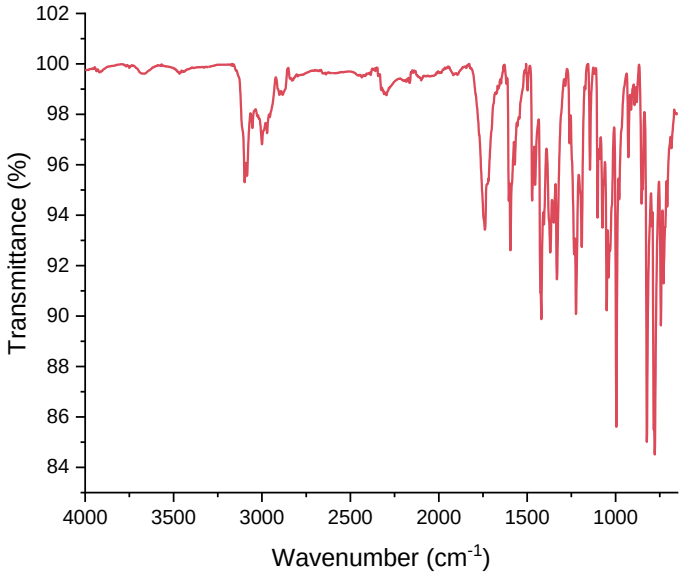

Figure S49. IR (ATR) spectrum of 2b

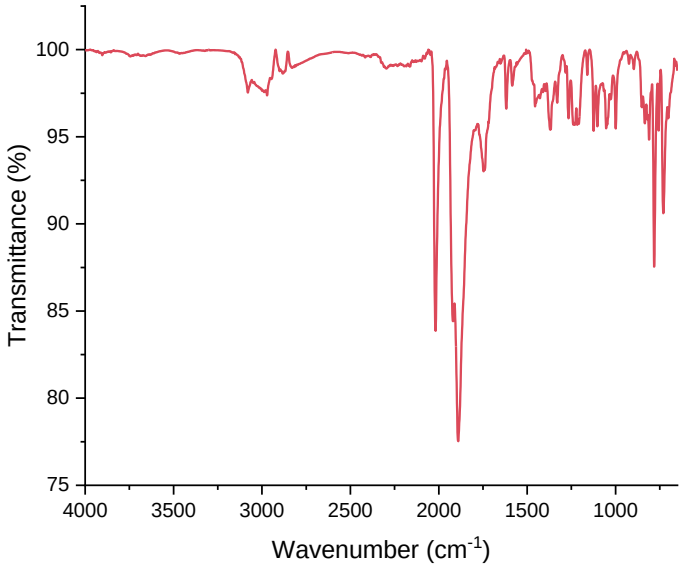

Figure S50. IR (ATR) spectrum of $2b_{Re}$

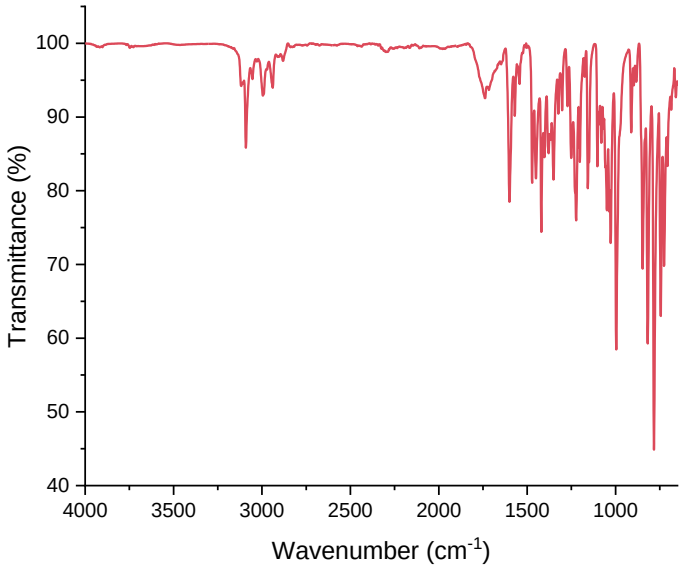

Figure S51. IR (ATR) spectrum of 2c

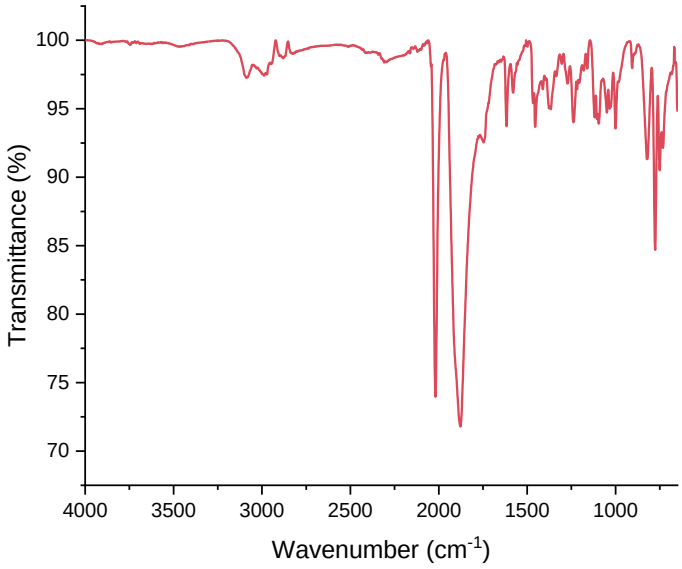

Figure S52. IR (ATR) spectrum of $2c_{Re}$

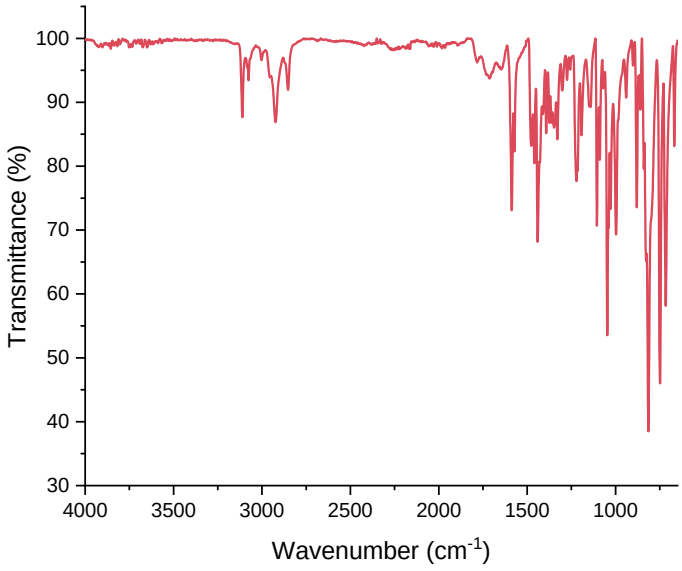

Figure S53. IR (ATR) spectrum of 3

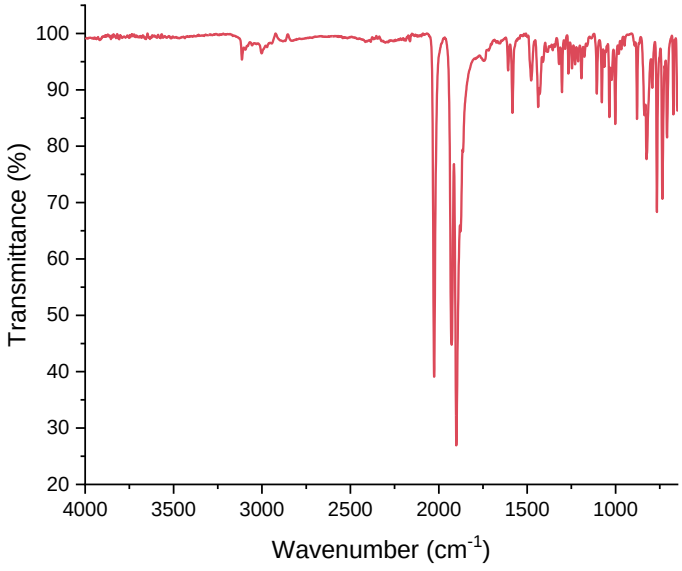

Figure S54. IR (ATR) spectrum of 3_{Re}

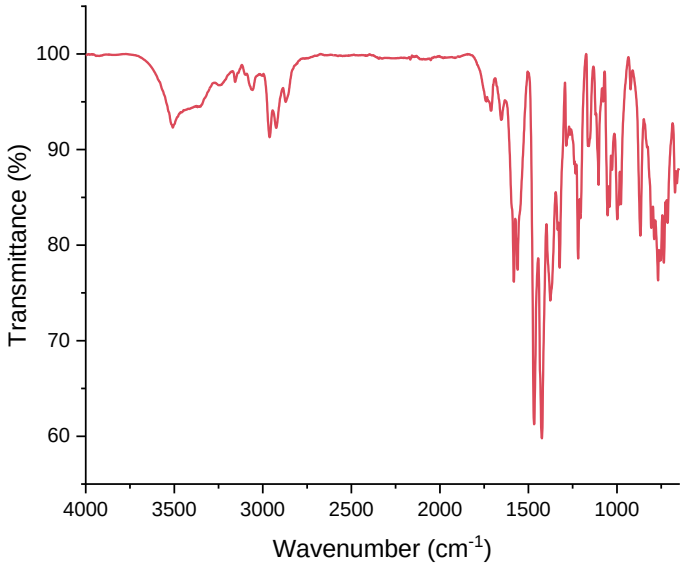

Figure S55. FTIR (ATR) spectrum of 4b

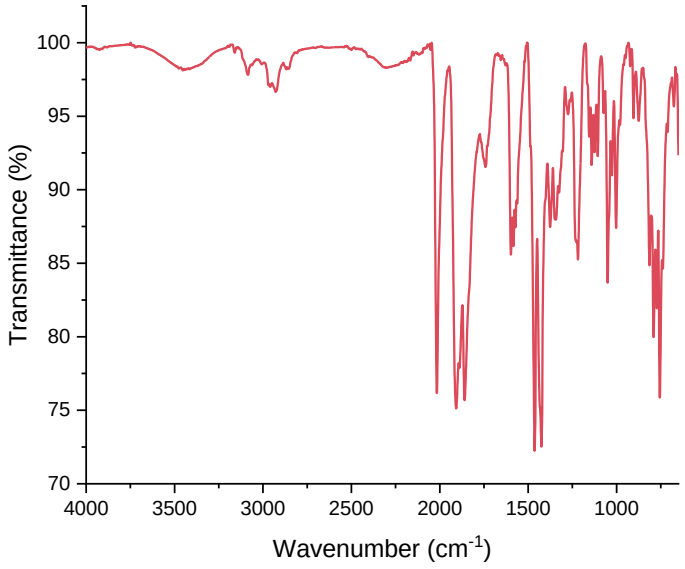

Figure S56. FTIR (ATR) spectrum of $4b_{Re}$

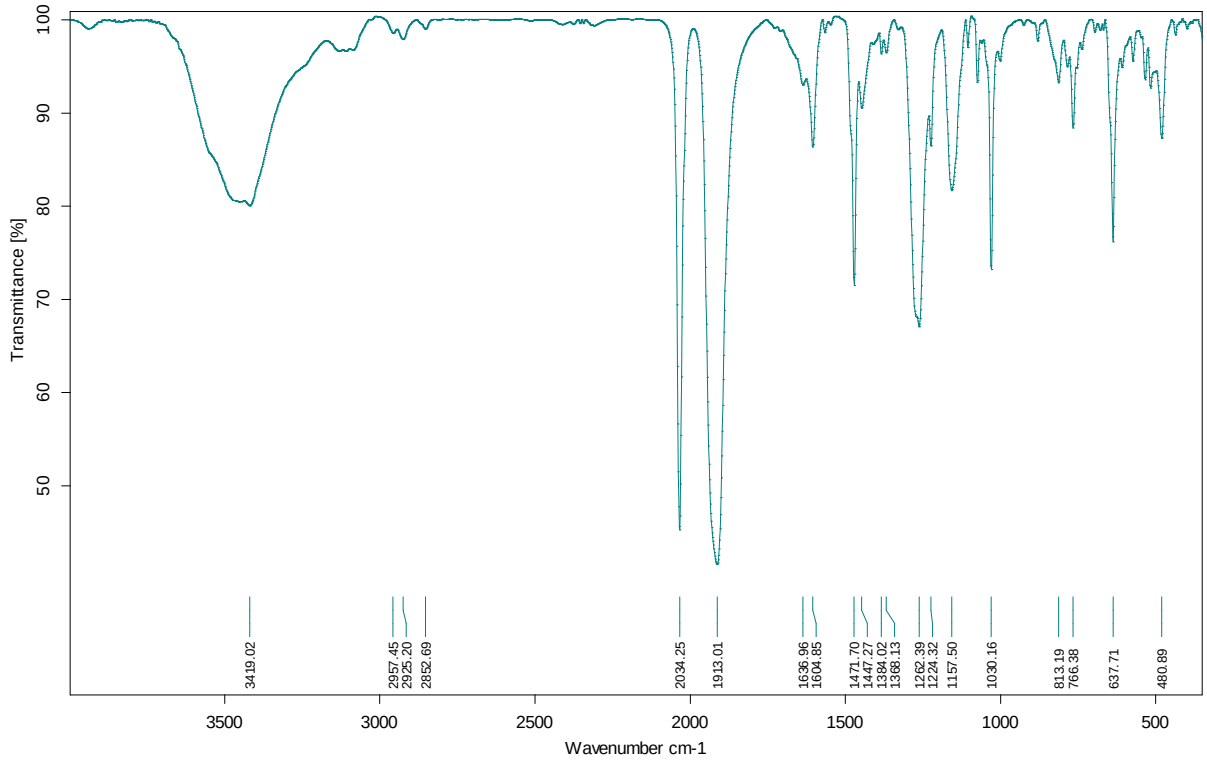

Figure S57. IR (KBr) spectrum of $4b_{Re}$·OTf

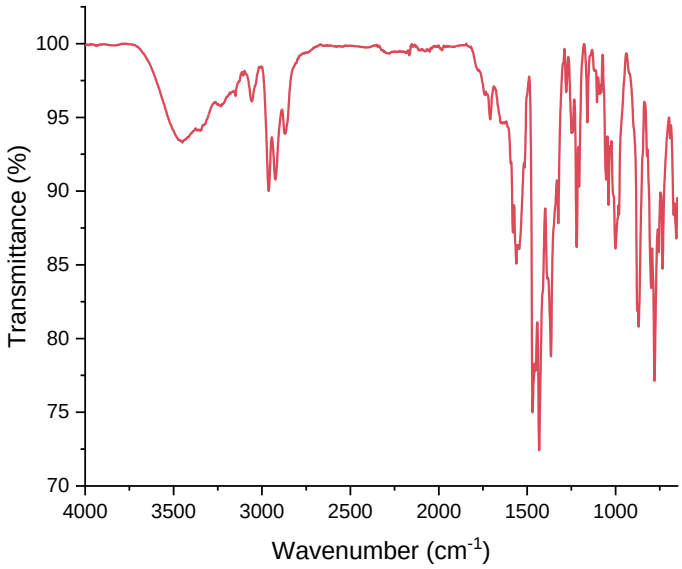

Figure S58. IR (ATR) spectrum of 4a

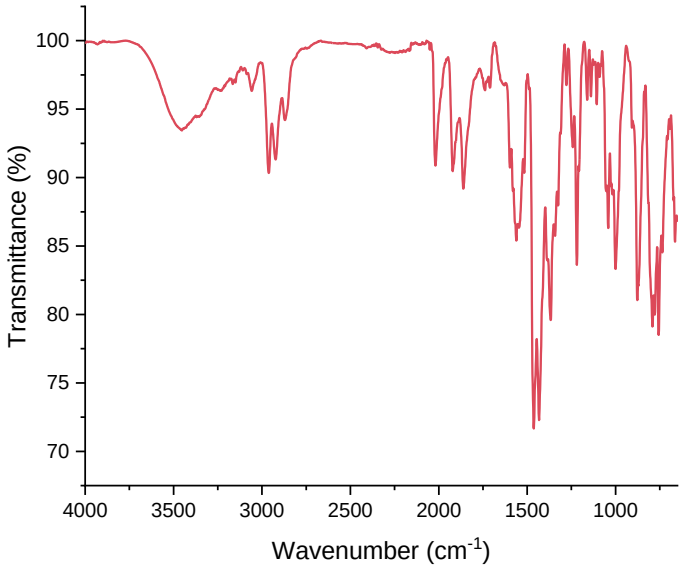

Figure S59. IR (ATR) spectrum of $4a_{Re}$

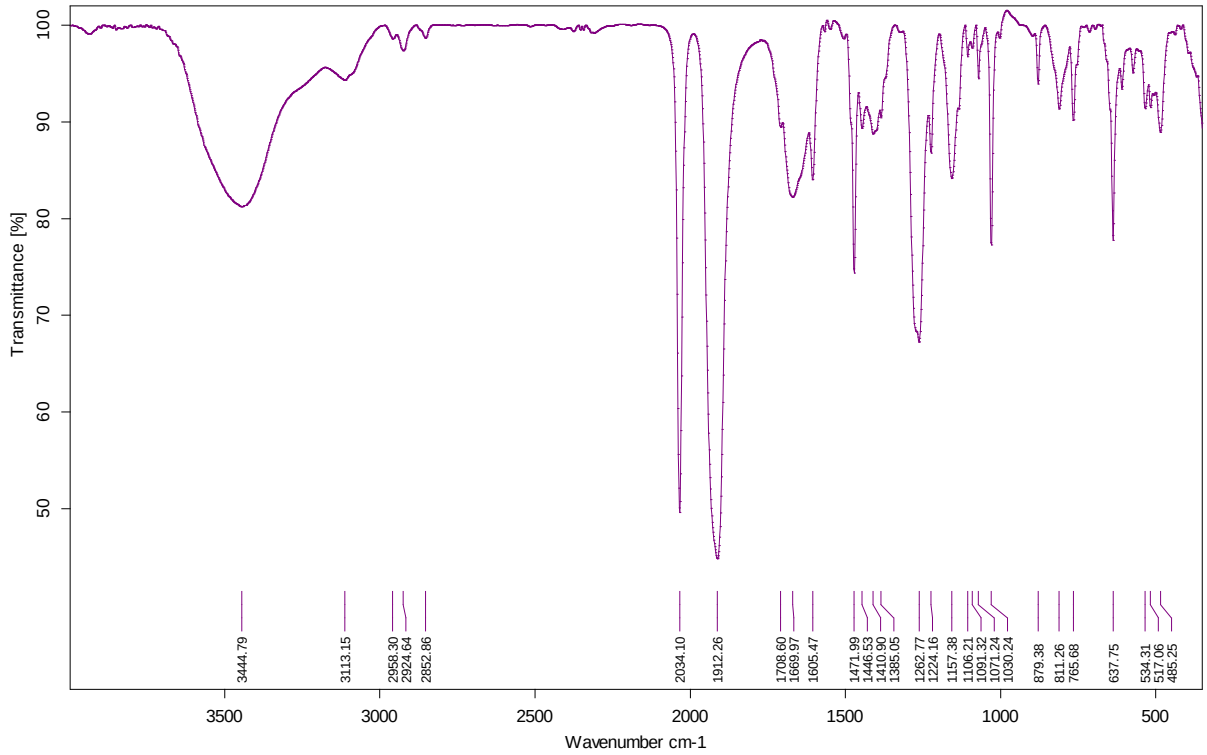

Figure S60. IR (KBr) spectrum of $4a_{Re}$·OTf

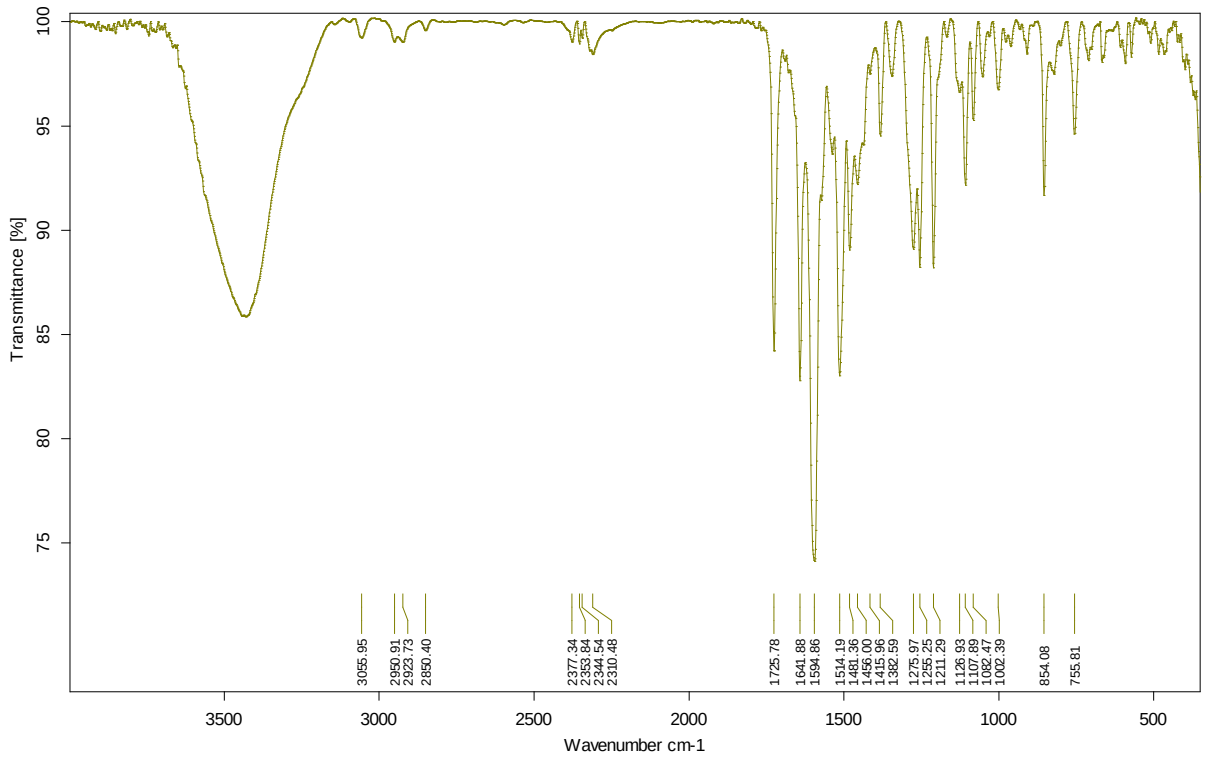

Figure S61. IR (KBr) spectrum of 6a

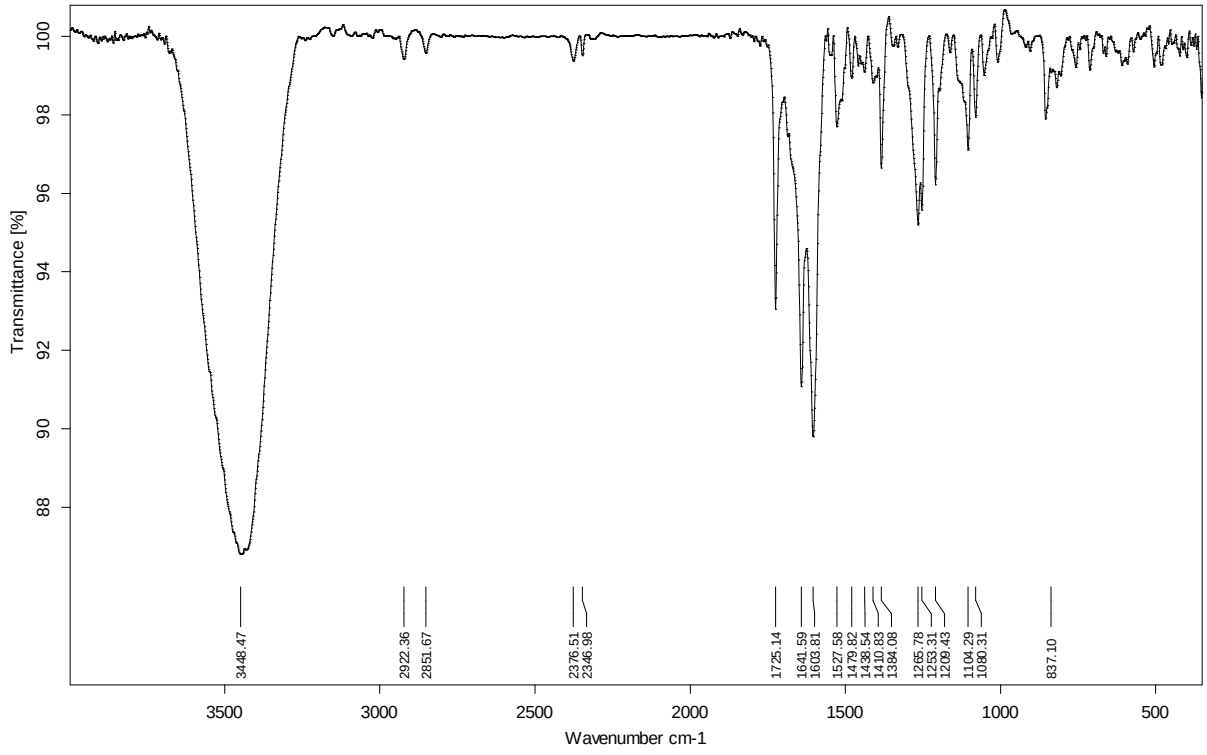

Figure S62. IR (KBr) spectrum of 6b

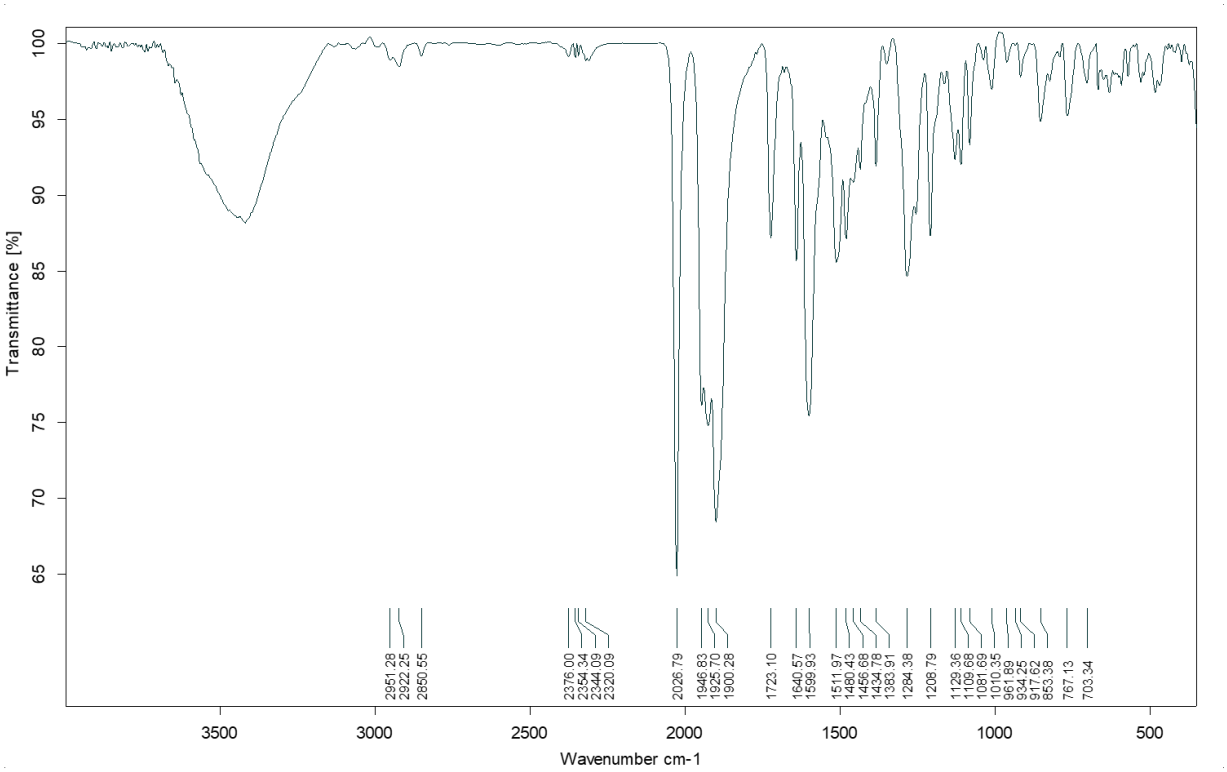

Figure S63. IR (KBr) spectrum 6a$_{Re}$

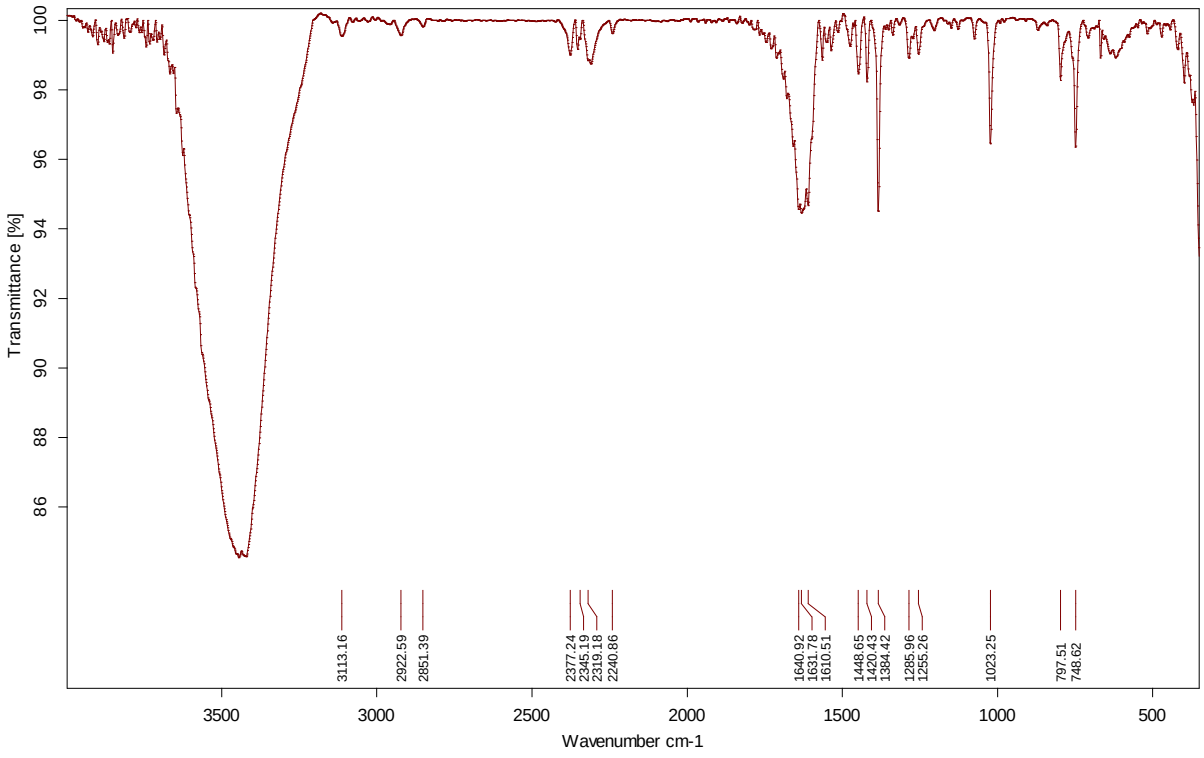

Figure S64. IR (KBr) spectrum of 9

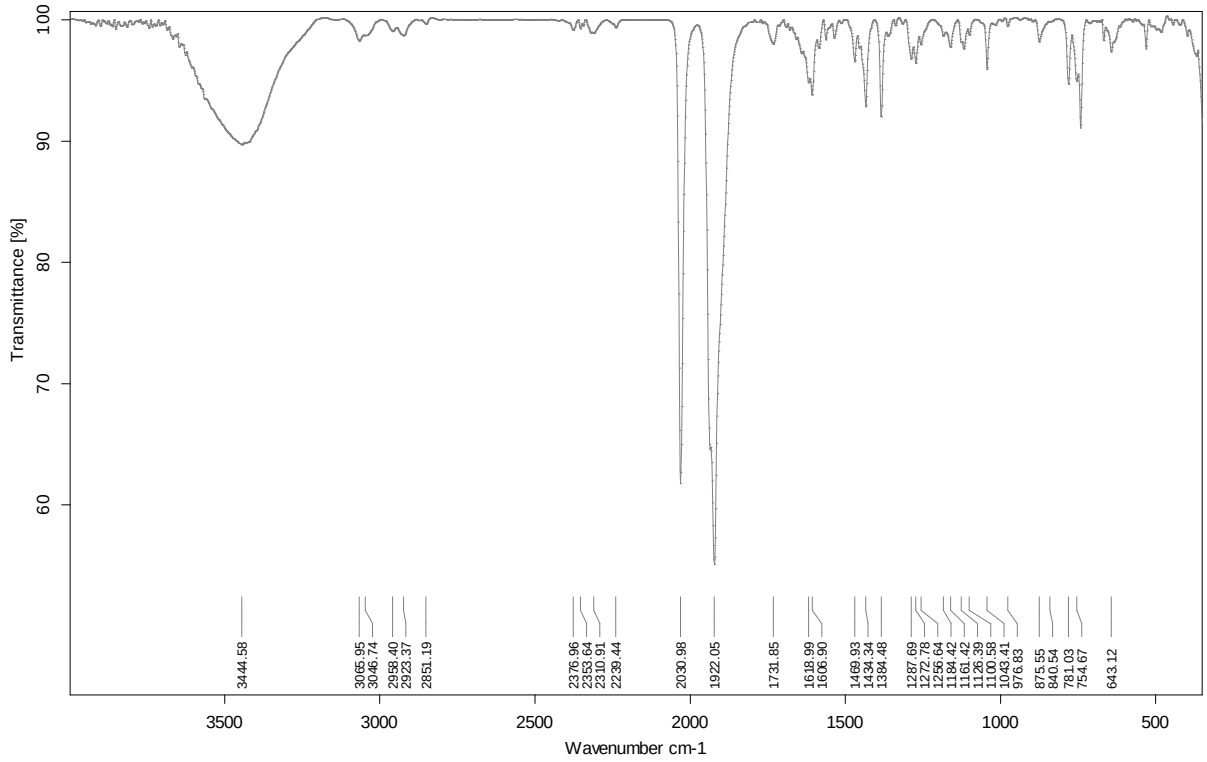

Figure S65. IR (KBr) spectrum 9_{Re}

6. UV-Vis spectra

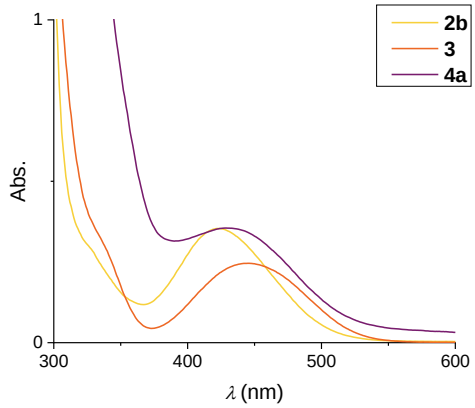

Figure S66. UV/Vis spectra of ligands 2b, 3 and 4a acetonitrile (*c* = 1.3 mmol, ACN)

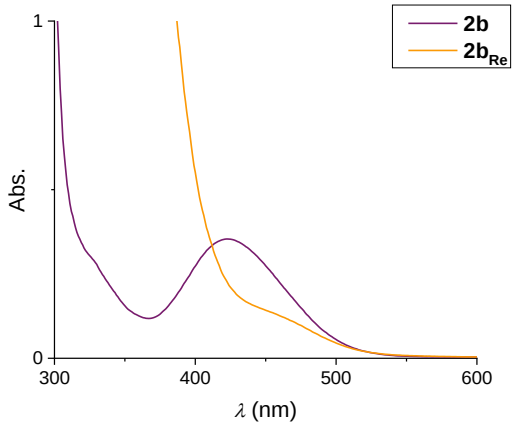

Figure S67. UV/Vis spectra of ligand 2b and complex 2b$_{Re}$ (*c* = 1.3 mmol, ACN)

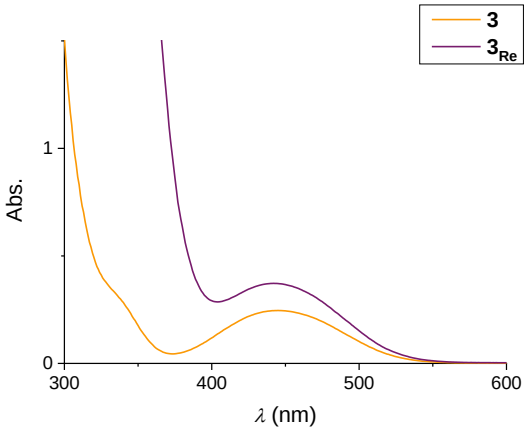

Figure S68. UV/Vis spectra of ligand 3 and complex 3$_{Re}$ (*c* = 1.3 mmol, ACN)

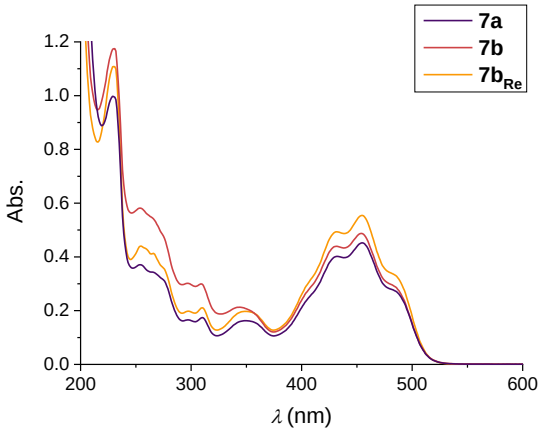

Figure S69. UV/Vis spectra of ligands 6a-6b and complex 6a$_{Re}$ (*c* = 2 × 10^{-5} mmol, ACN)

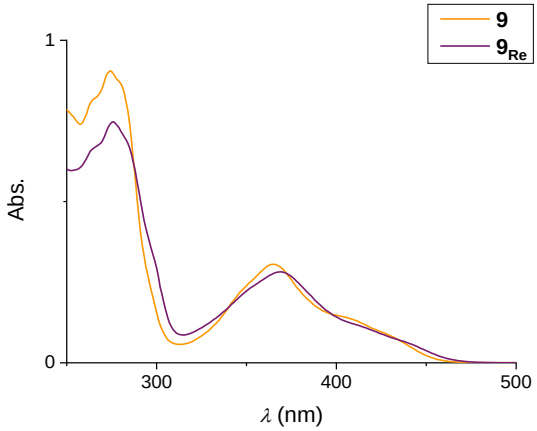

Figure S70. UV/Vis spectra of ligand 9 and complex 9$_{Re}$ (*c* = 1.3 mmol, ACN)

7. Synthesis of precursors

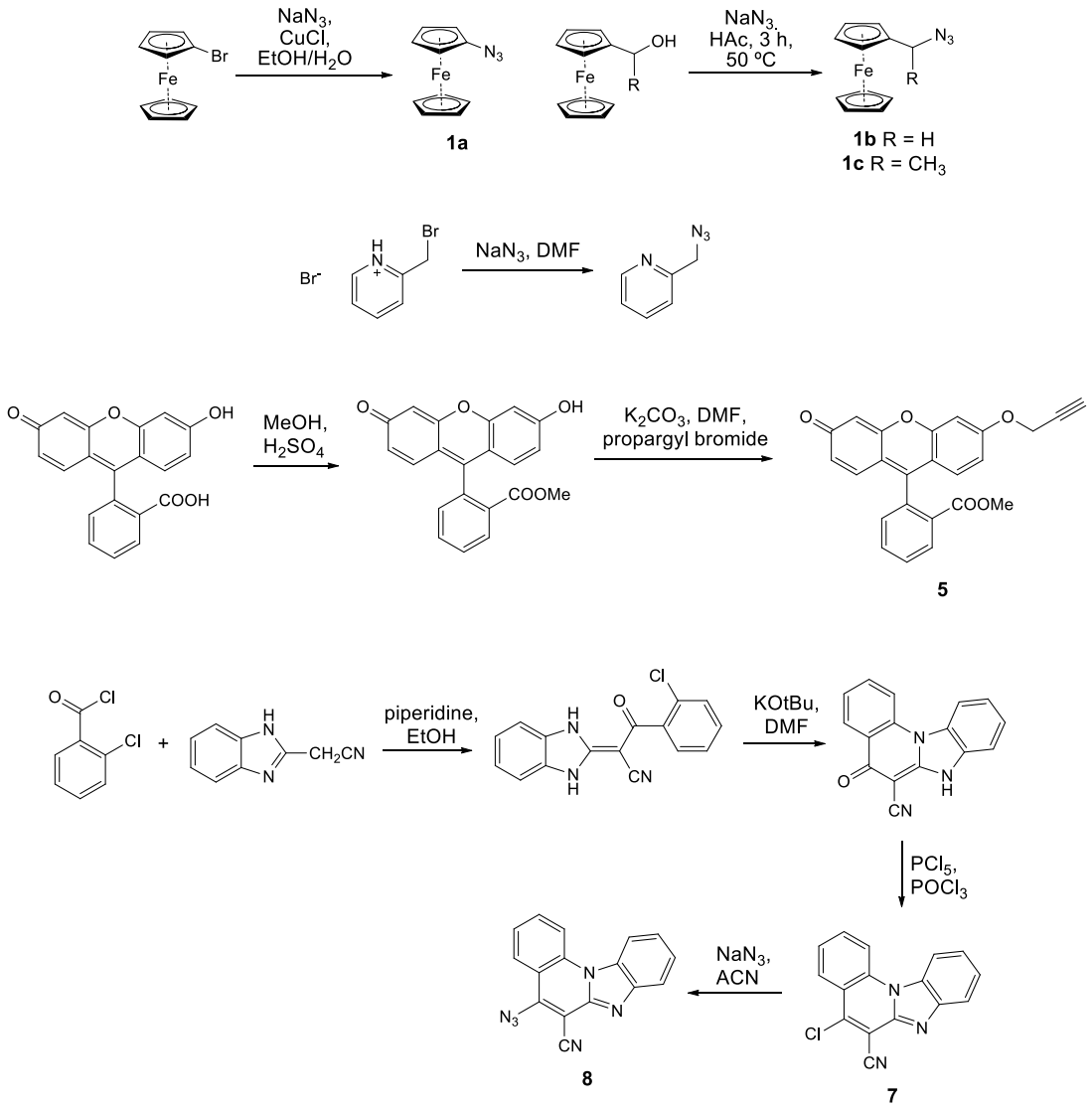

Scheme S1. Ferrocene azides (1a-c),[1] 2-picolyl azide,[2] propargyl derivative of fluorescein (5)[3] and benzimidazo[1,2-*a*]quinoline derivatives 7[4] and 8[5] were synthesised according to literature procedures

To prepare a fluorescent heterobimetallic complex, a xanthene fluorophore was introduced into the structure of ligand by conjugation of ferrocene and fluorescein by 1,2,3-triazole linker. The fluorescent product was isolated, but the coordination of the Re(I) metal centre probably did not result in formation of ML_2 complex (Scheme S2). Due to the low solubility of the product we were not successful in detailed characterisation.

Methyl 2-(6-((1-(ferrocenemethyl)-1,2,3-triazol-4-yl)methoxy)-3-oxoxanthen-9-yl)benzoate (6b). Compound **6b** was synthesised according to the general procedure for *click* reactions using 1-azidomethylferrocene (241 mg, 1.00 mmol, 1 equiv.), propargyl derivative **5** (386 mg, 1.00 mmol, 1 equiv.) and $Cu(OAc)_2 \cdot H_2O$ (9 mg, 0.05 mmol, 0.05 equiv.) in methanol (10 ml). Mobile phase for column chromatography was dichloromethane:methanol = 30:1. Yield: **6b** (0.32 mmol, 32%), red crystals (m. p. > 250 °C). ^{1}H NMR (300 MHz, DMSO) δ 8.27 (s, 1H, H5-triaz.), 8.21 (dd, *J* = 7.8, 1.0 Hz, 1H, Ar-H), 7.86 (td, *J* = 7.5, 1.3 Hz, 1H, Ar-H), 7.78 (td, *J* = 7.6, 1.3 Hz, 1H, Ar-H), 7.48 (dd, *J* = 7.5, 1.0 Hz, 1H, Ar-H), 7.38 (d, *J* = 2.4 Hz, 1H, Ar-H), 6.93 (dd, *J* = 8.9, 2.4 Hz, 1H, Ar-H), 6.81 (dd, *J* = 9.3, 6.8 Hz, 2H, Ar-H), 6.39 (dd, *J* = 9.7, 1.9 Hz, 1H, Ar-H), 6.24 (d, *J* = 1.9 Hz, 1H, Ar-H), 5.33 (s, 2H, CH_2), 5.31 (s, 2H, CH_2), 4.38 – 4.31 (m, 2H, Fc-H), 4.18 (s, 7H, Fc-H), 3.57 (s, 3H, OCH_3). ^{13}C NMR (151 MHz, DMSO) δ 183.83, 165.14, 162.43, 158.30, 153.38, 149.89, 141.66, 133.82, 133.16, 130.66, 130.33, 130.01, 129.46, 129.39, 128.79, 124.51, 116.72, 114.46, 114.02, 104.58, 101.35, 82.29, 68.60, 68.34, 61.87, 52.27, 48.96. IR (KBr)/cm^{-1}: 3448, 2922 (sp^3 C-H stretch), 2852 (sp^3 C-H stretch), 1725 (ester C = O stretch), 1642 (sp^2 C = N stretch), 1603 (sp^2 C = C Ar stretch), 1528 (sp^2 C = C Ar stretch), 1480, 1439, 1411, 1384, 1266 (C-O stretch), 1253 (C-O stretch), 1209, 1104, 1080, 837. SJ-218

Complex 6b$_{Re}$. Ligand **6b** (100 mg, 0.16 mmol, 1 equiv.), $Re(CO)_5Cl$ (58 mg, 0.16 mmol, 1 equiv.) and chloroform (20 ml) were used for the synthesis. Mobile phase for column chromatography was dichloromethane:methanol = 30:1. Yield: **6b$_{Re}$** (38 mg), red powder.

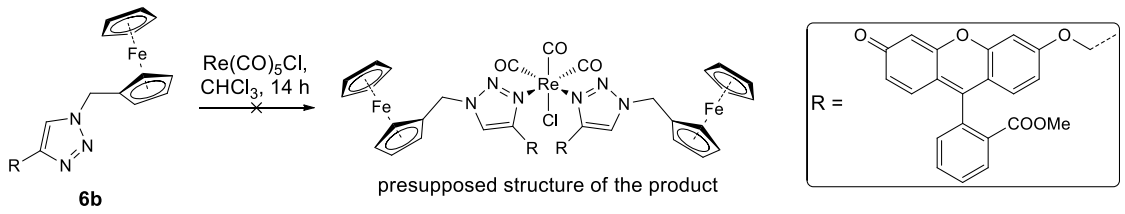

Scheme S2. Attempt of fluorescent heterobimetallic complex synthesis

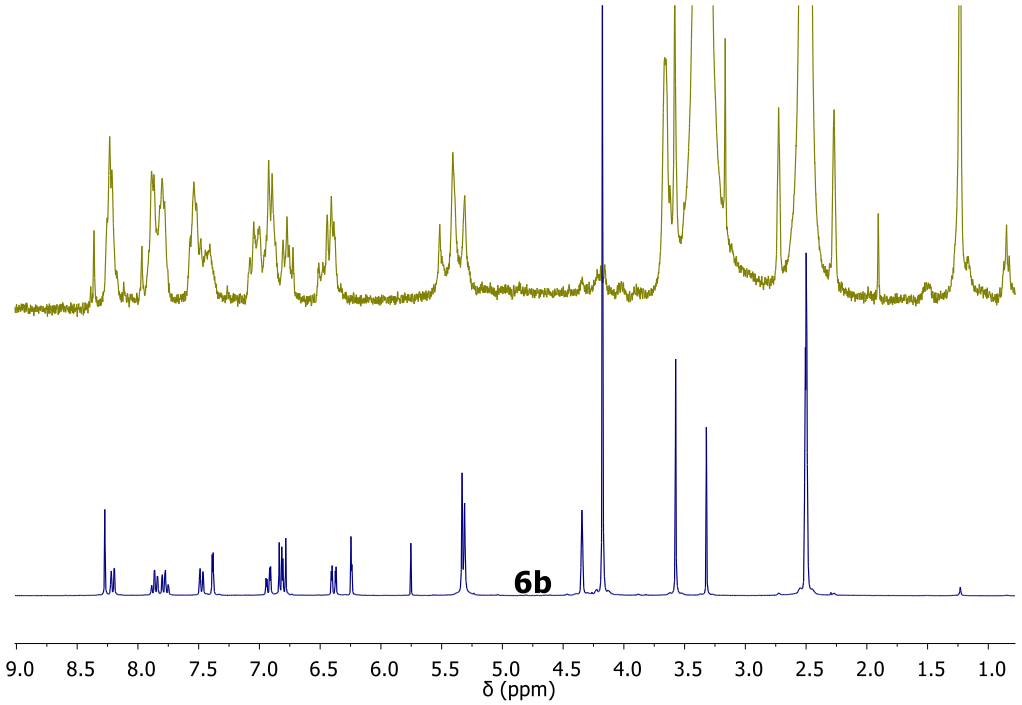

Figure S71. Comparison of the ^{1}H NMR spectra from ligand 6b (bottom) and product of the complexation reaction (top)

8. Interactions with biomolecules

Solubility

All compounds were dissolved in DMSO at 1 × 10^{-3} M. The stock solutions were kept at +4 °C and working aliquots were kept at +25 °C. No visible precipitation in working solutions was noticed.

8.1. Characterisation of $4a_{Re}$ and $4a_{Re}$·OTf and its interactions with biomolecules

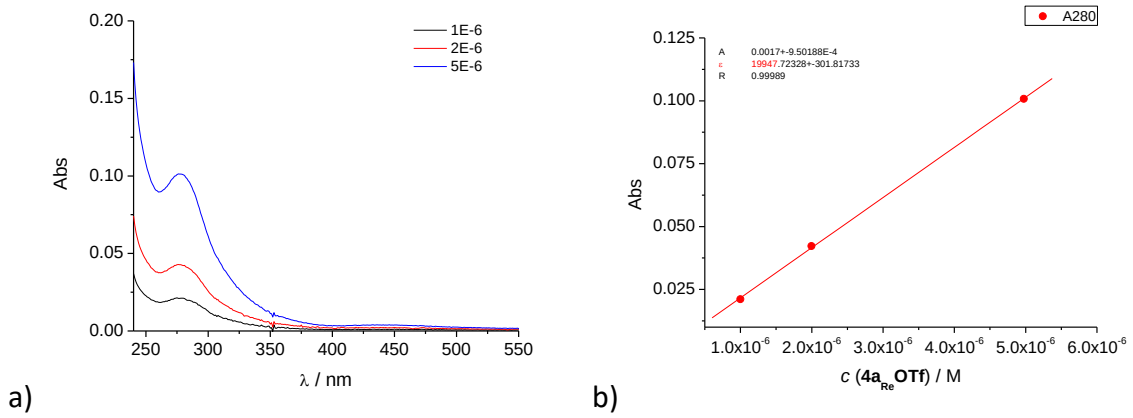

Figure S72. Absorption dependence of $4a_{Re}$·OTf on concentration. The sample shows one absorbance peak at 280 nm, b) calibration for $4a_{Re}$·OTf at 280 nm (ϵ = 19947 $M^{-1}cm^{-1}$).

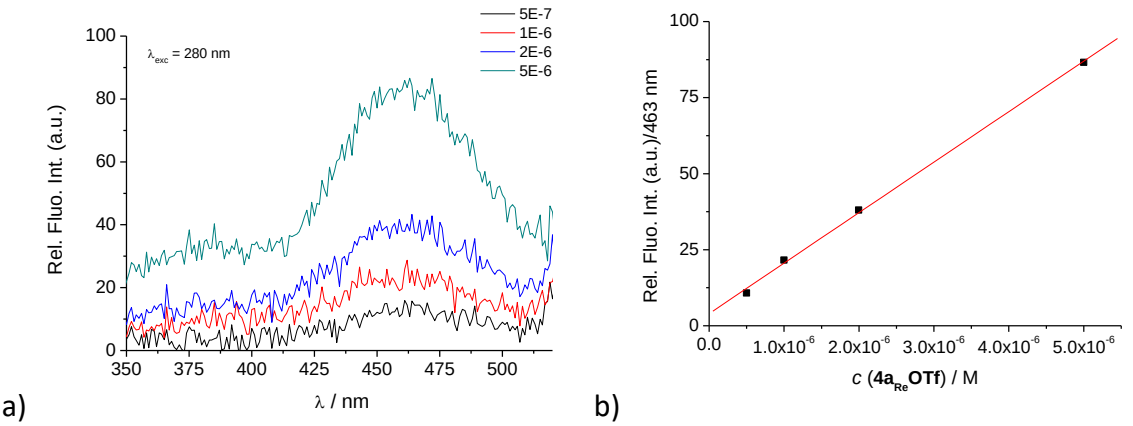

Figure S73. a) fluorescence intensity dependence of $4a_{Re}$·OTf on concentration. The sample shows a weak fluorescence peak at 463 nm, b) calibration for $4a_{Re}$·OTf at 463 nm.

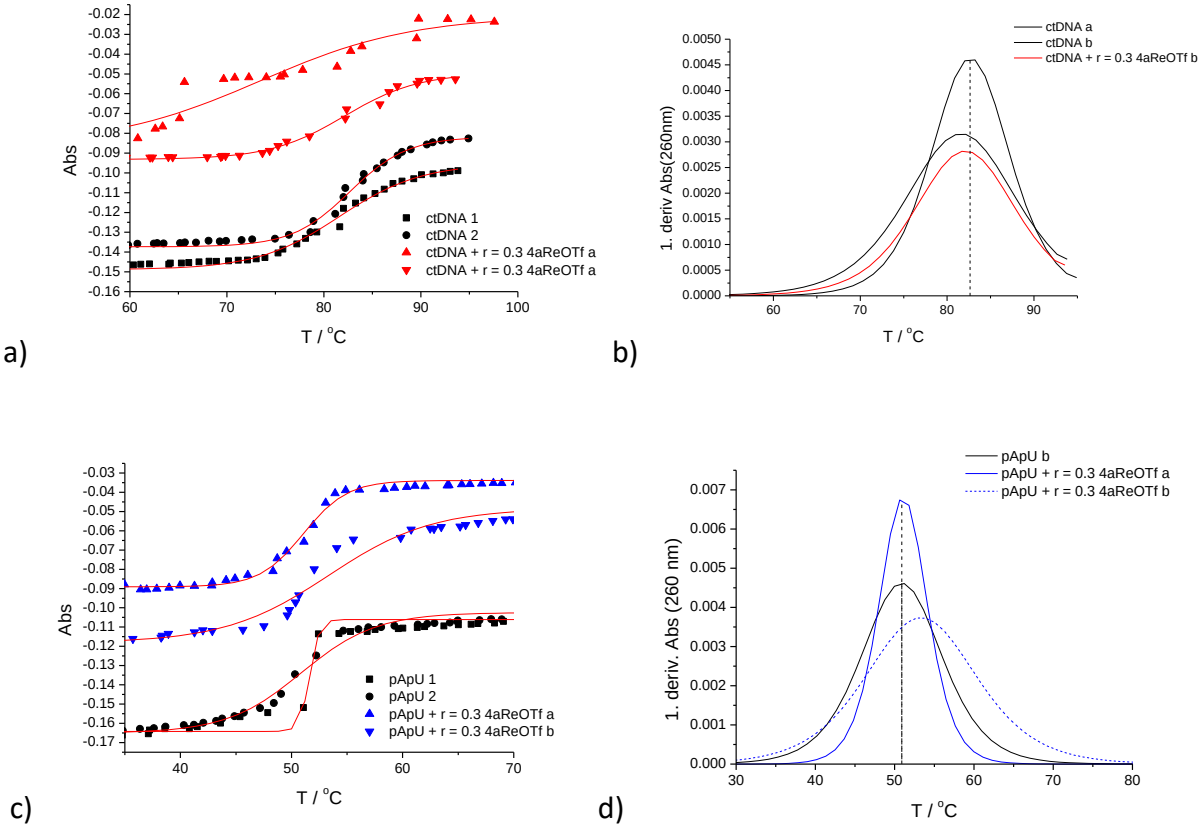

Figure S74. Melting curves of ctDNA upon addition *r* = 0.3 ([compound]/[polynucleotide]) of $4a_{Re}$·OTf at pH 7.0, (buffer sodium cacodylate, *I* = 0.05 M), red lines denote fitting of experimental data to sigmoidal eq. by Origin 7.5, b) the first derivation of absorbance (fitted to sigmoidal eq.) on temperature, c) melting curves of pApU upon addition *r* = 0.3 ([compound]/[polynucleotide]) of $4a_{Re}$·OTf at pH 7.0, (buffer sodium cacodylate, *I* = 0.05 M), red lines denote fitting of experimental data to sigmoidal eq. by Origin 7.5., d) the first derivation of absorbance (fitted to sigmoidal eq.) on temperature.

8.2. Characterisation of 6a and 6a$_{Re}$, 9 and 9$_{Re}$

8.2.1. UV/Vis and fluorescence spectra of 6a, 6a$_{Re}$, 9 and 9$_{Re}$

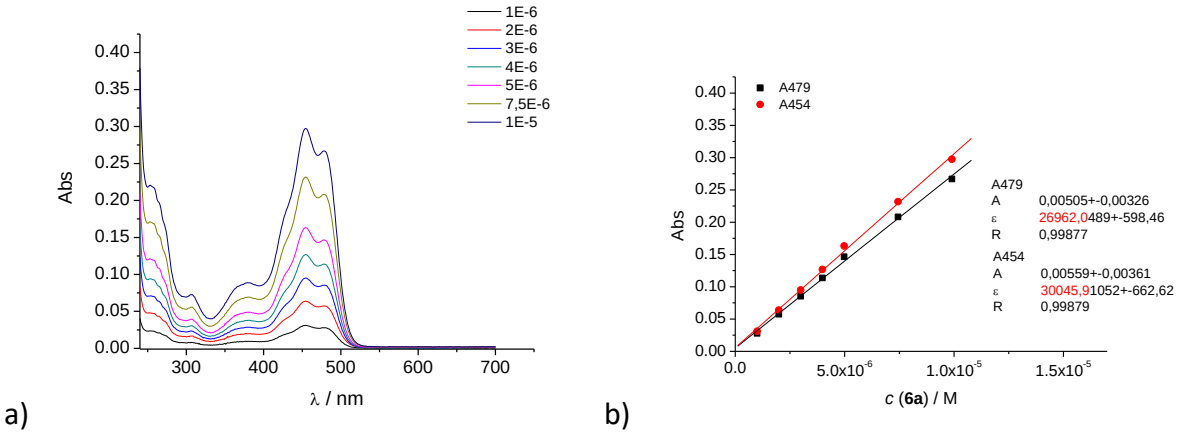

Figure S75. Absorption dependence of 6a on concentration. The sample shows two absorbance peaks, at 479 nm and at 454 nm, b) calibration for 6a at 479 (black) and 454 (red) nm. Molar extinction coefficient (ε) is 26962 M^{-1} cm^{-1} at 479 nm and 30046 at 454 nm.

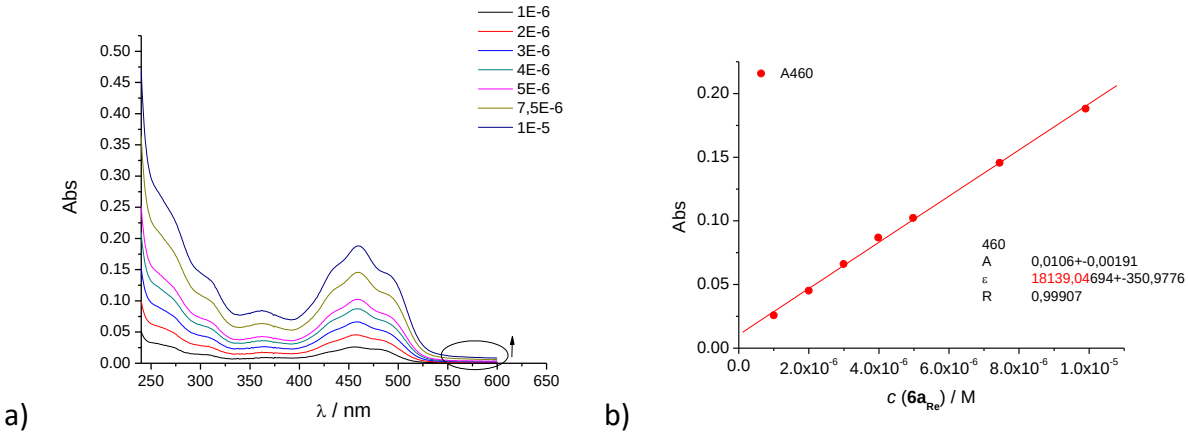

Figure S76. Absorption dependence of 6a$_{Re}$ on concentration. The sample shows an absorbance peak at 460 nm, b) calibration for 6a$_{Re}$ at 460 nm. Molar extinction coefficient (ε) is 18139 M^{-1} cm^{-1} at 460 nm.

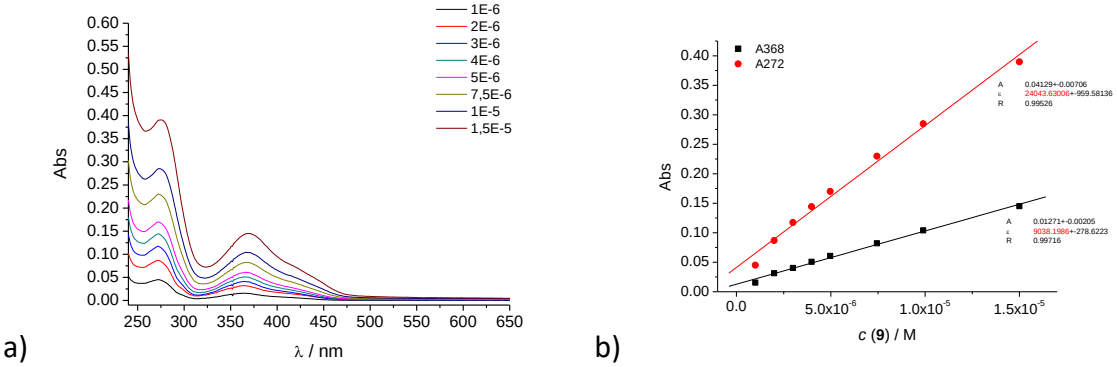

Figure S77. Absorption dependence of 9 on concentration, b) calibration for 9 at 272 and 368 nm. Molar extinction coefficient (ε) is 24043.6 M^{-1} cm^{-1} at 272 nm and 9038 at 368 nm.

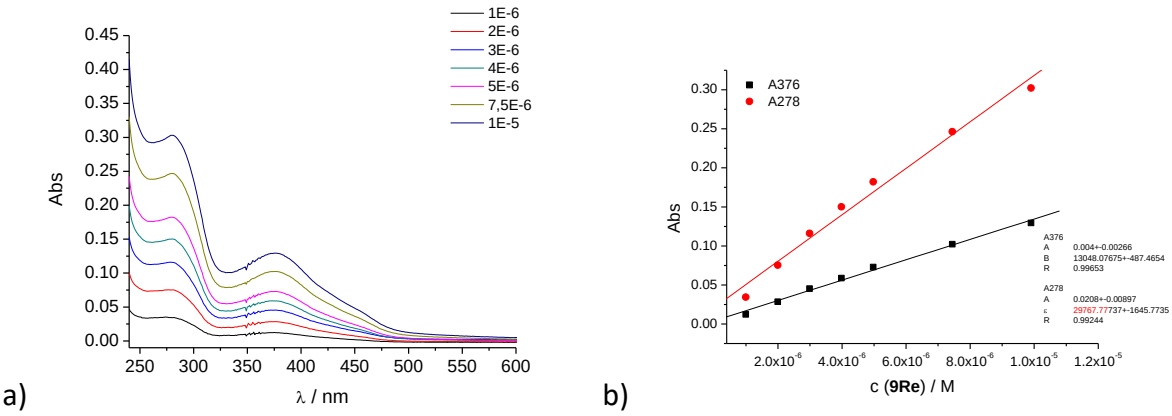

Figure S78. Absorption dependence of 9_{Re} on concentration. The sample shows two absorbance peaks, at 376 nm and at 278 nm, b) calibration for 9_{Re} at 278 and 376 nm. Molar extinction coefficient (ε) is 29767.8 M^{-1} cm^{-1} at 278 nm and 13048.1 at 376 nm.

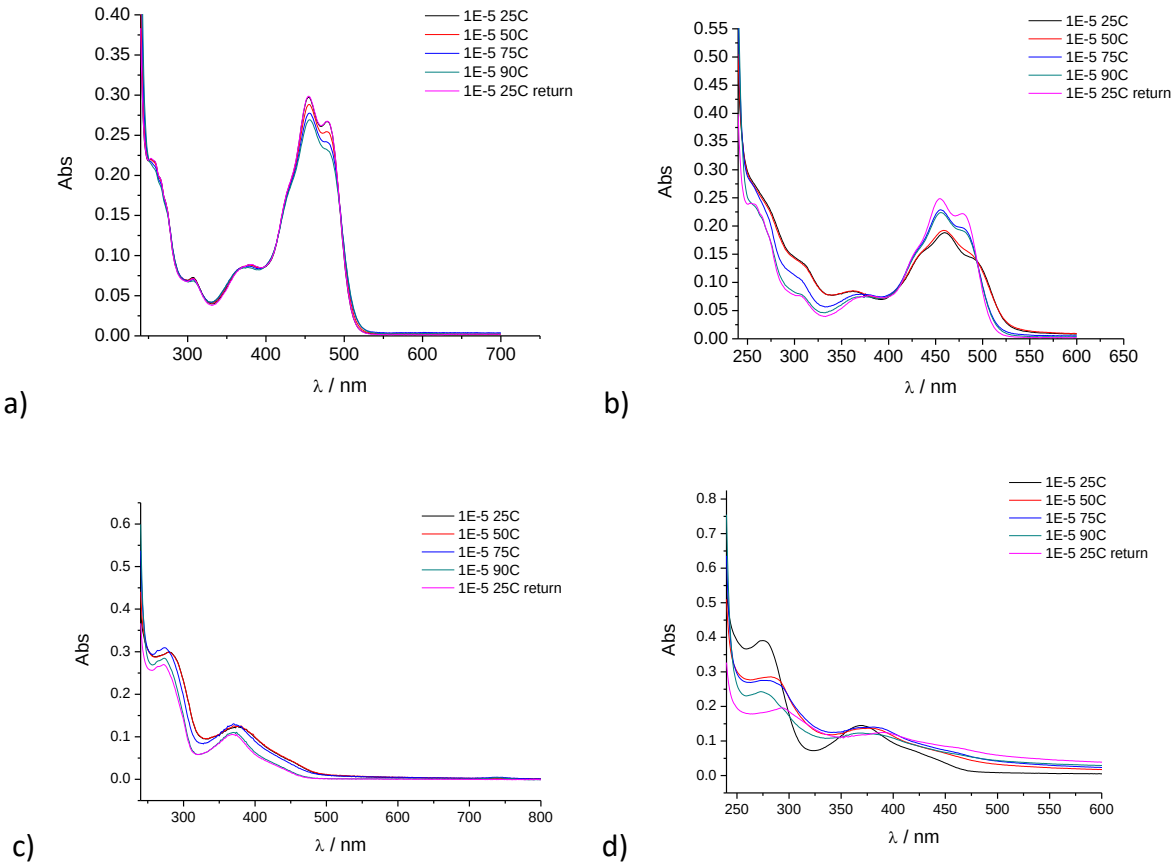

Figure S79. a) temperature stability of 6a at c = 1×10^{-5} M, b) temperature stability of 6a$_{Re}$ at c = 1×10^{-5} M, c) temperature stability of 9 at c = 1 × 10^{-5} M, d) temperature stability of 9$_{Re}$ at c = 1 × 10^{-5} M.

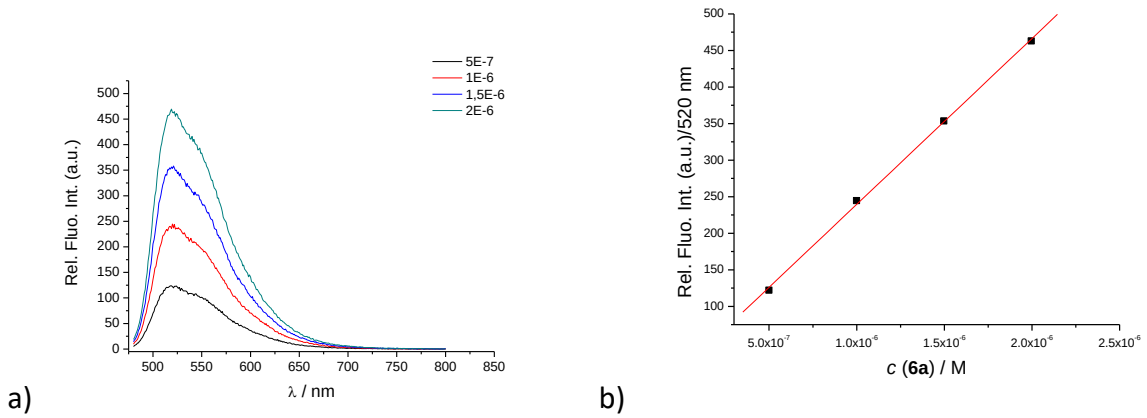

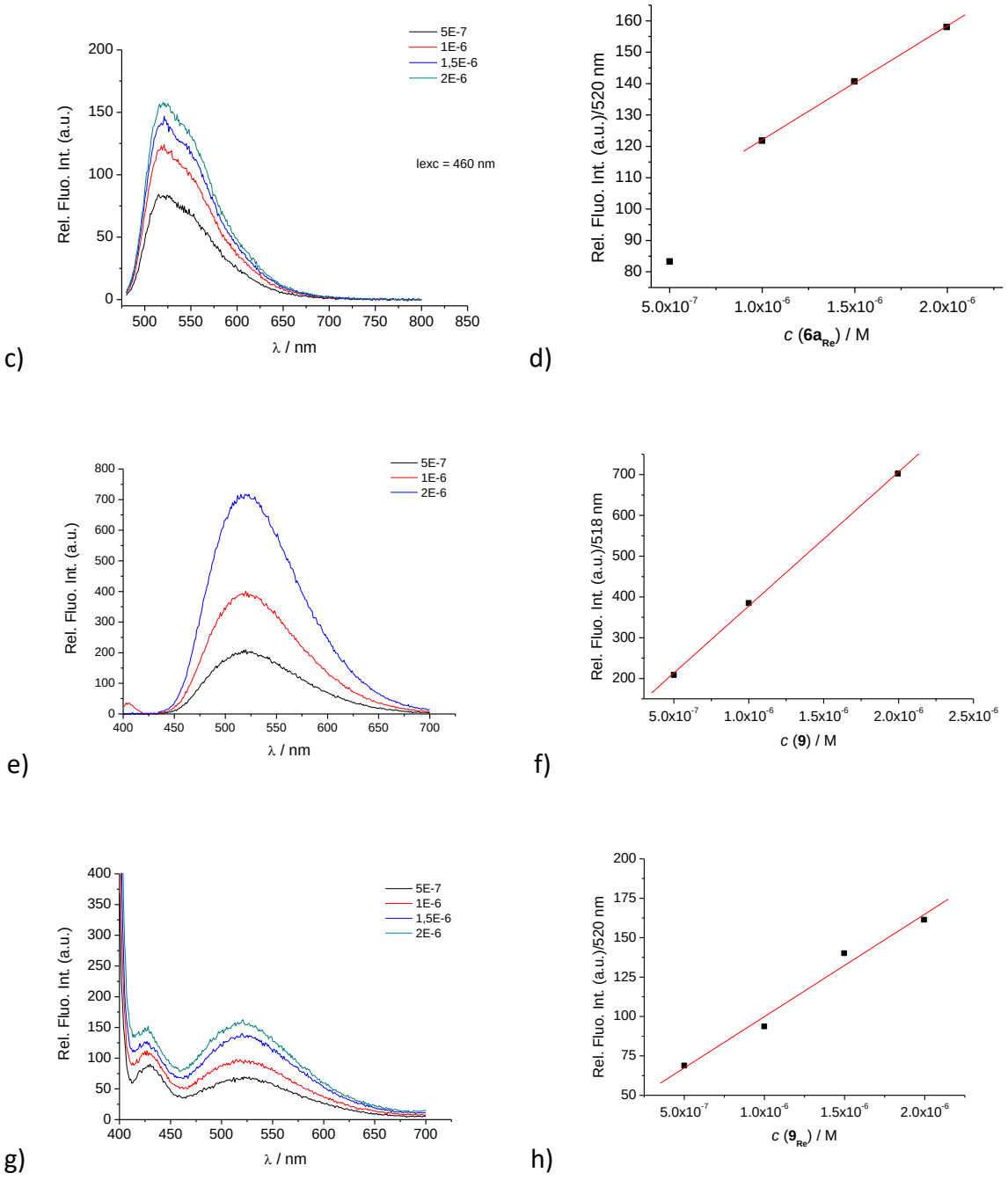

Figure S80. a) dependence of fluorescence spectra on concentration of 6 (λ_{exc} = 460 nm, slits 5 nm-5 nm), b) dependence of fluorescence spectra on concentration increase of 6 at λmax = 520 nm, c) dependence of fluorescence spectra on concentration of 6a$_{Re}$ (λ_{exc} = 460 nm, slits 5 nm-5 nm), d) dependence of fluorescence spectra on concentration increase of 6a$_{Re}$ at λmax = 520 nm, e) Dependence of fluorescence spectra on concentration of 9 (λ_{exc} = 368 nm, slits 10 nm-10 nm), f) dependence of fluorescence spectra on concentration increase of 9 at λmax = 518 nm, g) Dependence of fluorescence spectra on concentration of 9$_{Re}$ (λ_{exc} = 372 nm, slits 20 nm-20 nm), h) dependence of fluorescence spectra on concentration increase of 9$_{Re}$ at λmax = 520 nm.

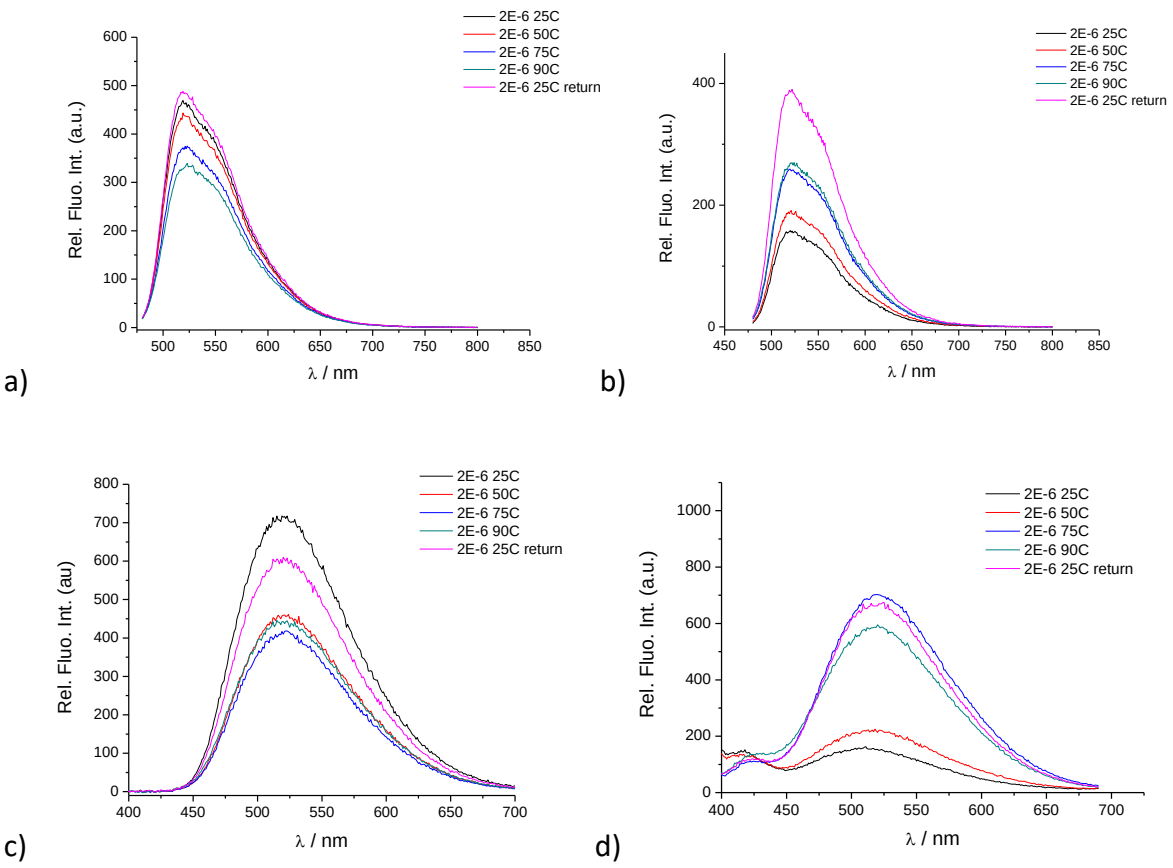

Figure S81. a) dependence of fluorescence intensity on temperature increase for 6a at 2 × 10^{-6} M, b) dependence of fluorescence intensity on temperature increase for $6a_{Re}$ at 2 × 10^{-6} M, c) dependence of fluorescence intensity on temperature increase for 9 at 2 × 10^{-6} M, d) dependence of fluorescence intensity on temperature increase for 9_{Re} at 2 × 10^{-6} M.

8.2.2. Study of interactions of 6a and $6a_{Re}$, 9 and 9_{Re} with ds DNA/RNA and proteins in aqueous media

8.2.2.1. Fluorimetric titrations of 6a

General conditions: slits 5-10, excitation at 460 nm, emission at 520 nm

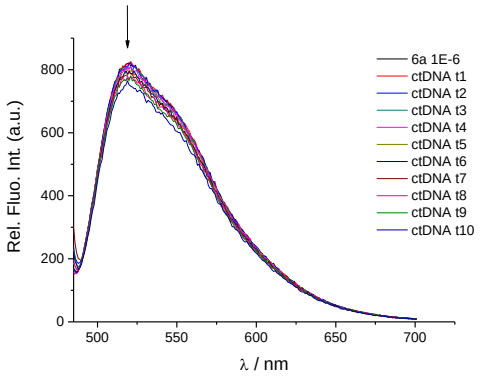

Figure S82. Changes in fluorescence spectrum of 6a (c = 1 × 10^{-6} M) upon titration with ctDNA at pH 7.0, sodium cacodylate buffer, I = 0.05, too small changes of intensity at λ_{max} = 520 nm on c(ctDNA) for processing.

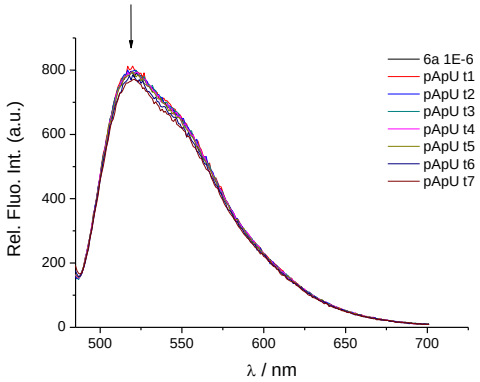

Figure S83. Changes in fluorescence spectrum of 6a (λ_{exc} = 460 nm, c = 1 × 10^{-6} M) upon titration with pApU at pH 7.0, sodium cacodylate buffer, I = 0.05, too small changes of intensity at λ_{max} = 520 nm on c(pApU) for processing.

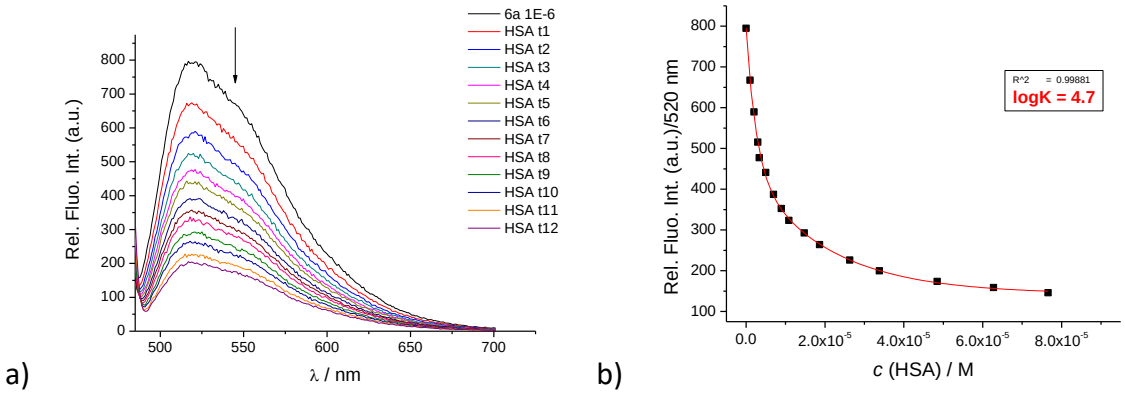

Figure S84. a) Changes in fluorescence spectrum of 6a (c = 1 × 10^{-6} M) upon titration with HSA at pH 7.0, sodium cacodylate buffer, I = 0.05, b) dependence of 6a intensity at λ_{max} = 520 nm on c(HSA), at pH 7.0, sodium cacodylate buffer, I = 0.05 M, fit to stoichiometry dye:HSA = 1:1

8.2.2.2. Fluorimetric titrations of 6a$_{Re}$

General conditions: slits 5-10 for all experiments, excitation at 460 nm, emission at 520 nm

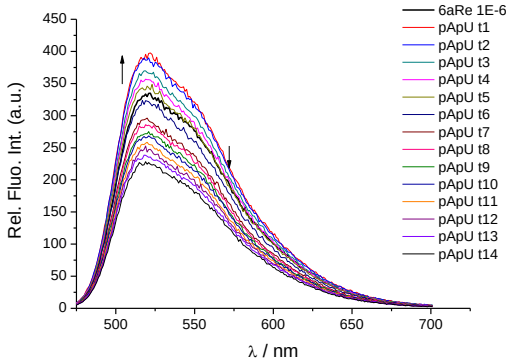

Figure S85. Changes in fluorescence spectrum of 6a$_{Re}$ (c = 1 × 10^{-6} M) upon titration with pApU at pH 7.0, sodium cacodylate buffer, I = 0.05 M.

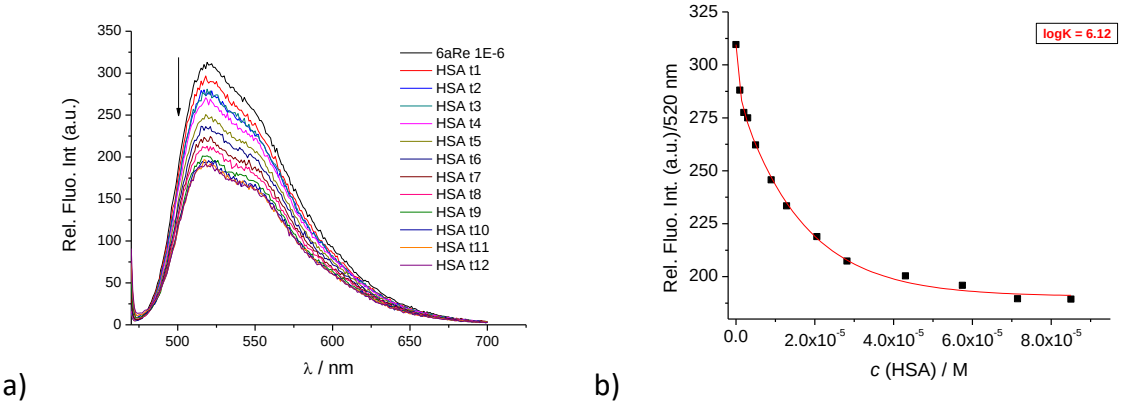

a) b)

Figure S86. Changes in fluorescence spectrum of 6a$_{Re}$ (c = 1 × 10^{-6} M) upon titration with HSA at pH 7.0, sodium cacodylate buffer, I = 0.05, b) dependence of 6a$_{Re}$ intensity at λ_{max} = 520 nm on c(HSA), at pH 7.0, sodium cacodylate buffer, I = 0.05 M, fit to fit to stoichiometry dye:HSA = 1:1.

8.2.2.3. Fluorimetric titrations of 9

General conditions: slits 10-20, excitation at 368 nm, emission at 518 nm

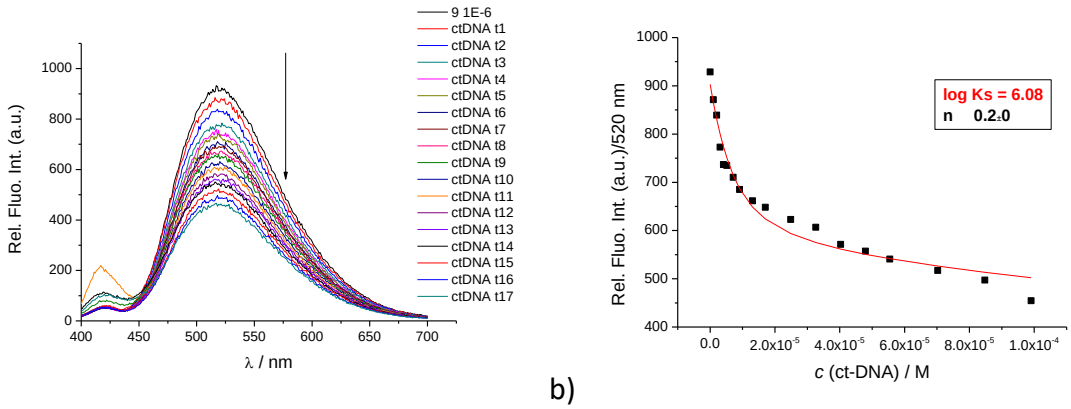

a) b)

Figure S87. Changes in fluorescence spectrum of 9 (c = 1 × 10^{-6} M) upon titration with ctDNA at pH 7.0, sodium cacodylate buffer, I = 0.05, b) dependence of 9 intensity at λ_{max} = 518 nm on c(ctDNA), at pH 7.0, sodium cacodylate buffer, I = 0.05 M, fit to Scatchard eq.

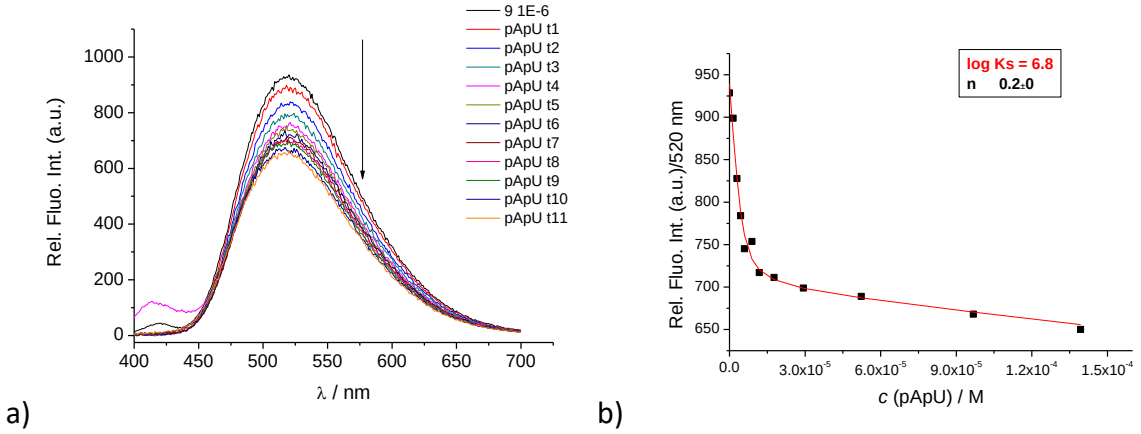

Figure S88. Changes in fluorescence spectrum of 9 (λ_{exc} = 368 nm, c = 1 × 10^{-6} M) upon titration with pApU at pH 7.0, sodium cacodylate buffer, I = 0.05, b) dependence of AM406 intensity at λ_{max} = 518 nm on c(pApU), at pH 7.0, sodium cacodylate buffer, I = 0.05 M, fit to Scatchard eq.

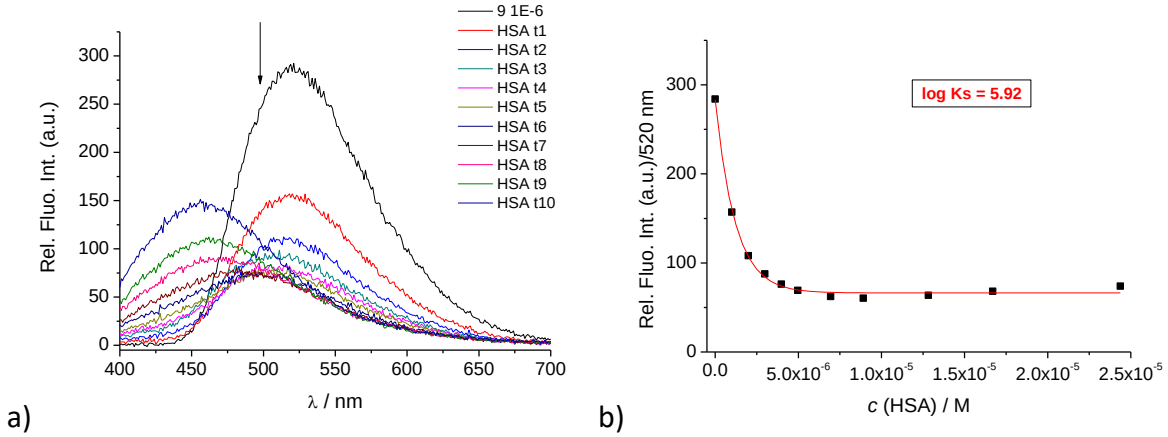

Figure S89. Changes in fluorescence spectrum of 9 (c = 1 × 10^{-6} M) upon titration with HSA at pH 7.0, sodium cacodylate buffer, I = 0.05, b) dependence of 9 intensity at λ_{max} = 520 nm on c(HSA), fit to stoichiometry dye:HSA = 1:1.

8.2.2.4. Fluorimetric titrations of 9_{Re}

General conditions: slits 20 nm-20 nm for all experiments except HSA titration (slits 10 nm – 20 nm), excitation at 376 nm

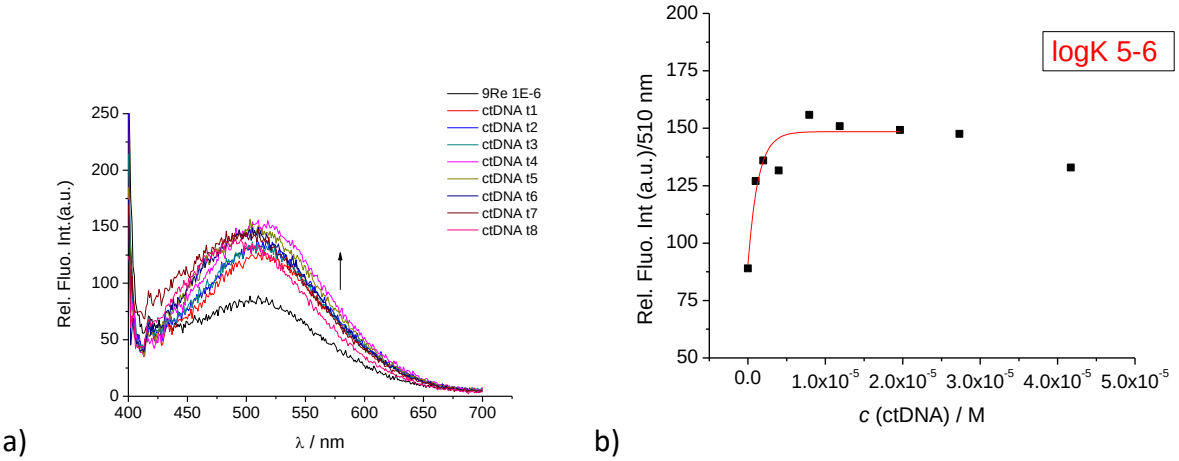

Figure S90. Changes in fluorescence spectrum of 9_{Re} (c = 1 × 10^{-6} M, λ_{exc} = 376 nm, λ_{em} = 510 nm) upon titration with ctDNA at pH 7.0, sodium cacodylate buffer, I = 0.05, b) small changes of intensity at λ_{max} = 510 nm on c(ctDNA), allowed only estimation of log K.

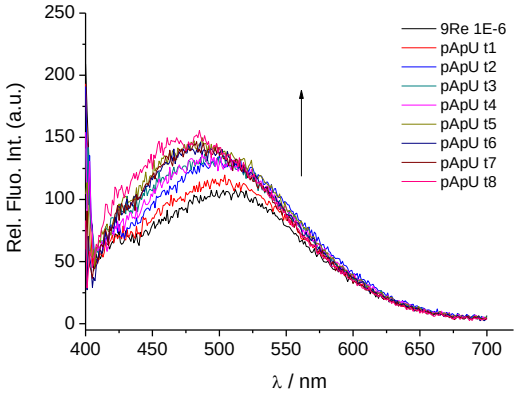

Figure S91. Changes in fluorescence spectrum of 9_{Re} (c = 1 × 10^{-6} M) upon titration with pApU at pH 7.0, sodium cacodylate buffer, I = 0.05, b) dependence of 9_{Re} intensity at λ_{max} = 510 nm on c(pApU), at pH 7.0, sodium cacodylate buffer, I = 0.05 M. Too small changes of intensity at λ_{max} = 520 nm on c(pApU) for processing.

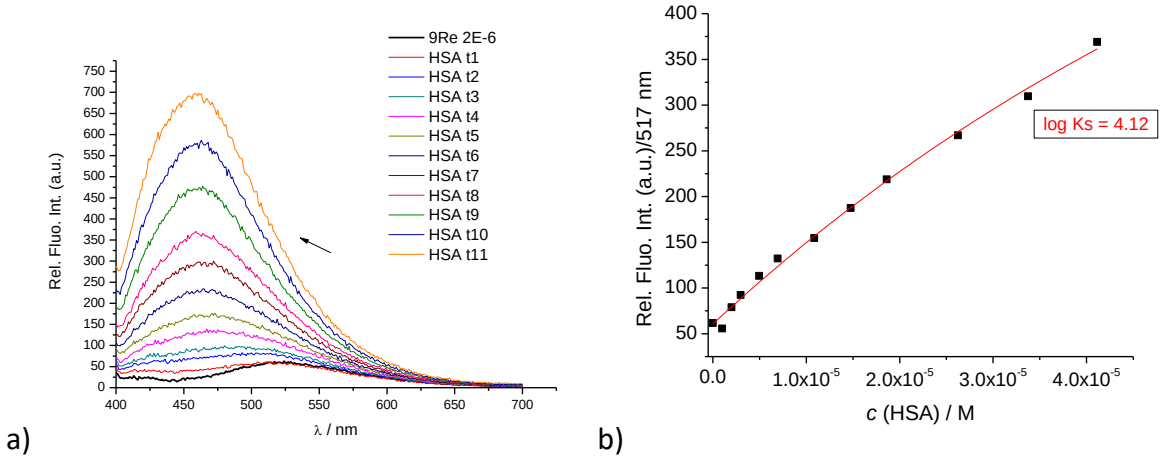

Figure S92. Changes in fluorescence spectrum of 9_{Re} (c = 2 × 10^{-6} M) upon titration with HSA at pH 7.0, sodium cacodylate buffer, I = 0.05, done at slits 10-20, b) dependence of 9_{Re} intensity at λ_{max} = 517 nm on c(HSA), fit to stoichiometry dye:HSA = 1:1.

8.2.2.5 Circular dichorism experiments

Instrument (JASCO J-815 CD Spectrometer): 25 ˚C, pH = 7, buffer Na cacodylate, I = 0.05 M; t_{incub} = 0 min; **parameters:** range = 550-240 nm**,** sensitivity = high (5 mdeg)**,** data pitch = 0.2 nm**,** scanning speed = 200 nm/min, accumulation = 3

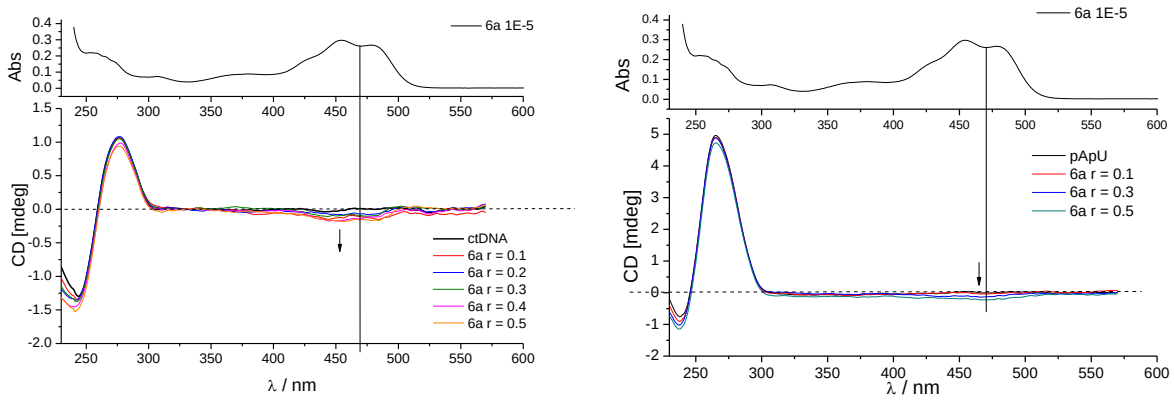

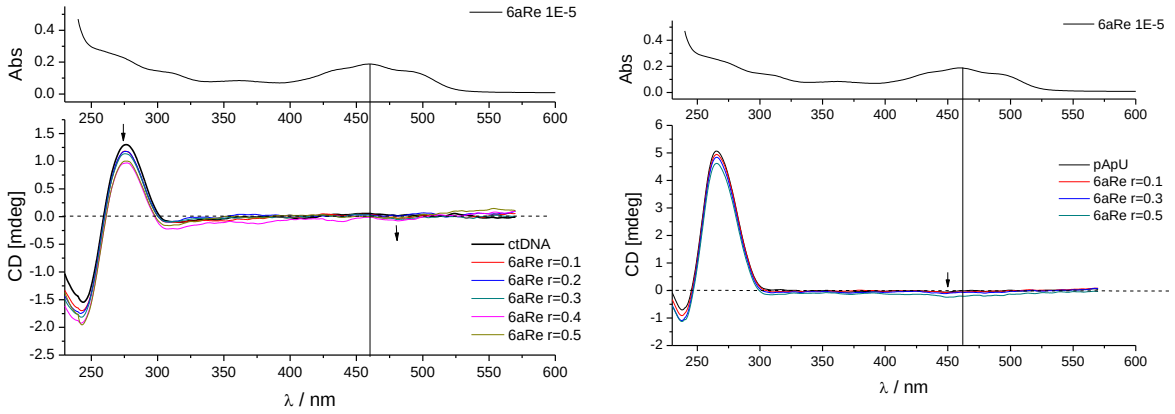

c) d)

Figure S93. CD titration of polynucleotides (c = 2 × 10^{-5} M) with 6a and $6a_{Re}$ at molar ratios r = [compound]/[polynucleotide] (pH 7.0, buffer sodium cacodylate, I = 0.05 M): a) ctDNA with 6a, b) pApU with 6a, c) ctDNA with $6a_{Re}$, d) pApU with $6a_{Re}$

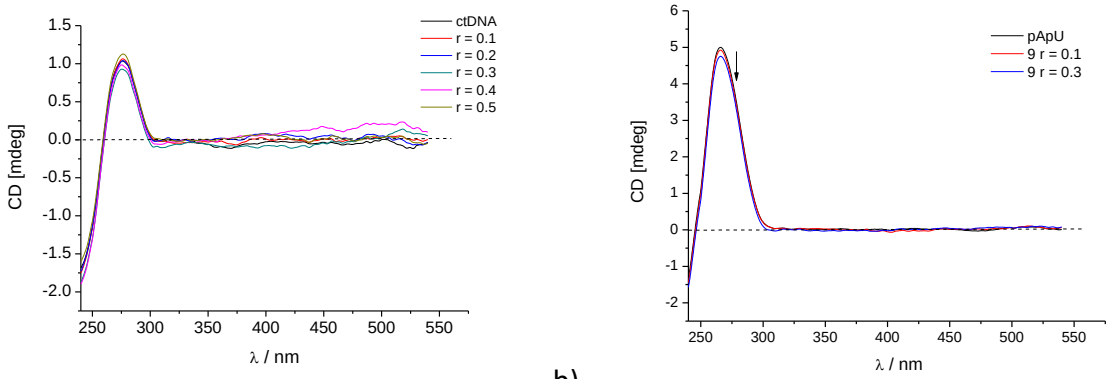

a) b)

Figure S94. CD titration of polynucletiodes (c = 2 × 10^{-5} M) with 9 at molar ratios r = [compound] / [polynucleotide] (pH 7.0, buffer sodium cacodylate, I = 0.05 M). a) ctDNA with 9, b) pApU with 9.

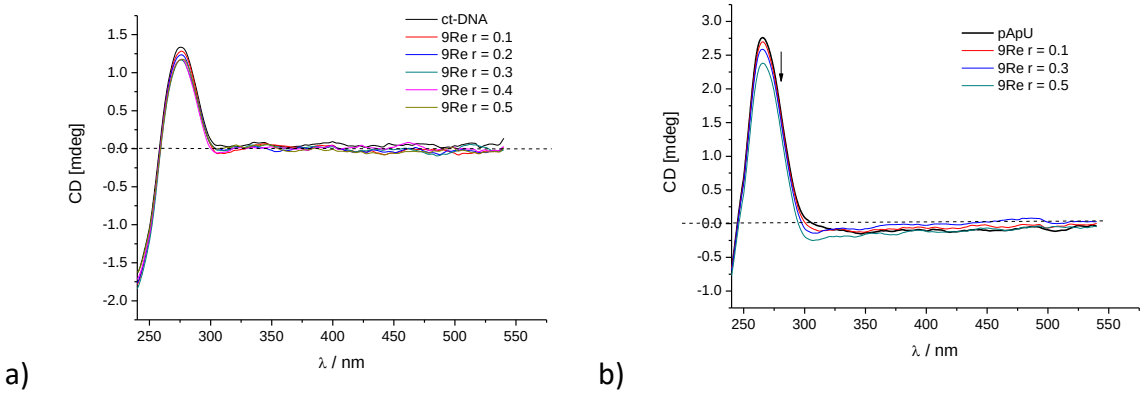

a) b)

Figure S95. CD titration of polynucletiodes (c = 2 × 10^{-5} M) with 9_{Re} at molar ratios r = [compound] / [polynucleotide] (pH 7.0, buffer sodium cacodylate, I = 0.05 M). a) ctDNA with 9_{Re}, b) pApU with 9_{Re}.

8.2.2.6. Thermal melting experiments

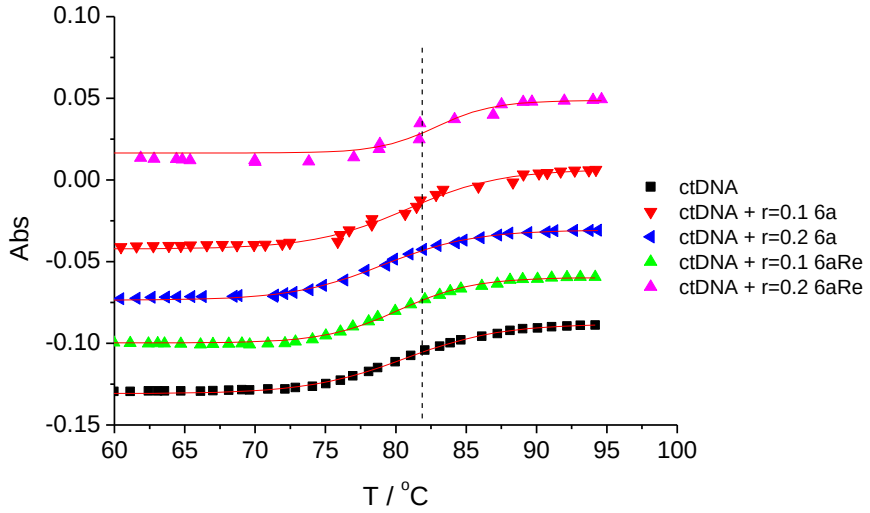

Figure S96. Melting curves of ct-DNA upon addition r = 0.1 or r = 0.2 ([compound]/[polynucleotide]) of 6a and $6a_{Re}$ at pH 7.0, (buffer sodium cacodylate, I = 0.05 M), red lines denote fitting of experimental data to sigmoidal eq. by Origin 7.5.

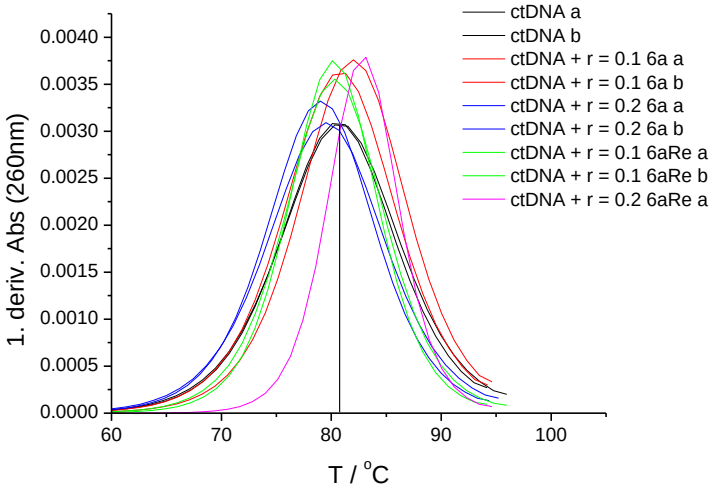

Figure S97. The first derivation of absorbance (fitted to sigmoidal eq.) on temperature for melting curves of ct-DNA upon addition r = 0.1 or r = 0.2 ([compound]/[polynucleotide]) of 6a and $6a_{Re}$ at pH 7.0, (buffer sodium cacodylate, I = 0.05 M).

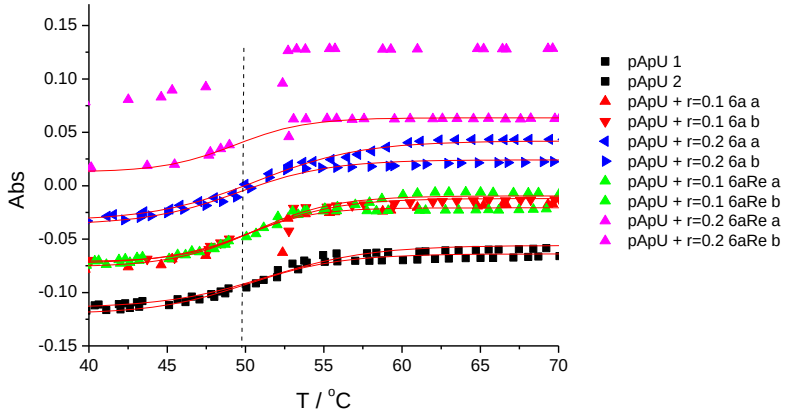

a)

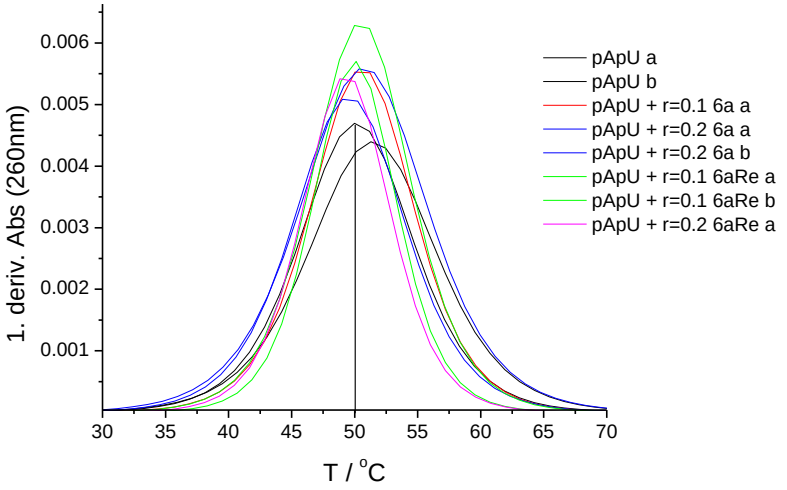

b)

Figure S98. a) melting curves of pApU upon addition r = 0.1 or r = 0.2 ([compound]/[polynucleotide]) of 6a and $6a_{Re}$ at pH 7.0, (buffer sodium cacodylate, I = 0.05 M), red lines denote fitting of experimental data to sigmoidal eq. by Origin 7.5., b) the first derivation of absorbance (fitted to sigmoidal eq.) on temperature.

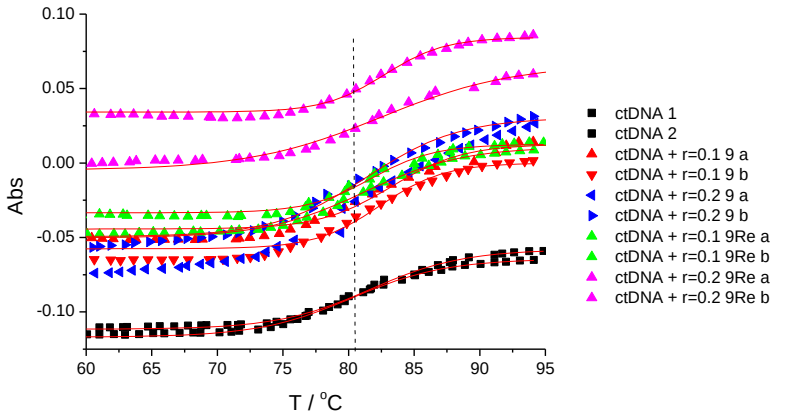

a)

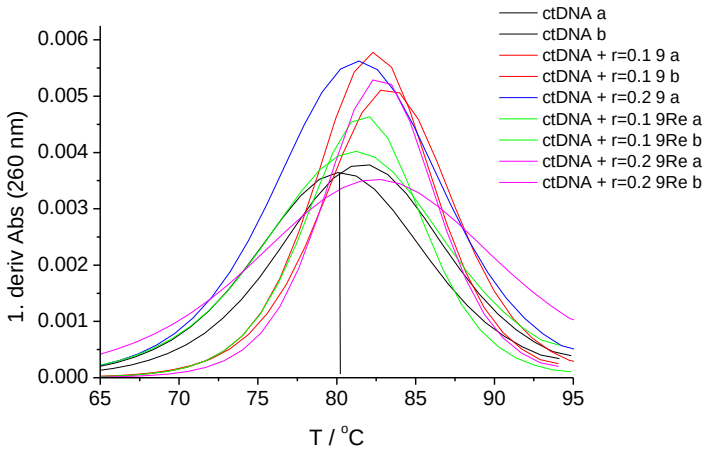

b)

Figure S99. Melting curves of ct-DNA upon addition r = 0.1 or r = 0.2 ([compound]/[polynucleotide]) of 9 and 9_{Re} at pH 7.0, (buffer sodium cacodylate, I = 0.05 M), red lines denote fitting of experimental data to sigmoidal eq. by Origin 7.5., b) the first derivation of absorbance (fitted to sigmoidal eq.) on temperature.

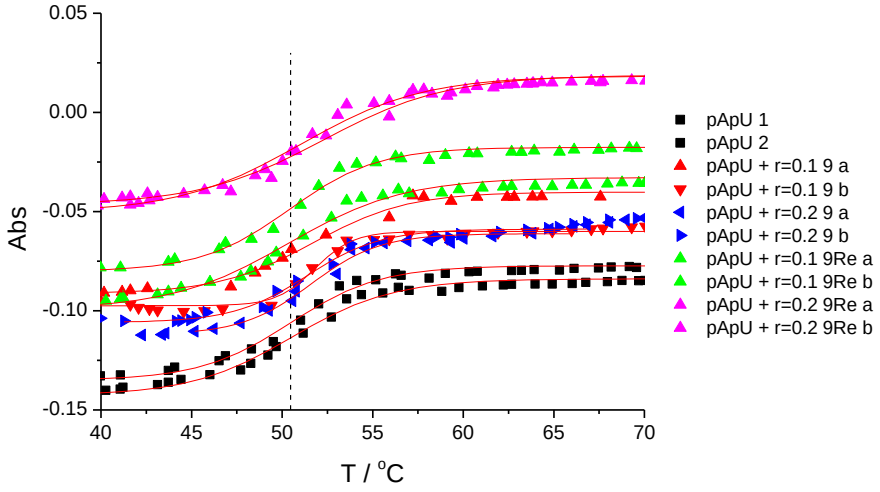

a)

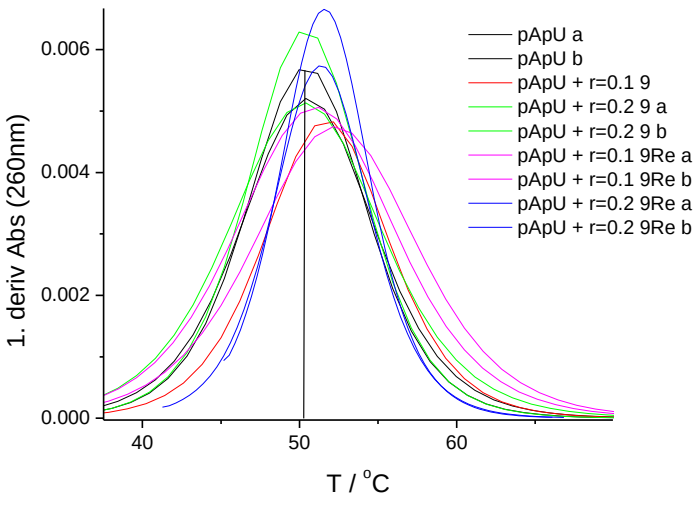

b)

Figure S100. Melting curves of pApU upon addition *r* = 0.1 or *r* = 0.2 ([compound]/[polynucleotide]) of 9 and 9_{Re} at pH 7.0, (buffer sodium cacodylate, *I* = 0.05 M), red lines denote fitting of experimental data to sigmoidal eq. by Origin 7.5., b) the first derivation of absorbance (fitted to sigmoidal eq.) on temperature.

9. Cytotoxicity studies

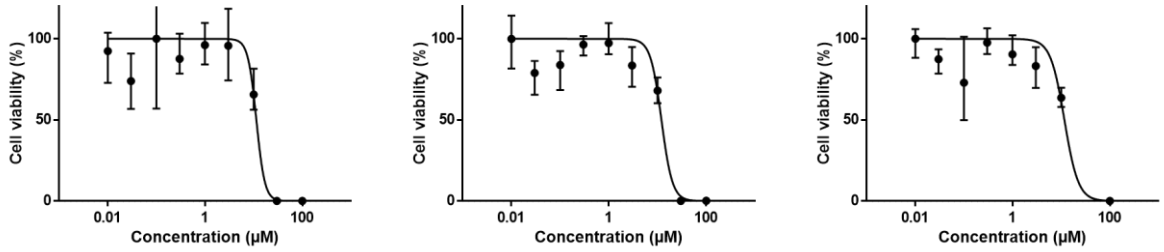

Figure S101: Fluorometric cell viability assay of $2a_{Re}$ in CT26 cells after 48h incubation.

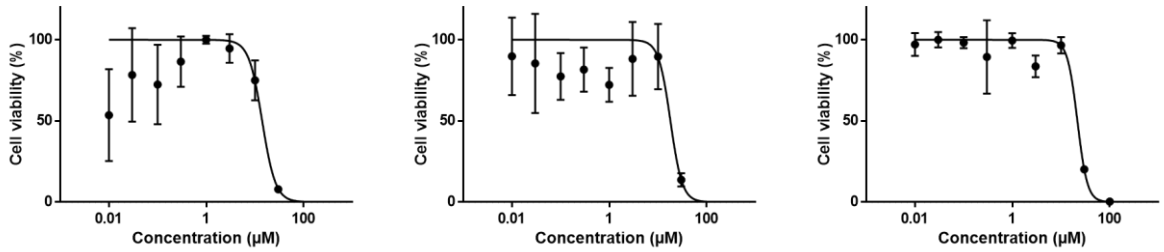

Figure S102: Fluorometric cell viability assay of 2bRe in CT26 cells after 48h incubation.

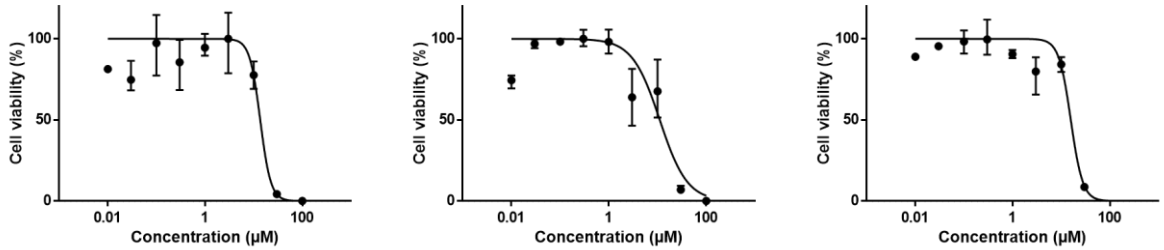

Figure S103: Fluorometric cell viability assay of 2cRe in CT26 cells after 48h incubation.

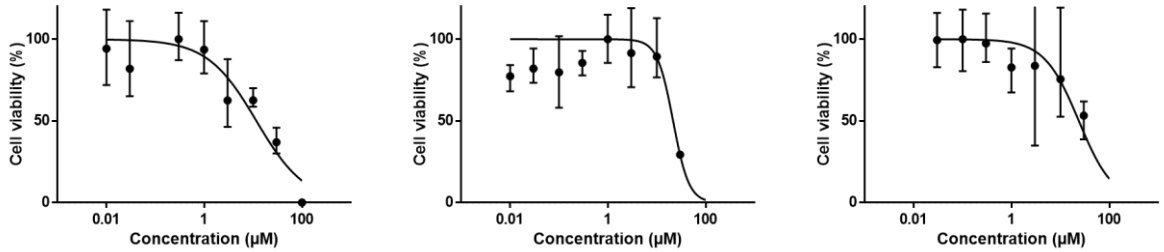

Figure S104: Fluorometric cell viability assay of 3Re in CT26 cells after 48h incubation.

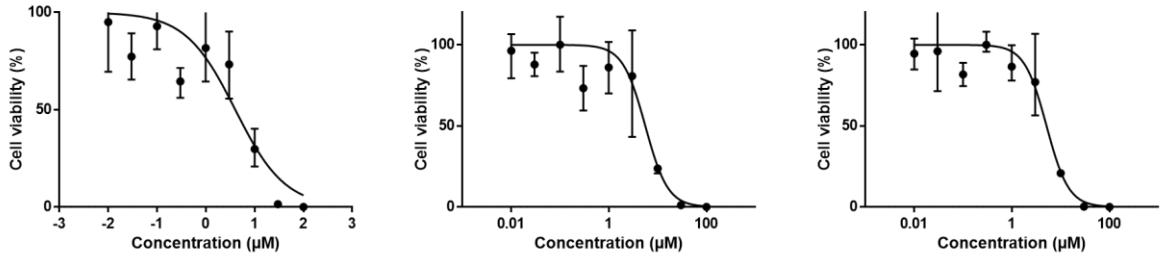

Figure S105: Fluorometric cell viability assay of 4aRe in CT26 cells after 48h incubation.

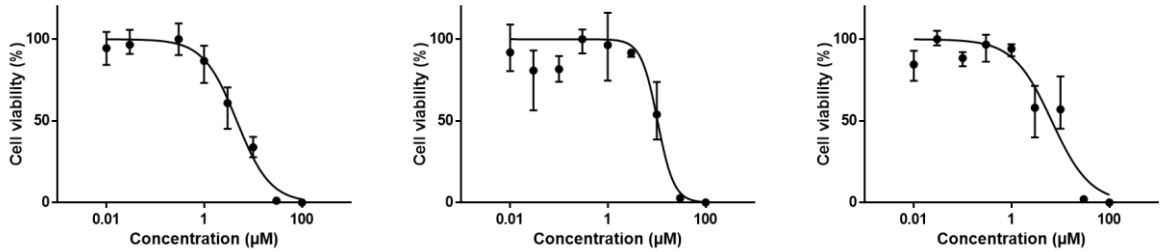

Figure S106: Fluorometric cell viability assay of 4bRe in CT26 cells after 48h incubation.

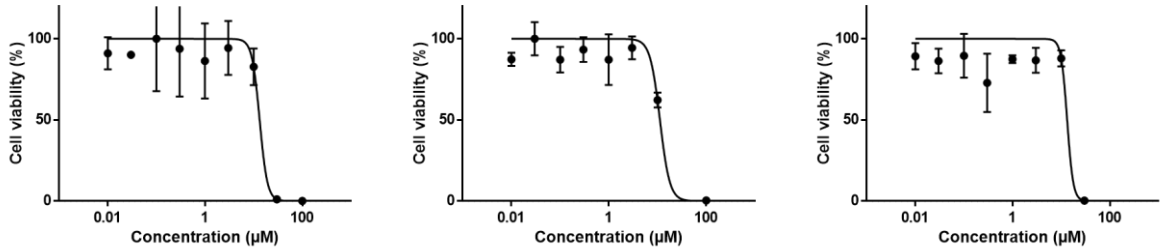

Figure S107: Fluorometric cell viability assay of 4aRe·OTf in CT26 cells after 48h incubation.

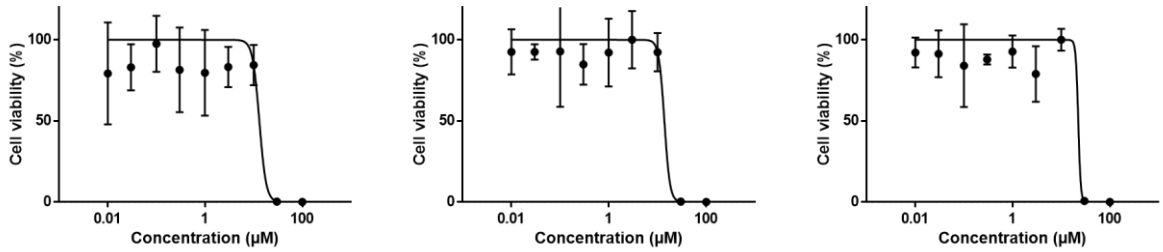

Figure S108: Fluorometric cell viability assay of 4bRe·OTf in CT26 cells after 48h incubation.

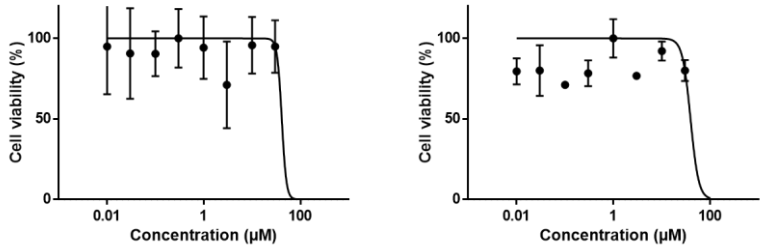

Figure S109: Fluorometric cell viability assay of 6aRe in CT26 cells after 48h incubation.

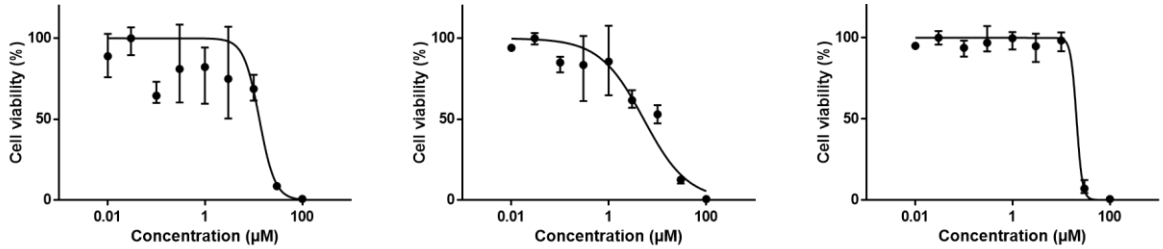

Figure S110: Fluorometric cell viability assay of 9Re in CT26 cells after 48h incubation.

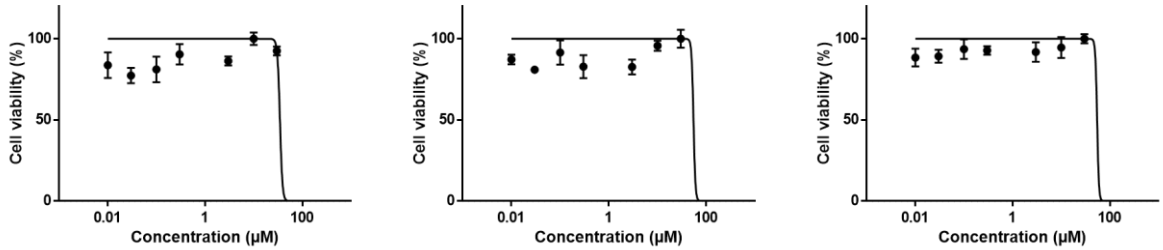

Figure S111: Fluorometric cell viability assay of 2aRe in HT29 cells after 48h incubation.

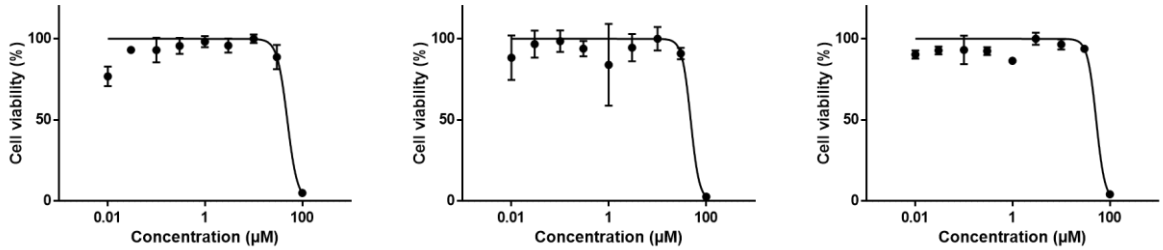

Figure S112: Fluorometric cell viability assay of 2bRe in HT29 cells after 48h incubation.

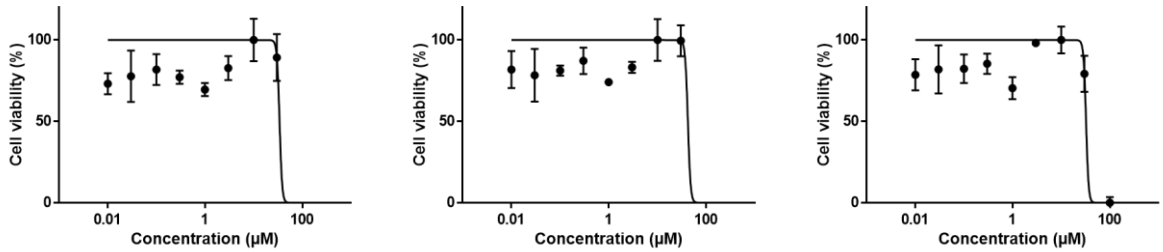

Figure S113: Fluorometric cell viability assay of 2cRe in HT29 cells after 48h incubation.

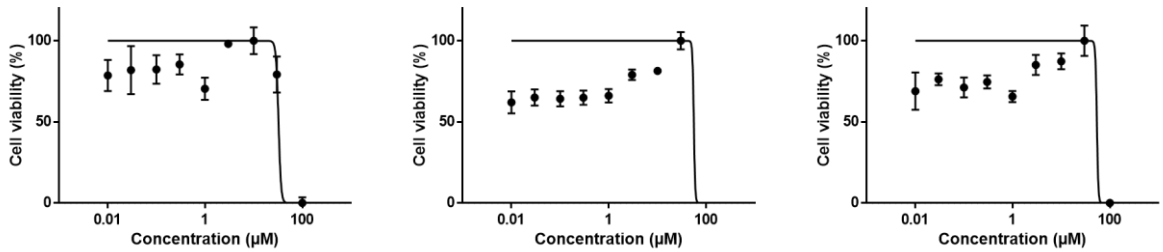

Figure S114: Fluorometric cell viability assay of 3Re in HT29 cells after 48h incubation.

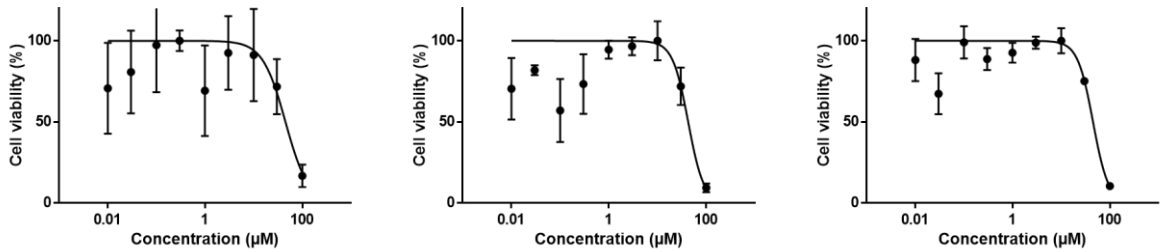

Figure S115: Fluorometric cell viability assay of 4aRe in HT29 cells after 48h incubation.

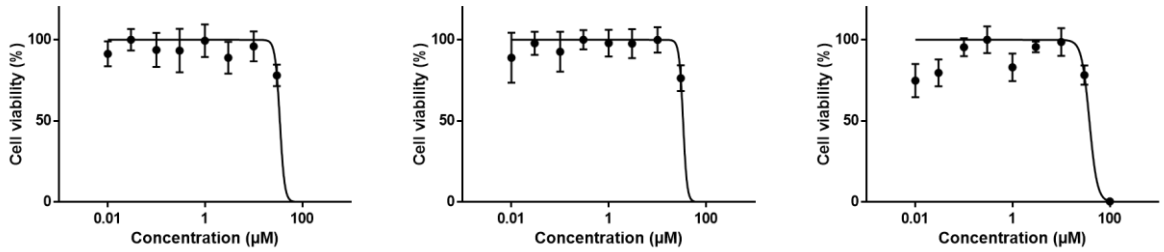

Figure S116: Fluorometric cell viability assay of 4bRe in HT29 cells after 48h incubation.

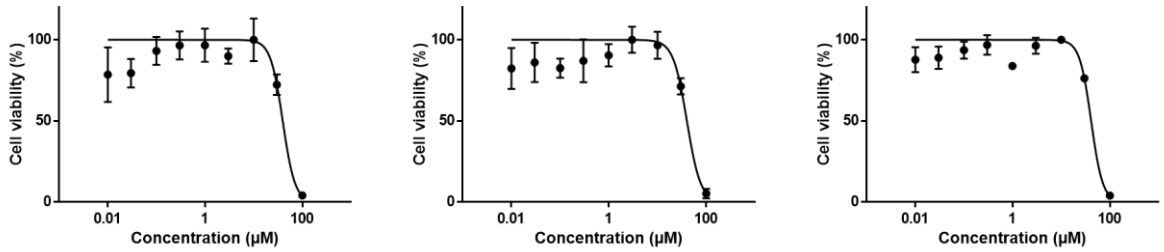

Figure S117: Fluorometric cell viability assay of 4aRe·OTf in HT29 cells after 48h incubation.

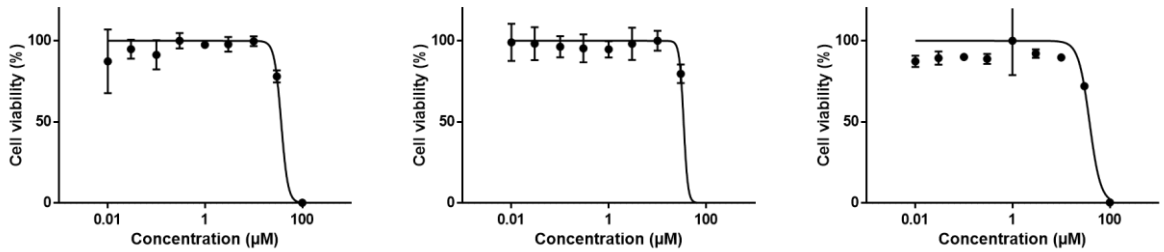

Figure S118: Fluorometric cell viability assay of 4bRe·OTf in HT29 cells after 48h incubation.

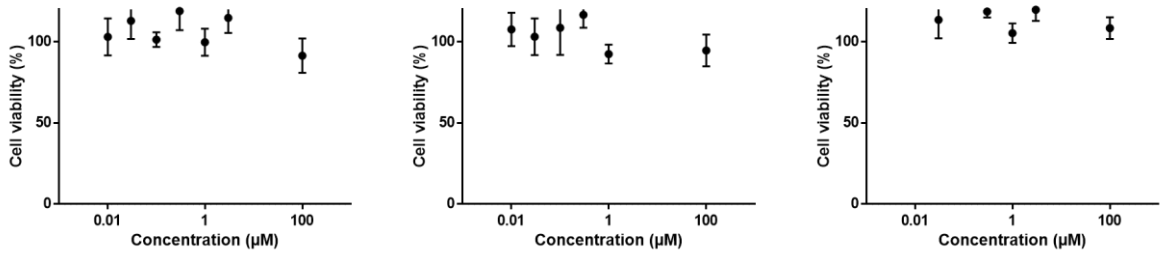

Figure S119: Fluorometric cell viability assay of 6aRe in HT29 cells after 48h incubation.

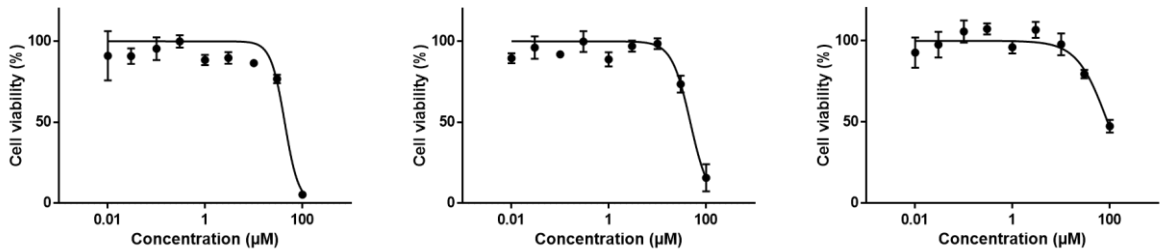

Figure S120: Fluorometric cell viability assay of 9Re in HT29 cells after 48h incubation.

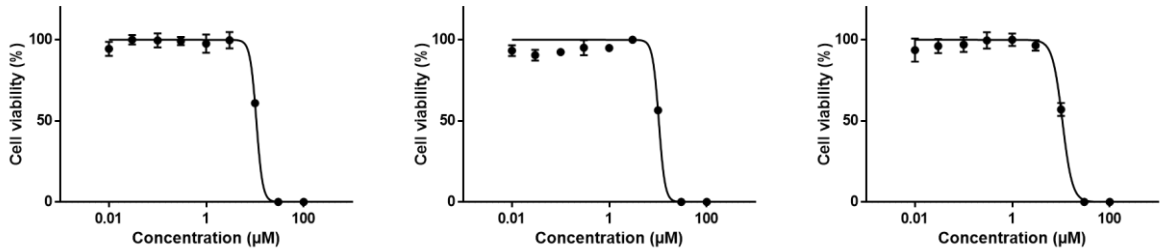

Figure S121: Fluorometric cell viability assay of 4aRe in RPE-1 cells after 48h incubation.

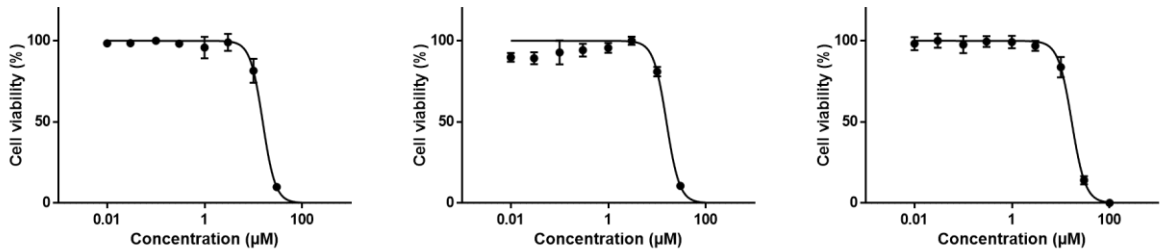

Figure S122: Fluorometric cell viability assay of 4bRe in RPE-1 cells after 48h incubation.

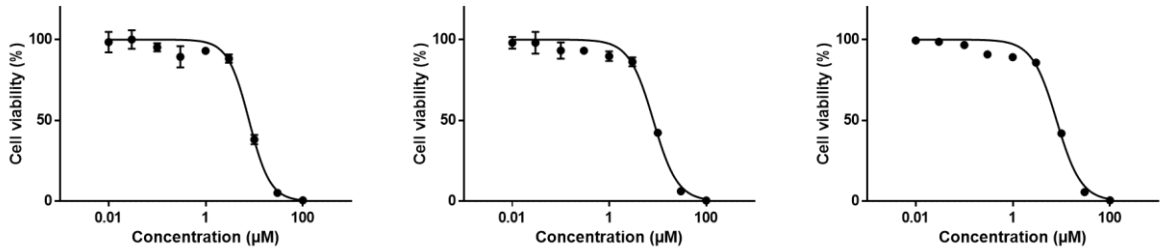

Figure S123: Fluorometric cell viability assay of 9Re in RPE-1 cells after 48h incubation.

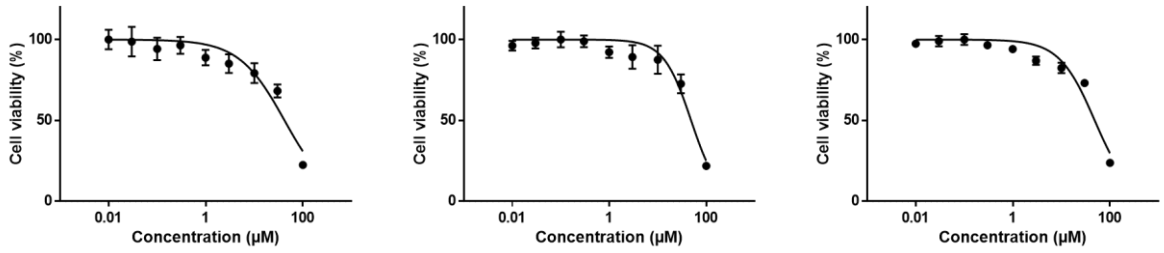

Figure S124: Fluorometric cell viability assay of CDDP–cisplatin in RPE-1 cells after 48h incubation.

10. Stability assessment

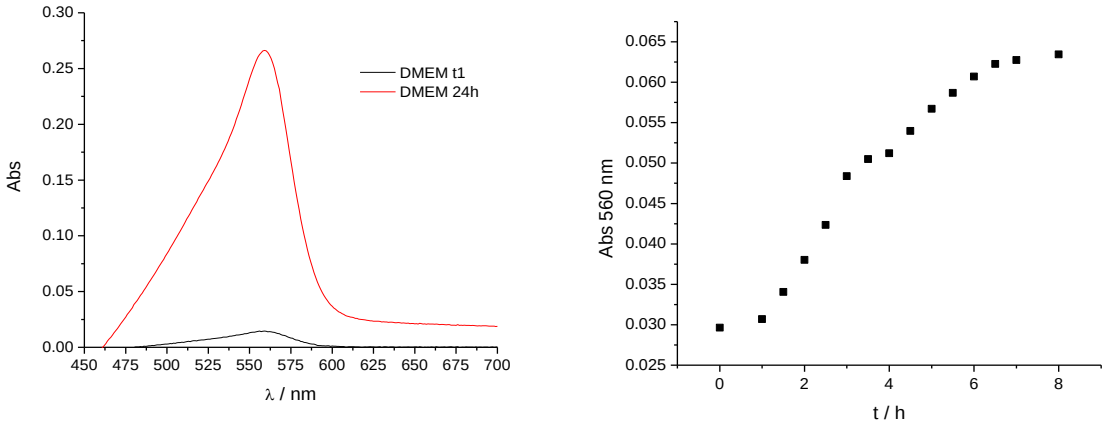

Figure S125. LEFT: UV/Vis spectra of DMEM with 10% fetal bovine serum and sodium cacodylate buffer (DMEM:buffer = 1:1) at time of preparation (t1) and after 24 h. RIGHT: Changes at DMEM maximum at 560 nm over 8 h.

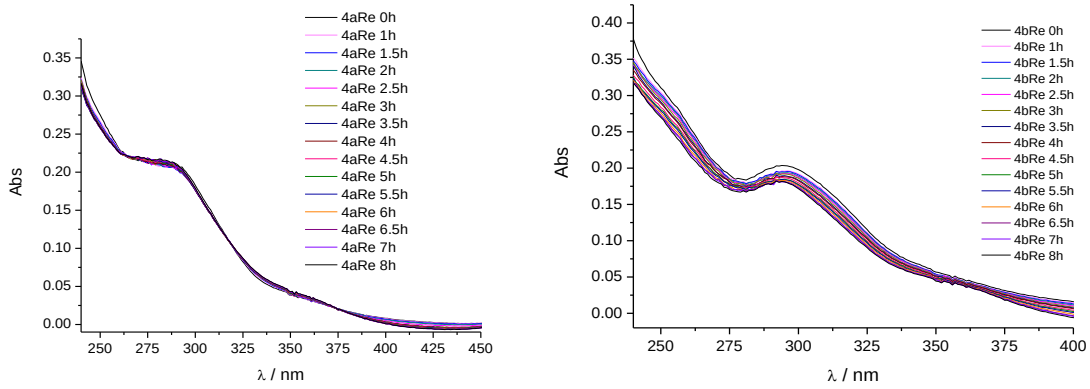

Figure S126. UV/Vis spectra of $4a_{Re}$ (LEFT) and $4b_{Re}$ (RIGHT), at $c = 1 \times 10^{-5}$ M, in DMEM with 10% fetal bovine serum and sodium cacodylate buffer (DMEM:buffer = 1:1) over 8 h.

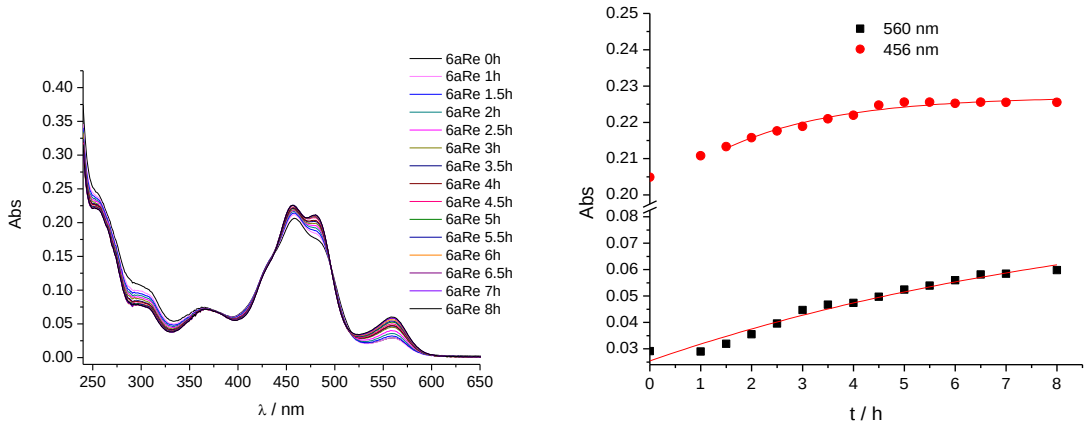

Figure S127. LEFT: UV/Vis spectra of $6a_{Re}$ (c = 1 × 10^{-5} M) in DMEM with 10% fetal bovine serum and sodium cacodylate buffer (DMEM:buffer = 1:1) over 8h. RIGHT: Note that DMEM absorbance change at 560 nm has the same trend as the change at maximum of $6a_{Re}$ (456 nm). When corrected for DMEM contribution, changes of UV/Vis spectrum of $6a_{Re}$ are negligible.

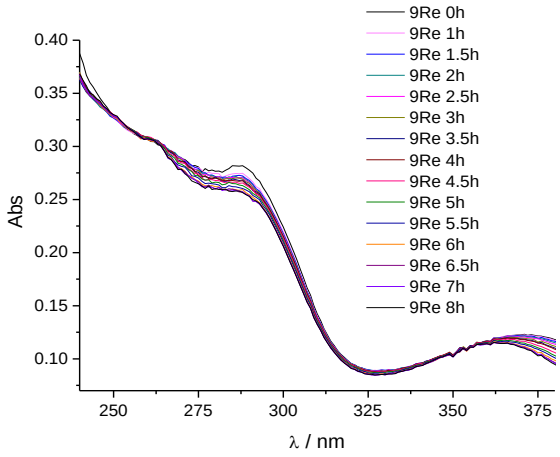

Figure S128. UV/Vis spectra of 9_{Re} (c = 1 × 10^{-5} M) in DMEM with 10% fetal bovine serum and sodium cacodylate buffer (DMEM:buffer = 1:1) over 8 h. When corrected for DMEM contribution, changes of UV/Vis spectrum of 9_{Re} are negligible.

11. Cellular localization

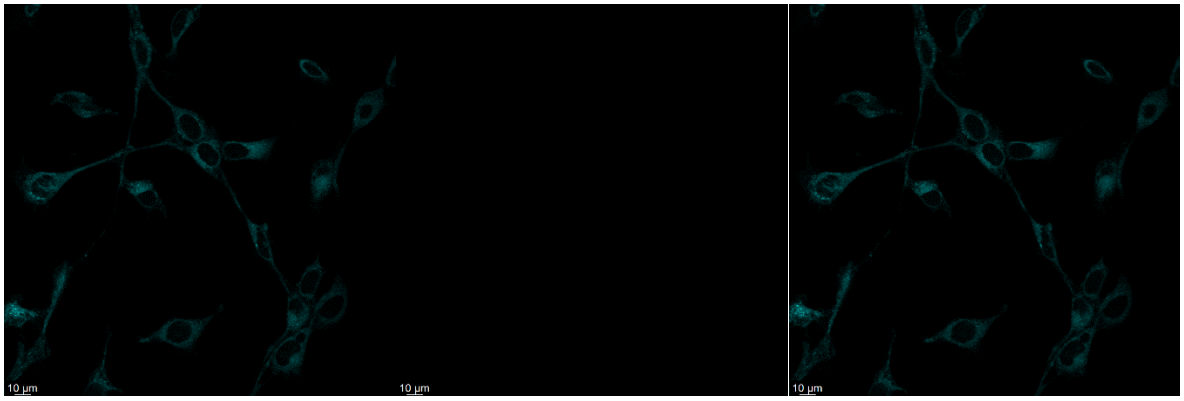

Figure S129. Confocal imaging in a CT26 cell line without fluorophore (negative control). Cells were labeled with LysoTracker™ Deep Red. Overlay is displayed on the right image. All scale bars: 10 µm, zoom: 0.75. On the left: Lysotracker fluorescence. In the middle: 9_{Re} fluorescence (negative control). On the right: overlay.

Figure S130. Confocal imaging in a CT26 cell line without fluorophore (negative control). Cells were labeled with LysoTracker™ Deep Red. Overlay is displayed on the right image. All scale bars: 10 µm, zoom: 1.53. On the left: Lysotracker fluorescence. In the middle: 9_{Re} fluorescence (negative control). On the right: overlay.

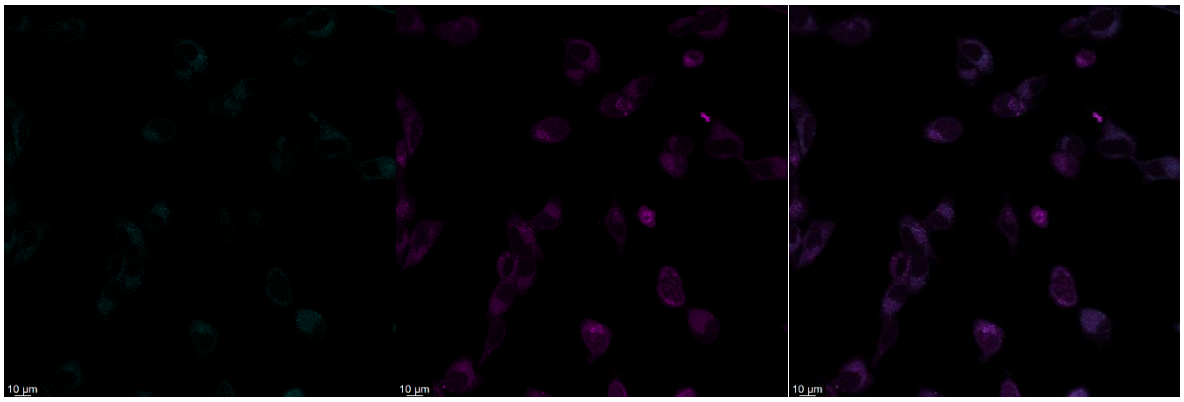

Figure S131. Confocal imaging in a CT26 cell line after 3 h of incubation with 7 µM of complex 9_{Re} (magenta). Cells were labeled with LysoTracker™ Deep Red (cyan). All scale bars: 10 µm, zoom: 0.75. On the left: Lysotracker fluorescence. In the middle: 9_{Re} fluorescence (7 µM). On the right: overlay.

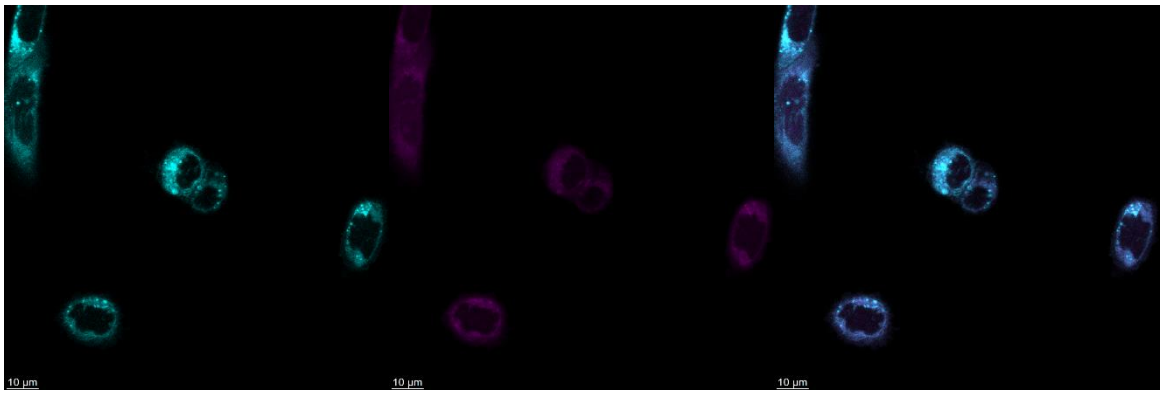

Figure S132. Confocal imaging in a CT26 cell line after 3 h of incubation with 7 µM of complex 9_{Re} (magenta). Cells were labeled with LysoTracker™ Deep Red (cyan). All scale bars: 10 µm, zoom: 1.53. On the left: LysoTracker™ Deep Red fluorescence. In the middle: 9_{Re} fluorescence (7 µM). On the right: overlay.

12. Literature

1 B. M. Upton, R. M. Gipson, S. Duhović, B. R. Lydon, N. M. Matsumoto, H. D. Maynard and P. L. Diaconescu, *Inorg. Chem. Front.*, 2014, **1**, 271.

2 Z. Yan, G. Wei, S. Guang, M. Xu, X. Ren, R. Wu, G. Zhao, F. Ke and H. Xu, *Dyes Pigm.*, 2018, **159**, 542–550.

3 X. Li, H. Zhang, Y. Xie, Y. Hu, H. Sun and Q. Zhu, *Org. Biomol. Chem.*, 2014, **12**, 2033.

4 N. Perin, R. Nhili, M. Cindrić, B. Bertoša, D. Vušak, I. Martin-Kleiner, W. Laine, G. Karminski-Zamola, M. Kralj, M.-H. David-Cordonnier and M. Hranjec, *Eur. J. Med. Chem.*, 2016, **122**, 530–545.

5 A. Meščić Macan, N. Perin, S. Jakopec, M. Mioč, M. R. Stojković, M. Kralj, M. Hranjec and S. Raić-Malić, *Eur. J. Med. Chem.*, 2020, **185**, 111845.